Doctoral Thesis

Interfacial Engineering for Enhanced Performance Optoelectronic Devices

Hak-Beom Kim

Department of Energy Engineering

(Energy Engineering)

Graduate School of UNIST

2019

Interfacial Engineering for Enhanced Performance Optoelectronic Devices

Hak-Beom Kim

Department of Energy Engineering
(Energy Engineering)

Graduate School of UNIST

Interfacial Engineering for Enhanced Performance Optoelectronic Devices

A thesis/dissertation
submitted to the Graduate School of UNIST
in partial fulfillment of the
requirements for the degree of
Doctor of Philosophy

Hak-Beom Kim

12/13/2018 of submission

Approved by

Advisor
Jin Young Kim

Interfacial Engineering for Enhanced Performance Optoelectronic Devices

Hak-Beom Kim

This certifies that the thesis of Hak-Beom Kim is approved.

12/13/2018 of submission

signature

Advisor: Jin Young Kim

signature

Sang Il Seok: Thesis Committee Member #1

signature

Myoung Hoon Song: Thesis Committee Member #2

signature

Tae-Hyuk Kwon: Thesis Committee Member #3

signature

Dong Suk Kim: Thesis Committee Member #4;

three signatures total in case of masters

Abstract

Interfacial engineering is worth considering as one of the most promising technologies in the field of solution-processed optoelectronic devices based on organics or perovskites. These optoelectronic devices process a variety of advanced merits such as mechanical flexibility and large area processability with low cost via solution-processing. Here, interfacial engineering is a key technology to maximize device performance, while maintains the processing merits mentioned above. Particularly, interfacial engineering controls energy levels and balances charge transport along interfacial layers by introducing surface modifiers or charge transport layers. This thesis demonstrates facile and efficient interfacial engineering techniques which tune electronic structures of the devices via spontaneously aligned interface dipole and selective charge carrier transport by introducing organic surface modifiers (OSMs) for photovoltaics and light-emitting diodes applications. Firstly, 4-chlorobenzoic acid (CBA), is incorporated into organic solar cells (OSCs) via a simple spin coating on a high work function indium tin oxide (ITO) electrode. By replacing PEDOT:PSS with CBA, higher power conversion efficiency (PCE) is achieved, which is attributed to higher visible transparency and improved interface compatibility between hole transport layer and organic active layer. Next, ethanolamine (ETA) is vapor-coated on ITO substrate in order to reduce the work function of ITO for the inverted structure of PSC which exhibit opposite electrode polarity compared to conventional structure. It is confirmed that ETA serves as an efficient electron transport layer where metal oxides have been often used. Maximized light absorption within the active layer as well as improved electron transport between the active layer and ITO cathode lead to the enhanced device performance. Thirdly, I also report an interfacial engineering of hole transport layer using various conjugated polyelectrolytes (CPEs) in PeSCs. By using CPE as hole transport layer, perovskite film exhibits better morphological uniformity and surface coverage, resulting in higher PCE. In addition, pH-neutrality improvs device stability in ambient air compared to those of the devices with acidic PEDOT:PSS as hole transport layer. Finally, perovskite based light-emitting solar cells (LESCs) is demonstrated. Halide perovskite is one of the promising materials for optoelectronic applications due to its long diffusion length, broad absorption range (~ 850 nm), high absorption coefficient (> 10^5 cm^{-1}) and high dielectric constant. Recently, perovskite optoelectronic devices have developed dramatically increased performance in both perovskite solar cells (PeSCs) and perovskite light-emitting diodes (PeLEDs). As both devices share similar device architecture and materials, perovskite can be used to realize single device that can efficiently operates in both PeSC and PeLED modes as LESCs. To do so, a polyelectrolyte based on a partially protonated PEI backbone with tetraimadazolylborate anions (PEI BIm_4) is incorporated as a selective electron transport layer in LESCs. Carefully designed interfacial materials and engineering

can support to implement high efficiency optoelectronic devices and give opportunities to study the device with totally new architecture.

Table of Contents

List of Figures

List of Table

Abbreviation

Abbreviation	Description
OSM	organic surface modifiers
CBA	4-chlorobenzoic acid
ITO	indium tin oxide
PCE	power conversion efficiency
PSC	polymer solar cell
PCE	power conversion efficiency
ETA	ethanolamine
CPEs	conjugated polyelectrolytes
PeSCs	perovskite solar cells
PeLEDs	perovskite light-emitting diodes
LESCs	light-emitting solar cells
PEI BIm_4	a polyelectrolyte based on a partially protonated PEI backbone with tetraimadazolylborate anions
CuPc	copper phthalocyanin
PCBM	[6,6]-phenyl-C61-butyric acid methyl ester
EQE	external quantum efficiency
J_{sc}	short-circuit current density
V_{oc}	open circuit voltage
IPCE	incident photon-to-current conversion efficiency
$CaTiO_3$	mineral calcium Titanium
DSSCs	dye sensitized solar cells
E_g	band gap
VBM	valence band maximum
CBM	conduction band maximum
UPS	ultraviolet photoelectron spectroscopy
HOMO	highest occupied molecular orbital

LUMO	lowest unoccupied molecular orbital
ICT	integer charge transfer
E_{ICT+}	energy of a positive integer charge transfer
E_{ICT-}	energy of a negative integer charge transfer
BHJ	bulk heterojunction
OSCs	organic solar cells
HTL	hole transport layer
ETL	electron transport layer
PEDOT:PSS	poly(3,4-ethylenedioxythiophene):poly-styrene sulfonate
SAMs	self-assembled monolayers
CB	chlorobenzene
DIO	1,8-diiodooctane
AFM	atomic force microscopy
XPS	X-ray photoelectron spectroscopy
RMS	root-mean-square
PTB7	poly[[4,8-bis[(2-ethylhexyl)oxy]benzo[1,2-b:4,5-b']dithiophene-2,6-diyl][3-fluoro-2-[(2-ethylhexyl)carbonyl]-thieno-[3,4-b]thiophenediyl]]
$PC_{71}BM$	[6,6]-phenyl-C_{71} butyric acid methyl ester
SCLC	space-charge-limited current
EIS	electrical impedance spectroscopy
PEIE	polyethylenimine ethoxylated
PFN	poly[(9,9-bis(3′-(N,N-dimethylamino)propyl)-2,7-fluorene)-alt-2,7-(9,9-dioctylfluorene)]
ETA-SC	ethanolamine deposited on ITO substrate via both spin-coating
ETA-SC	ethanolamine deposited on ITO substrate via both vapor-coating
FF	fill factor
V_2O_5	vanadium oxide
NiO	nickel oxide
ZnO	zinc oxide
CPE-K	poly[2,6-(4,4-bis-potassiumbutanylsulfonate-4H-cyclopenta-[2,1-b;3,4-b']-dithiophene)-alt-4,7-(2,1,3-benzothiadiazole)]

DMF	*N,N*-dimethylformamide
MAI	methylammonium iodide
MABr	methylammonium bromide
$PbCl_2$	lead chloride
PbI_2	lead iodide
$PbBr_2$	lead bromide
PL	photoluminescence
LEDs	light emitting diodes
IPA	anhydrous isopropanol
DMSO	dimethyl sulfoxide
TPBi	1,3,5-tris(N-phenylbenzimidazol-2-yl) benzene
WF	work function

CHAPTER 1. Introduction

1.1 History of organic solar cells

The discovery of solar cells began in 1839 by Becquerel,[1] who discovered photo currents. Adams and Smith reported the radiation rates in 1873 and in 1876, respectively. Then, Pochettino and Bolmer discovered anthracite as the first organic compound in 1906 and 1913.[2] Many researchers recognized the promising utilization of organic materials as a photo sensitizer for imaging systems in the 1950s and 1960s. With the growing scientific interest in being commercially viable, research on photoconductivity and related fields has soared. Many dyes were found to have semiconducting properties in the 1960s. After the oil crisis in the 1970s, the industry tried to develop eco-friendly energy resources and increased manufacturing and costs as a huge amount of effort went into research on photovoltaic cells, and manufacturing facilities have been built in many countries to produce photovoltaic modules using silicon-based p-type and n-type bonded solar cells. Later, low-cost photovoltaic cells were required for general use and the photovoltaic cells began to use organic materials. Tang et al. reported organic solar cells with 0.95% power conversion efficiency using two organic substances, copper phthalocyanin (CuPc) and perylene tetracarboxylic derivatives in 1986.[3]

One of the biggest developments in technology of organic solar cells was the discovery of C_{60} fullerene and its derivatives (e.g. [6,6]-phenyl-C61-butyric acid methyl ester, PCBM) to replace the n-type acceptor. C_{60} Derivatives have become standard n-type acceptor molecules of organic solar cells with strong electronics and high electron mobility. In the early 1990s, Heeger *et al.* and Yoshino *et al.* individually demonstrated the transfer of electronic charges between a conjugated polymer and a fullerene derivatives.[4, 5] They observed a very fast photo-induced electron transmission process of about 50–100 fs, which is dominant in all photophysical processes. These findings were very significant in establishing the foundation for organic solar cells technology, and researchers first demonstrated planar heterojunction organic solar cells in 1993s. The results contributed to the development of organic solar cells through a polymer-fullerene composite. Yu *et al.* have introduced bulk heterojunction structure to improve the power conversion efficiency of organic solar cells.[6] After, Kim *et al*. have come up with new directions in the field; developing tandem structured organic solar cells.7 Lately, power conversion efficiency of organic solar cells have achieved up to 18% by using various techniques of device architectures, new small-molecule acceptor and conjugated polymer donor materials.

1.2 Working principle of organic solar cells

The solar cells are a device that converts sunlight to produce electricity and typically operated in the following steps.[7]

1) Light absorption
2) Exciton diffusion
3) Exciton dissociation and Charge transport
4) Charge collection

When light is illuminated, the active layer absorbs photons in the device, then the generated excitons to diffuse at the donor-acceptor (D-A) interface to be dissociated into free charge. After electrons and holes transported to each electrode.

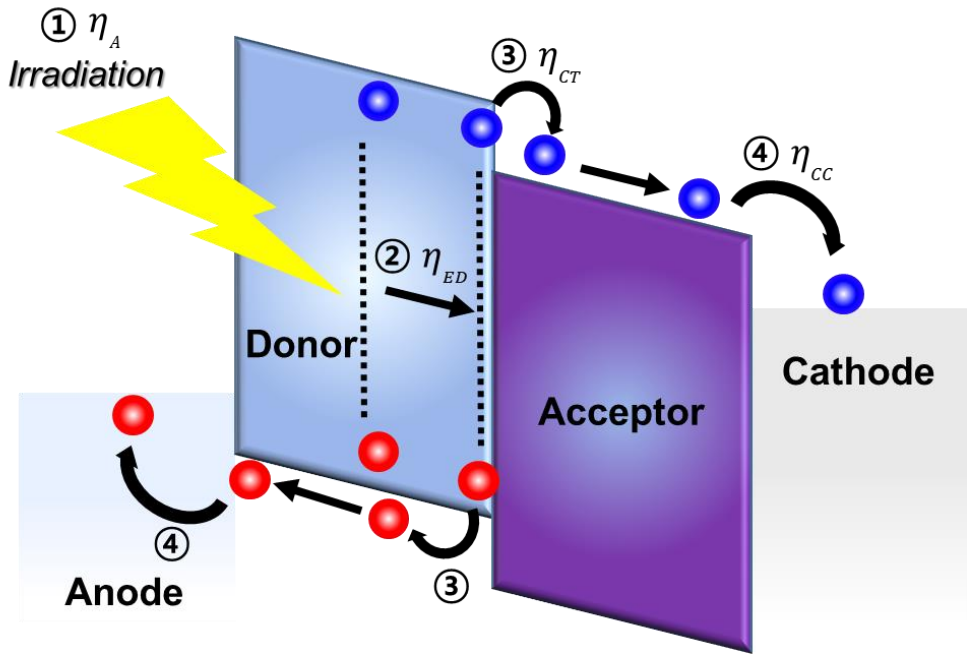

Figure 1. 1. Operation of organic solar cells.

The efficiency is the result of each steps. These 4-steps determine solar cells performance also closely linked to external quantum efficiency (EQE). EQE is defined as the number of photons collected by the device as a percentage of the number of charge carriers collected in the electrode under short circuit conditions.[8] EQE can be defined by the following equation. (1-1),

$$\mathrm{EQE} = \eta_A \times \eta_{ED} \times \eta_{CT} \times \eta_{CC} \quad (1\text{-}1)$$

① Light absorption (η_A)

The absorption of photons with the thickness of the photo-active layer is determined by the optical absorption coefficient, absorption spectral bands, and internal reflections. Most semiconducting polymers have band gaps larger than 2 eV and have a light absorption range of 650 nm, but recently there have been reported organic materials with a light absorption range of 900 nm. In general, the active layer thickness is 100nm to prevent loss of charge transfer, and to maintain a balance between sufficient light absorption and efficient transfer of charge, both the wide absorption spectral bands and the high absorption coefficient are important. Furthermore, the organic material has a very high absorption coefficient compared to silicon, making it possible to thin film devices to absorb enough light even in a thin layer. Excitons can be diffused to a D-A interface with $L_i \leq L_D$

② Exciton diffusion (η_{ED})

At the D-A interface, the Efficiency of exciton diffusion is closely related to the exciton diffusion length (L_D) and distance (L_i) between the D-A interface that serves as a photo-exciton dissociation center.[9] The L_D is equal to $(D_\tau)^{1/2}$, where D is diffusion coefficient and τ is exciton lifetime.[10] otherwise, they can be recombine with a reduced η_{ED}. In general, the exciton diffusion length is within the range of 4 to 20 nm for conjugated polymers.[11-13]

③ Exciton dissociation and charge transport (η_{CT})

The efficiency of exciton dissociation into free holes and electrons relies on D-A LUMO energy offsets and internal electric field at a D-A heterojunction. From current understanding, the minimum energy required to dissociate an exciton in a conjugated polymer is what is needed to overcome the exciton binding energy.[14] These energies can result from the offset between the LUMO energy levels of the donor and the acceptor.

The η_{CT} is charge transport efficiency. The holes are transported in a conjugated polymer, while the electrons are transported in an inorganic semiconductor. Both the donor and acceptor materials are required to form highly efficient percolation networks spanning the entire active layer to provide efficient charge transport.[15] The polymers need to have a higher degree of planarity for efficient

backbone stacking for a high hole mobility. Through the treatments such as thermal and solvent annealing, the polymers should also be able to self-assemble into a more organized structure.

④ Charge collection (η_{CC})

It is the fraction of the charge carriers transported from the active layer to the electrodes. The collected charge carriers depend on the energy level and electrodes of the active layer and the interface between each layer.

1.3 Characterization of organic solar cells

The efficiency of solar cells are determined by its open circuit voltage (*Voc*), short-circuit current density (*Jsc*) and fill factor and then, the efficiency can be calculated from the current density voltage (*J-V*) characteristic curves. The power conversion efficiency can be defined by the following equation. (1-2),

$$\eta = \frac{J_{sc} \times V_{oc} \times FF}{P_s} \times 100 \qquad (1\text{-}2)$$

Where P_S is the incident light power density. A standard test condition for solar cells is Air Mass 1.5 global (AM 1.5 G) with an incident power density of 100 mW cm^{-2} at a temperature of 25° C. Equivalent circuit of a solar cell is shown as **Figure 1.2**. A series resistance (R_S) originates from contact and bulk semiconductor, and a shunt resistance (R_{sh}) comes from poor diode contact. The *J-V* characteristics can be described as equation. (1.3),[16]

$$J = J_s \left\{ \exp\left[\frac{q(V - JR_sA)}{nKT}\right] - 1 \right\} + \frac{V - JR_sA}{R_{sh}A} - J_{ph} \qquad (1\text{-}3)$$

Where k is Boltzmann's constant, T is temperature, q is elementary charge, A is device area, n is ideality factor of the diode, J_s is reverse saturation current density, J_{ph} is photocurrent, R_S is series resistance and R_{sh} is shunt resistance. The *J-V* curves and photovoltaic parameters including V_{OC} and FF strongly depend on the n, J_s, R_S, and R_{sh}.

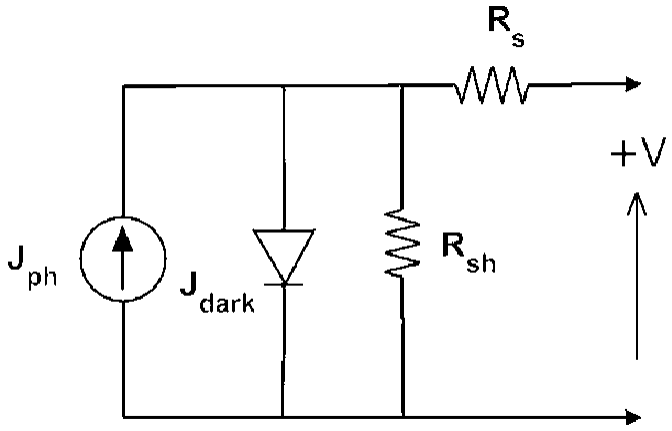

Figure 1. 2. The equivalent circuit of solar cells.

An ideal solar cell has *n* close to 1, 0 of R_s, and infinite R_{sh}. These conditions reduce equation. (1-3),

$$J = J_s\left[\exp\left(\frac{qV}{kT}\right) - 1\right] - J_{ph} \tag{1-4}$$

which is a typical diode equation with an additional term, $-J_{ph}$. Ideal J_s exhibits exponential dependence on E_g: $J_s \sim \exp(-E_g)$. Short-circuit current density, J_{SC} ($V = 0$) is equal to J_{ph} in the ideal case and open circuit voltage, V_{OC} is obtained by putting $J = 0$ to equation (1-4).

$$V_{OC} = \frac{kT}{q}\ln\left(\frac{J_{ph}}{J_s} + 1\right) \tag{1-5}$$

Output power density of the device can be calculated by multiplying V to equation (1-4).

$$P_{out} = JV = J_sV\left[\exp\left(\frac{qV}{kT}\right) - 1\right] - J_{ph}V \tag{1-6}$$

Maximum output power density, P_m is achieved when $dP_{out}/dV = 0$:

$$\frac{dP_{out}}{dV} = \frac{d(JV)}{dV} = \frac{dJ}{dV}V + J = 0 \tag{1-7}$$

Substituting equation (1-4) for J of dJ/dV in equation (1-7) gives the current density at maximum power point (mpp), J_m:

$$J_m = -J_s\beta V_m \exp(\beta V_m) \tag{1-8}$$

where β is kT/q. The voltage at mpp, V_m can be obtained by substituting equation (1-8) for J in equation (1-4):

$$-J_S\beta V_m \exp(\beta V_m) = J_s\left[\exp\left(\frac{qV_m}{kT}\right) - 1\right] - J_{ph}$$

$$V_m = \frac{1}{\beta}\ln\left[\frac{(J_{ph}/J_s)+1}{1+\beta V_m}\right] = V_{OC} - \frac{1}{\beta}\ln(1 + \beta V_m) \tag{1-9}$$

The power conversion efficiency (PCE) is the ratio of P_m to the incident power density, P_{in}.

$$\eta = \frac{|P_m|}{P_{in}} = \frac{|I_mV_m|}{P_{in}} = \frac{J_s\beta V_m^2\exp(\beta V_m)}{P_{in}} \tag{1-10}$$

(-) sign of P_m from J_m was removed in equation (1-10) because the sign indicates the power is generated from the device. Positive sign of P_{in} in denominator means that the power is absorbed by the device. For the efficiency calculation, the sign of each power is physically meaningless.

J-V characteristics of solar cell under illumination is shown in **Figure 1.3**.

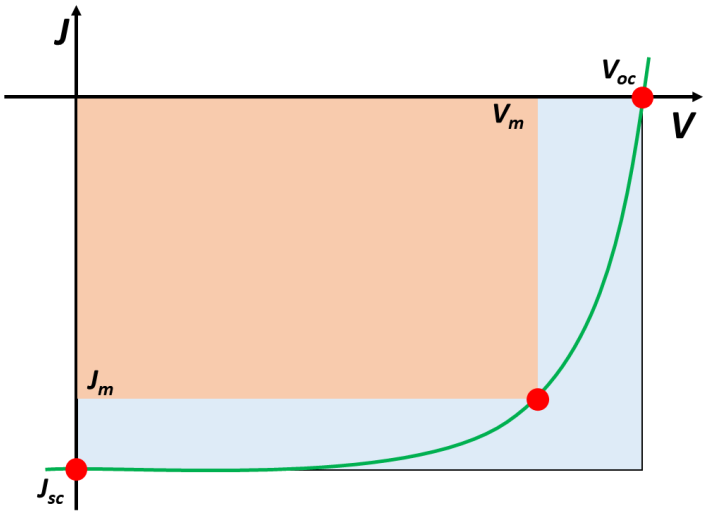

Figure 1. 3. *J-V* characteristics of solar cells under illumination.

Here, a new figure of merit, fill factor, *FF* is introduced. *FF* is a geometrical parameter measuring the degree of areal occupation of blue square ($V_m \times I_m$) in green square ($V_{OC} \times J_{SC}$). It cannot reach to 100% even in ideal solar cell because of the exponential dependence of *J-V* characteristics. PCE, then can be expressed using V_{OC}, J_{SC}, and *FF*:

$$\eta = \frac{|P_m|}{P_{in}} = \frac{|V_m I_m|}{P_{in}} = \frac{V_{OC} J_{SC} FF}{P_{in}} \tag{1-11}$$

equation (1-10) addresses the consideration on theoretical maximum efficiency of solar cell. V_{OC} decreases with smaller E_g because of increased J_s, but J_{SC} increases. Because of this trade-off, it is reported that theoretical maximum efficiency of 30.6% can be achieved at 1.32 eV of E_g. The values can exhibit some discrepancy depending on the studies. The theoretical efficiency limit is called Schokley-Queisser limit.

In nonideal solar cell, *FF* is hugely affected by two parasitic resistances, R_s and R_{sh}:

$$FF(R_s, R_{sh}) = FF(0, \infty)\left[\left(1 - \frac{J_{SC} R_s}{V_{OC}}\right) - \left(\frac{V_{OC}}{J_{SC} R_{sh}}\right)\right] \tag{1-12}$$

Another useful method for measuring solar cells is the incident photon-to-current conversion

efficiency (IPCE), which is also called EQE, for monochromatic radiation. The IPCE value is the ratio of the observed photocurrent divided by the incident photon flux, uncorrected for reflective losses during optical excitation through the conducting glass electrode. The IPCE value determinates the percentage of incident photons converted to electrons that are predominantly coincident with the absorption spectrum of the solar cells. The IPCE can be defined by the following equation (1-13).

$$\mathrm{IPCE} = \frac{\text{number of electrons through the external circuit}}{\text{number of photons incident}} = \frac{[1240\ (\mathrm{eV\ nm})][\text{photocurrent density}(\mu\mathrm{A\ cm^{-2}})]}{[\text{wavelength (nm)}][\text{irradiation}(\mathrm{mW\ cm^{-2}})]} \tag{1-13}$$

The intensity of the sun's spectra changes further as they pathways through the Earth's atmosphere. A measure has been prepared to show how the solar radiation affects the mass and strength of the solar radiation. The sun on the Earth's surface at an incident angle 48.2° (AM 1.5 spectrum), as shown in **Figure 1.4.**[17]

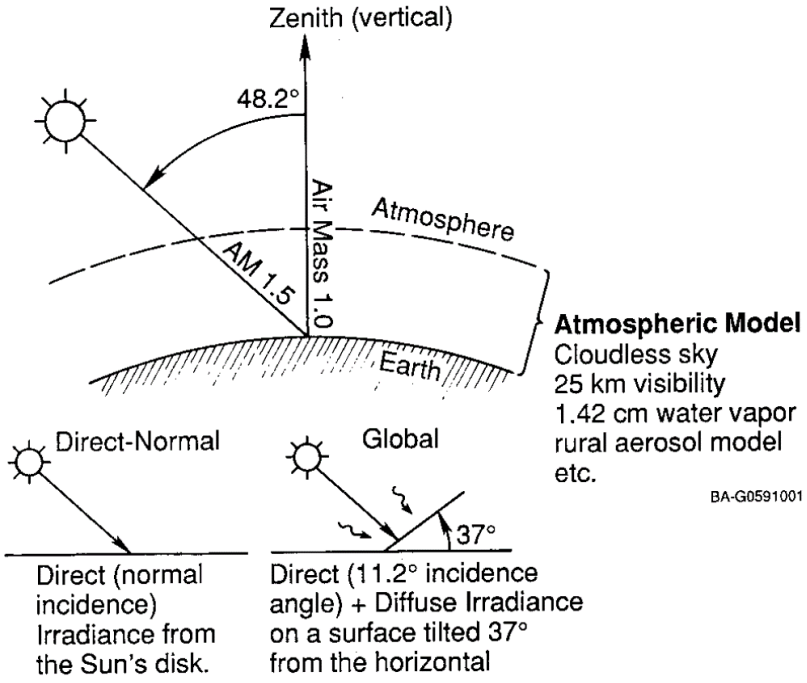

Figure 1. 4. Schematic explanation of the AM 1.5 spectrum.

1.4 Crystal Structure of perovskite material

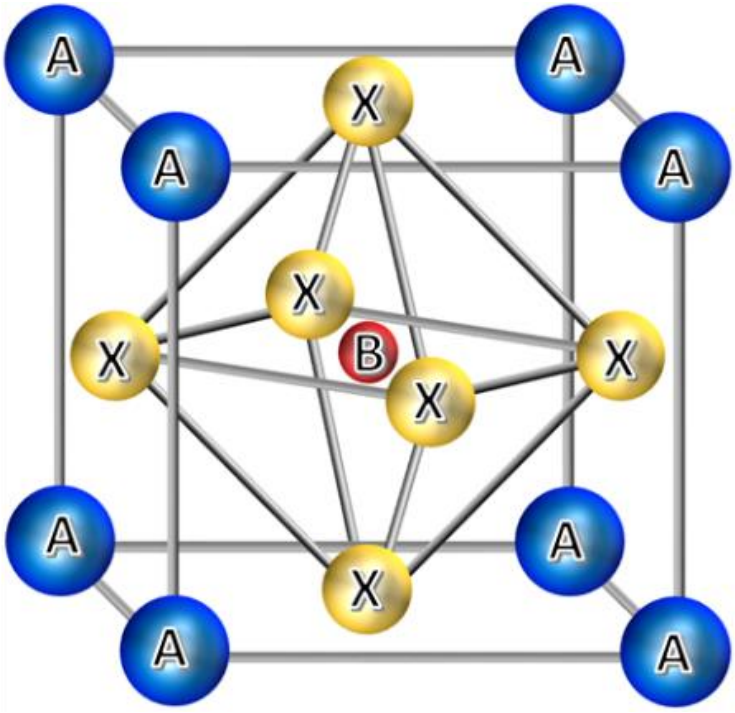

Figure 1. 5. Schematic of ABX_3 perovskite structure.

The general formula crystal structure in metal halide based perovskite is ABX_3 (**Figure 1.5**), where A-site shows organic and inorganic cations, B-site shows a divalent metal cation, X-site shows halide anions such as Cl^-, Br^- and I^-. Recently, most reported metal halide based perovskite solar cell consist of methylammonium lead triiodide ($MAPbI_3$) or formamidinium lead triiodide ($FAPbI_3$).

A- site = an organic cations ($CH_3NH_3^+$, $HC(NH)_2^+$) or inorganic cations (Cs^+, Rb^+)
B- site = divalent metal cation (Cu^{2+}, Fe^{2+}, Cd^{2+}, Mn^{2+}, Ge^{2+}, Sn^{2+}, Pb^{2+})
X- site = halide anions (Cl^-, Br^-, I^-)

Since the discovery of Perovskite structures in 1839s, this material has been extensively investigated and Goldschmidt's tolerance factor (t) explained by Victor M. Goldschmidt in 1962s.23 This tolerance factor is used to indicate the stability of the perovskite structure and is calculated using the ion radius of the atoms. The tolerance factor can be defined by the following equation. (1-14)

$$t = \frac{(r_A + r_x)}{\sqrt{2}(r_B + r_x)} \qquad (1\text{-}14)$$

The tolerance factor, r_A is the ionic radius of the A cations, r_B is the ionic radius of the B cations and r_x is the ionic radius of the X anion. The tolerance factor estimates if the A cation can fit inside the vacancies of the BX3 framework. Where a tolerance factor of $t = 1$, represents a fit resulting in the formation of a perfect cubic structure perovskite. In general, If the range of $0.89 \geq t \leq 1.00$, it can be expected a cubic structure perovskite. In case, for metal halide perovskites are generally formed with the rage of $0.81 \geq t \leq 1.11$, and then if the range of $t > 1.1$ or $t < 0.8$, the perovskite structure cannot be formed.

1.5 History of perovskite solar cells

The name Perovskite originally started in 1839 with mineral calcium Titanium ($CaTiO_3$) and now collectively defined Perovskite with the materials of same structure as $CaTiO_3$ (ABX_3, **Figure 1.5**) The perovskite material can change the composition of matter to create a variety of properties. For example, it is very interesting material that shows conductivity, piezoelectricity, electric resistance change, and phase separation of material structure, as well as conductor, semi-conductor, and superconductivity. Therefore, the material is being studied in various fields.

In the field of solar cells, in 2009s, Kojima *et al*. reported 3.8 % power conversion efficiency that metal halide based perovskites were able to function as sensitizer in a dye sensitized solar cells (DSSCs).[18] In these metal halide based perovskites, A-site is organic or inorganic, B-site is metal, and X-site is halide anions. Since initial discovery, the research into meatal halide based perovskite for optoelectronic applications has dramatically increased. In particular, the study soared after two different study groups reported more than 10 % efficiency for solid-state solar cells in 2012s.[19, 20] This is evidenced by the number of publications about Perovskite solar cells next year. (**Figure 1.6**)

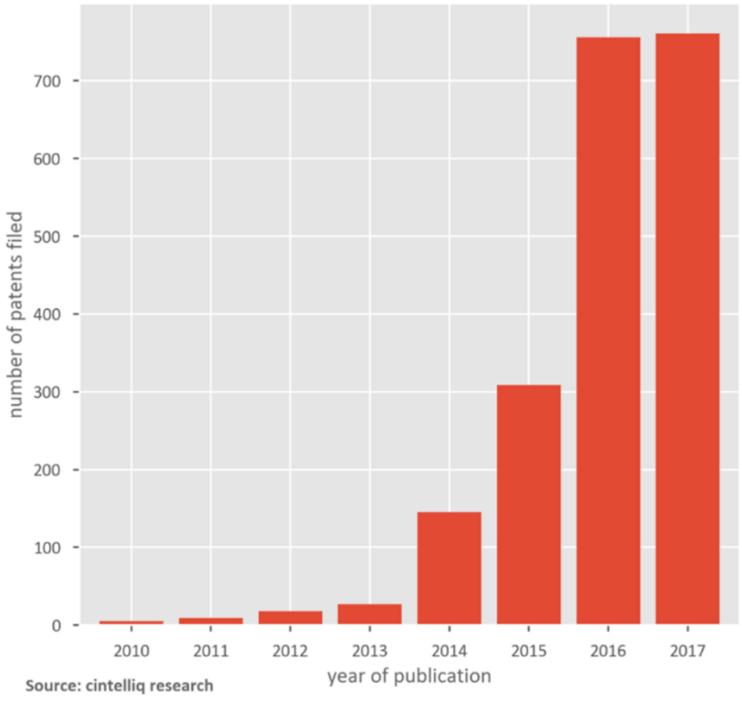

Figure 1. 6. Annual number of published perovskite solar cells.

This increased effort in research has improved understanding and efficiency of these perovskite solar cells devices. The perovskite solar cells have risen very rapidly since its first discovery in 2009, becoming an efficient solar cell that approaches silicon, in just a few years. Currently, according to the

solar cells efficiency chart provided by NREL, Perovskite solar cells show up to efficiency of 22.7 %. (**Figure 1.7**) Another advantage of perovskite solar cells, they can be based on organic solar cells, applying thin film solution processing technology. The fact that silicon solar cells can combine high efficiency with the processing power of thin-film organic solar cells to make future high efficiency solar panels a low-cost production makes this particularly attractive.

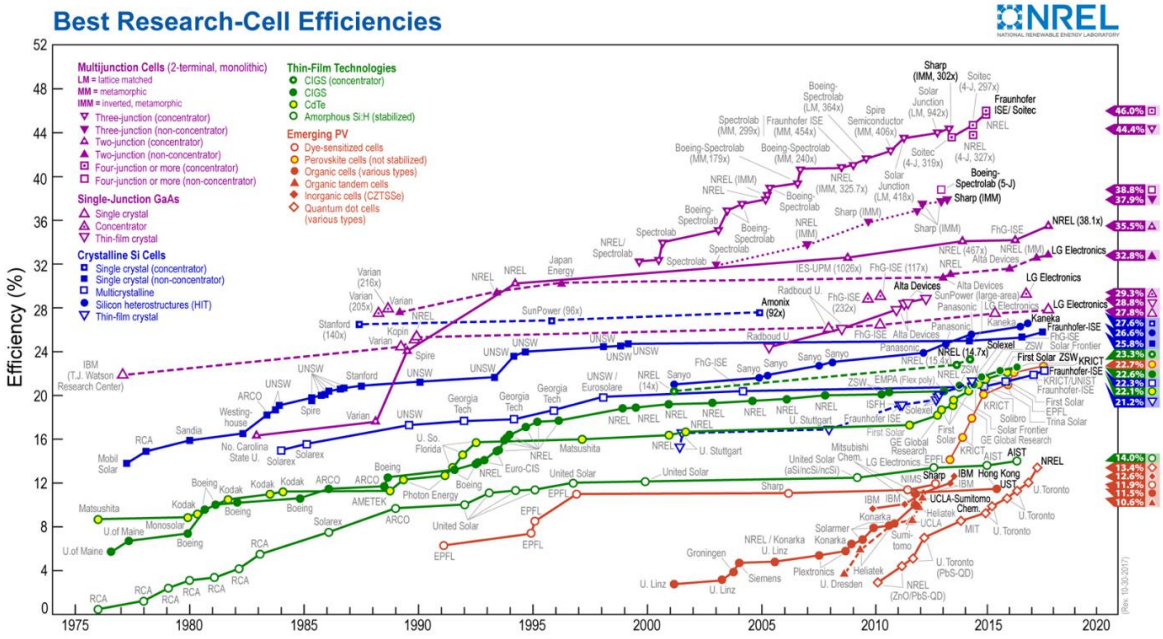

Figure 1. 7. Best research solar cell efficiencies.

1.6 Optical Band gap tuning of perovskite

The perovskite, commonly used $MAPbI_3$ in solar cells, has estimated band gap (E_g) range of 1.5 ~ 1.6 eV. In this case, the maximum absorption wavelength is 800 nm, but the perovskite can control to have longer or shorter absorption wavelength via band gap tuning without the adjusting absorption coefficient. Accessing the A-site MA ion as a substitute for FA ion enables band gap tuning without affecting the valence band maximum (VBM). By using FA ion, the absorption wavelength is extended up to 840nm, which is a reduction in band gap of approximately 0.07eV. Another approach to control the bad gap is adjustment in B-site. Modification of metal cations have a significant effect on both the conduction band maximum (CBM) and VBM. Replacing Pb^{2+} with Sn^{2+} ions, changes the values of CBM and VBM, and then orderly tuning of the bad gap in mixed Pb^{2+} and Sn^{2+} ions perovskites from 1.58 eV to 1.24 eV.[21]

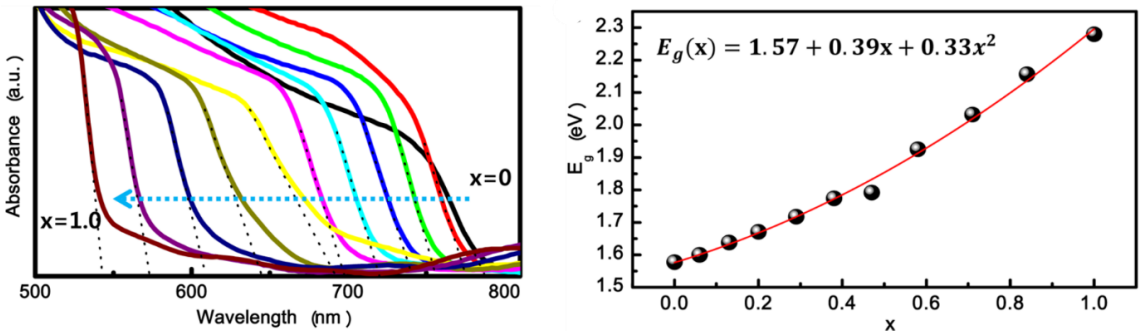

Figure 1. 8. UV-vis absorption spectra and a quadratic relationship of the band gap of $MAPb(I_{1-x}Br_x)_3$ as a function of Br composition (x).

Finally, band gap tuning of perovskite has been achieved via X- site halide substitution. Especially, replacement of I^- and Br^- ions, which results from a strong reliance of electronic energies on the effective exciton mass. A systematic shift of the shorter absorption wavelength with increasing Br^- ion ratio in X-site. This result indicates that the band gap can be tuned by the composition of the mixture. Park *et al*. reported a quadratic relationship of the band gap of $MAPb(I_{1-x}Br_x)_3$ perovskite as a function of Br composition (x) (**Figure 1.8**)[22] that can be expressed by following equation. (1-15)

$$E_g[MAPb(I_{1-x}Br_x)_3] = E_g[I] + \left(E_g[Br] - E_g[I] - b\right)_x + bx^2 \qquad (1\text{-}15)$$

Where I is $MAPbI_3$, Br is $MAPbBr_3$, and b is the bowing parameter. The method of least squares fit (redline) of band gap in **Figure 1.8** changes the equation (1-15) to equation (1-16) which yields the bowing parameter of b = 0.33 eV.

$$E_g(x) = 1.57 + 0.39x + 0.33x^2 \quad (1\text{-}16)$$

The stretch of bowing is a measure of the range of variation in the crystal field or the nonlinear effect arising from anisotropic nature of binding.[23] The result from equation that the small bowing parameter 0.33 eV in $MAPb(I_{1-x}Br_x)_3$ compared with other perovskite mixture suggests that $MAPbI_3$ and $MAPbBr_3$ have a quite well miscibility.[24]

Consequently, $MAPb(I_{1-x}Br_x)_3$ comprises the entire composition of the compound and these perovskites provide convenient band gap tuning by a simple mixture process. **Figure 1.9** shows a schematic energy level diagram of the possible combinations of perovskite materials.[25]

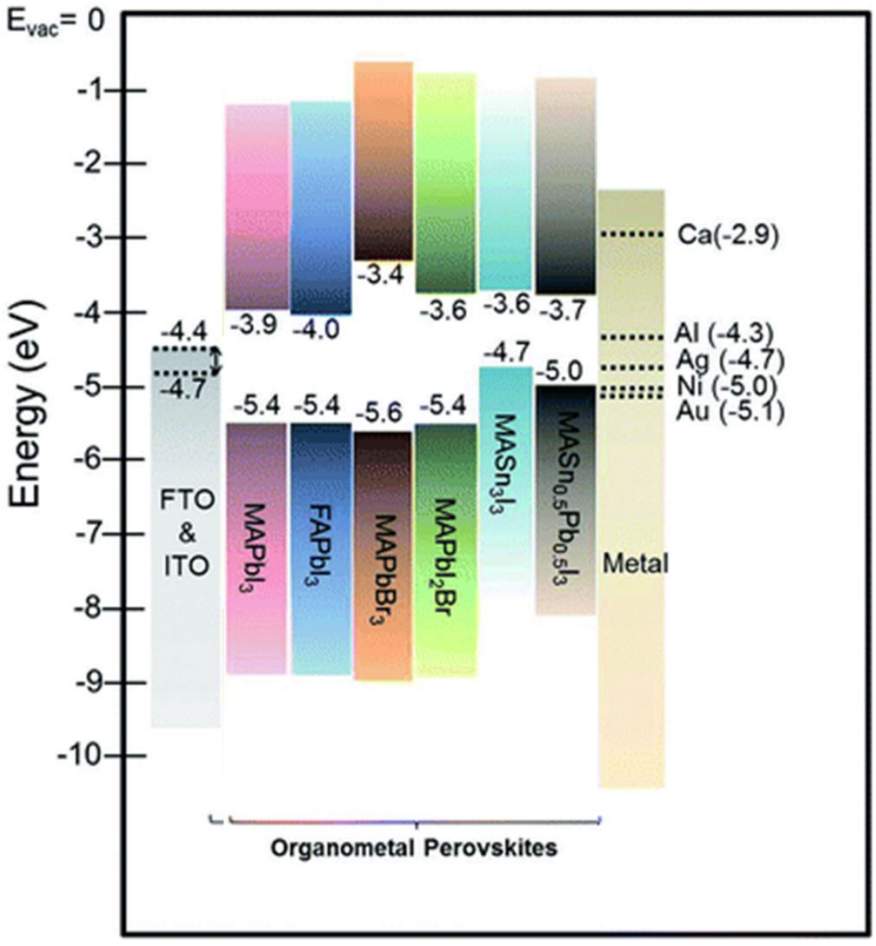

Figure 1. 9. Schematic energy level diagram of the possible combination perovskite.

CHAPTER 2. Interfacial Engineering

2.1 Metal-organic interface

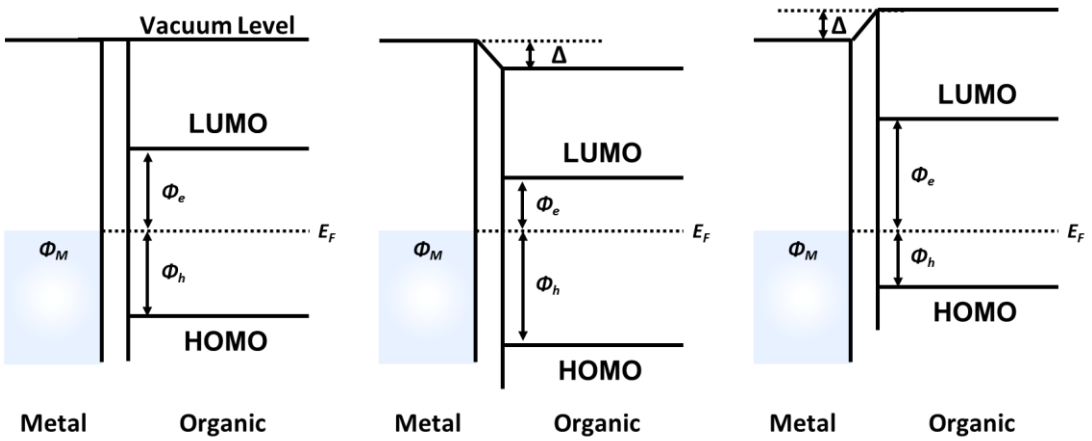

Figure 2. 1. Schematic vacuum level alignment at the metal-organic interface.

The work function of metal (Φ_M) in the intimate contact with organic materials. If the energy level of HOMO deeper than Φ_M, the Holes will transport across the interface to the organic HOMO level due to minimizing the energy until the Fermi level (E_F) is aligned, effectively pinning the HOMO level of the organic material to (Φ_M). Likewise, if higher energy level of LUMO than Φ_M, the electrons will transport to the LUMO level of organic material. In short, this phenomenon is defined Pinning of Fermi level and is effectively shown as a dipole shift of the vacuum level. If energy barrier for electrons or holes (Φ_h or Φ_e) have similar values between the HOMO and LUMO levels of organic materials. In case, the ΦM is not pinning. However, several researchers have demonstrated that the Fermi level does not pin to the between bulk HOMO and LUMO levels, because the interfaces of organic materials can have different properties, only to band of interfacial states respectively. The Fermi level pinning has been demonstrated by interfacial dipole via ultraviolet photoelectron spectroscopy (UPS) measurements. In the meantime, the researchers reported on the mechanism of interfacial dipole formation, but the exact underlying mechanisms are a subject still under debate. Recently, Fahlman *et al*. demonstrated the mechanism of interfacial dipole formation that one of the promising model is the integer charge transfer (ICT) model.[26]

2.2 The integer charge transfer model

The integer charge transfer (ICT) model assumes that an integer amount of charge is transferred, as opposed to partial charge transfer. The ICT model is generally used to describe interaction organic and substrate interface that are passivated by hydrocarbons or oxides. The presence of hydrocarbons or oxides disrupts the formation of interfacial dipoles via partial electron transfer, thereby, the work function of substrates effectively shifted via the push-back effect. It is also preventing hybridization of electronic state by decouples the π-electron from substrate bands. The ICT model via a tunneling mechanism that means the transfer of an integer amount of charges. The energy of a positive integer charge transfer (E_{ICT+}) is defined as energy required to remove a single electron from a molecule producing a fully relaxed state and the energy of a negative integer charge transfer (E_{ICT-}) is defined as the energy gained when a single electron is added to the molecule producing a fully relaxed state. The different way for energy level alignment in between metal and organic interface contact. The ICT model can be described by the following three type formulas. (**Figure 2.2**)

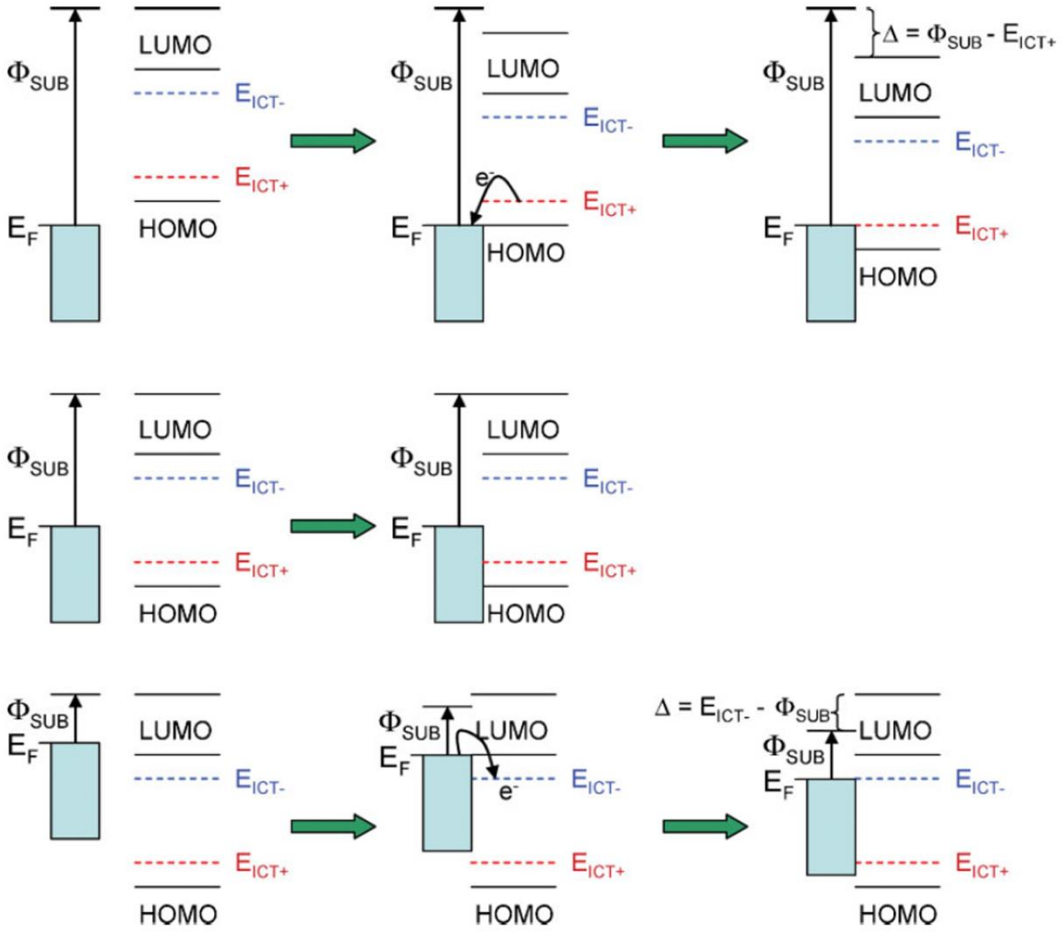

Figure 2. 2. Schematic of the evolution of the energy-level alignment at metal-organic interface in ICT model.

Firstly, if Φ_{SUB} higher than E_{ICT+} electrons will transport from the organic material into the substrate lead to vacuum level shift (Δ), this transport will continue until $E_{ICT+} + \Delta = \Phi_{SUB}$, hence the Fermi level will be pinned to the E_{ICT+} level by follow formula. (2-1)

$$\Phi_{SUB} > E_{ICT+} \tag{2-1}$$

Fermi level pinning to a positive ICT state, substrate-independent resulting work function $\Phi_{ORG/SUB}$

Secondly, if Φ_{SUB} located exactly between E_{ICT+} and E_{ICT-} electrons cannot transport across the interface. Hence, since no spontaneous charge transfer across the organic and substrate interface occurs in reaching equilibrium, there is no vacuum level offset, that means vacuum level alignment keeps for this type of interface by follow formula. (2-2)

$$E_{ICT-} < \Phi_{SUB} < E_{ICT+} \tag{2-2}$$

Vacuum level alignment, substrate-dependent resulting work function $\Phi_{ORG/SUB}$, slope = 1

Finally, if Φ_{SUB} deeper than E_{ICT-} the opposite will occur, that is electrons will transport from the substrate into the organic material until $E_{ICT-} - \Delta = \Phi_{SUB}$ thereby pinning the Fermi level to the E_{ICT-} state by follow formula (2-3)

$$\Phi_{SUB} < E_{ICT-} \tag{2-3}$$

Fermi level pinning to a negative ICT state, substrate-independent resulting work function $\Phi_{ORG/SUB}$

Consequently, according to the following ICT model, so that have Ohmic contact injection the work function of substrate should be designed to be larger than the E_{ICT+} state for hole injection and smaller than the E_{ICT-} state for electron injection. However, The ICT states include not only both electronic and geometrical relaxations, but substrate, hence molecules in the bulk are located in a potentially different environment than molecules close the interface.

2.3 Metal-organic interface with interfacial dipole

For an intrinsic semiconductor, the work function is defined by metal within a semiconductor close to the interface. (**Figure 2.3**) as electron in the metal occupy state up metal Fermi edge, the distance between Φ_M and the HOMO (or valence band) transport level describes the energy barrier for holes (Φ_h) (or electrons, Φ_e) under the estimate of vacuum level alignment by Schottky-Mott theory. This energy barrier can be changed by interfacial dipole, which can be made deliberately such as organic surface modifiers. The field between the two dipole charges is mostly located between them and obvious in the potential by and offset in the vacuum level (E_{vac}) and a following shift of energy level. Such dipoles are introduced intendedly by self-assemble monolayer. If the work function of metal is higher or lower than EA of the semiconductor by interfacial dipole direction, resulting of shift vacuum energy level, as shown in **Figure 2.3**[27] the charge direction at the interface constitutes the dipole leading to alignment.

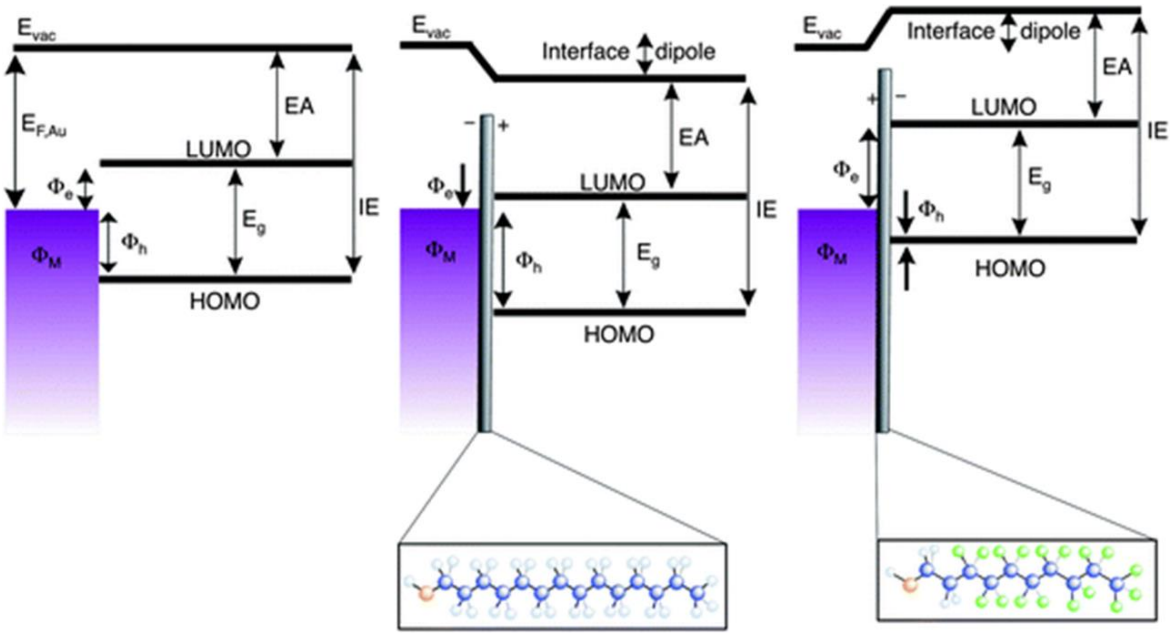

Figure 2. 3. Schematic vacuum level alignment with interfacial dipole at the metal-organic interface.

2.4 Working principle of charge selective interfacial layer

OSCs are often fabricate the basis of two types of device architecture. In the conventional types approach, the bulk heterojunction (BHJ) active layer is sandwiched between an ITO anode and low work function metal cathode, such as Al. The low work function metal electrode is easily oxidation in ambient air, the inverted types can be implemented to increase stability in which metal oxide interfacial layer such as titanium oxide or zinc oxide is inserted between the ITO and BHJ active layer. The top metal anode is used a more air stable, high work function metal electrode such as Au. In both types of architectures, the nature of electrical contact between the BHJ active layer and the electrodes is a critical factor that determines device characteristics. The series resistance (R_s) in a solar cell is attributed to the bulk conductivity of each of the interfacial layers and the contact resistance between them. Therefore, with high charge carrier materials and ohmic contact at the interfaces are required to obtain high J_{sc}. Also, V_{oc} can be increased by Fermi level alignment of both electrodes to HOMO of the donor and LUMO of the acceptor, respectively. Another parameter, the shunt resistance (R_{sh}), is determined by the active layer films quality and interface. Low R_{sh} result from the loss of charge carriers through leakage paths including voids in the films, the recombination and trapping of the carriers during their transport through the layer leading to a decrease in device efficiency.

While the BHJ active layer is an important component of high performance OSCs, the basic BHJ device that the electrodes are in direct contact both electron and hole abundant domains in the BHJ active layer. Therefore, it is possible to charges collected in the electrodes to recombination with oppositely charged carriers found in the interface. as shown in **Figure 2.4**

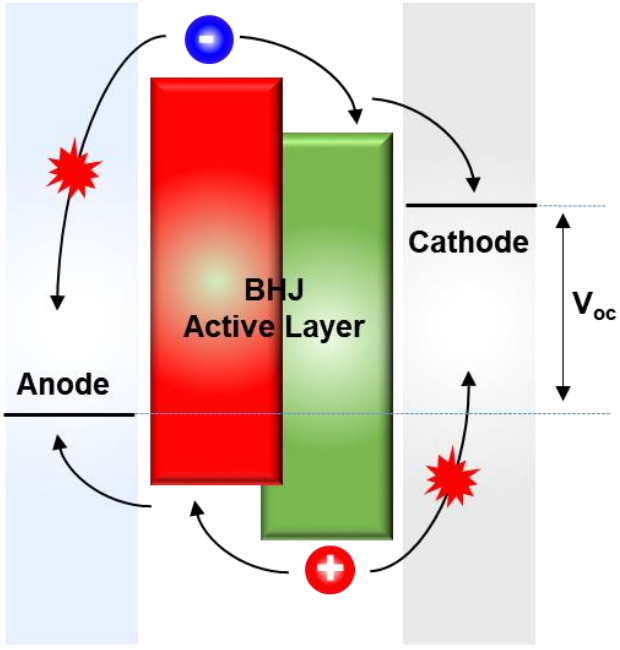

Figure 2. 4. Schematic energy band diagram of BHJ.

If charge selective interfacial layer (such as electron transport layer, ETL or hole transport layer, HTL) is inserted between the metal electrode (or ITO electrode) and BHJ active layer are spatially separated, the recombination can be effectively reduced. In short, the interfacial layer provides an intermediate energy barrier to prevent carriers from diffusing in the wrong direction. In addition, interfacial layer prevents inadvertent a variety of physical or chemical interactions between adjacent layers and act as optical spacers.

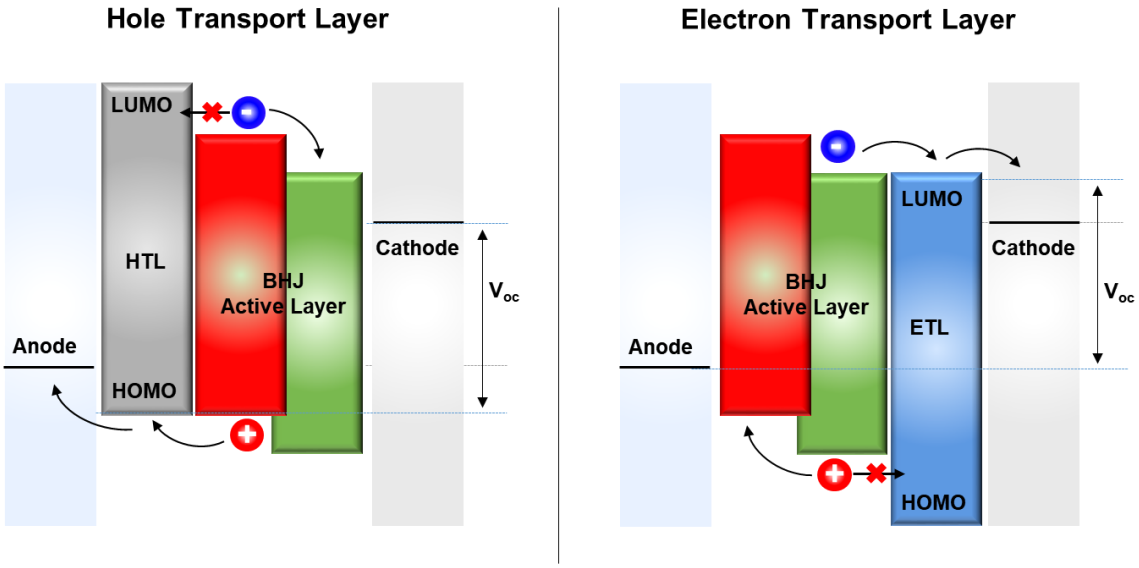

Figure 2. 5. Schematic energy band diagram of HTL and ETL.

Additionally, it is possible to increase the V_{oc} in the device using the ETL. If the LUMO of the ETL is aligned with the LUMO of the acceptor, and the ETL has a work function which is equal to or higher than LUMO of the acceptor, and then V_{oc} becomes aligned by the LUMO of the acceptor. Likewise, high LUMO energy of the HTL can prevent electron from diffusing reverse collected to the anode, and HOMO of HTL is aligned HOMO of donor can increase the V_{oc} by effectively deepening the work function of the anode. Thus, interfacial layer constitutes indispensable layer in OSCs.[28] as shown in **Figure 2.5**

CHAPTER 3. An Organic Surface Modifier to Produce a High Work Function Transparent Electrode for High Performance Polymer Solar Cells

3.1 Research background

The development of new conjugated polymers and device architectures have contributed to a dramatic improvement in device performance of polymer solar cells (PSCs), achieving power conversion efficiencies (PCEs) over 11%.[29-41] Until recently, efforts have focused on developing new charge transport layers to facilitate electron/hole transport from the active layer to cathode/anode. For conventional PSCs, poly(3,4-ethylenedioxythiophene):poly-styrene sulfonate (PEDOT:PSS) is widely used as hole transport layer (HTL) because of its solution-processability, excellent wettability to both indium tin oxide (ITO) surface and active layer solution, appropriate work function for producing an Ohmic contact between the active layer and ITO anode.[42-44] However, the acidic nature of PEDOT:PSS is detrimental to device stability due to chemical instability at the ITO/active layer interface by indium diffusion into the active layer.[45, 46] In addition, PEDOT:PSS layer has a weak absorption in the visible and near IR wavelength regions, reducing light absorption within the active layer.[43, 47, 48] To overcome these drawback, p-type metal oxides including vanadium oxide, molybdenum oxide, and ruthenium oxide have been developed as efficient HTL instead of PEDOT:PSS.[43, 44, 47-49] Although these metal oxides have high hole mobility and relatively high transparency in the visible spectral range, thermal annealing at 150 °C and UV-ozone treatment are required to complete the transformation into metal oxides. As an alternative, organic surface modifiers such as conjugated polyelectrolytes (CPEs) and self-assembled monolayers (SAMs) have been explored.[42, 50, 51] These enable device fabrication on flexible substrates using only low-temperature solution processing.

Small-molecule organic surface modifiers with functional groups that can form SAMs on the surface of metal oxides via chemical absorption have been utilized to modify the surface properties of metal oxides and alter the work function of the electrodes.[52-57] Beaumont *et al*. introduced various organic materials with electron withdrawing halogens (F, Cl, and Br) and carboxylic acid (or phosphonic acid) groups at the interface between electron donor and ITO anode in chloroaluminium phthalocyanine/C_{60} heterojunction solar, thereby controlling the work function and surface energy of ITO electrode.[56] Recently, Knesting and Wang *et al*. reduced contact resistance between inorganic metal oxide and organic active layer by incorporating a fluorinated SAM on the ITO surface instead of PEDOT:PSS, thereby improving the open-circuit voltage (V_{OC}) of bulk heterojunction (BHJ)

PSCs.[50, 51] Compared to polymer-type HTLs such as PEDOT:PSS and CPEs, the devices with small-molecule organic surface modifier may be cost-effective and air-stable. Unnecessary synthetic routes and purification processes are avoided, and they have neutral pH. However, they require immersing in solution for long times (> 20 hours) to form the SAM on the substrate. In addition, there have been no reports on high performance PSCs using only small-molecule organic surface modifier instead of polymer- and metal oxide-type HTLs.

3.2 Experimental details

Device fabrication

ITO substrates were sequentially cleaned with detergent, DI water, acetone, and 2-propanol via sonication for 10 min each. For PEDOT:PSS layer, PEDOT:PSS solution (Clevios™ P VP AI 4083, Heraeus) was spin-coated at 5000 rpm on cleaned ITO substrates after UV-ozone treatment for 10 min and dried at 140 °C for 10 min. For thin layer of 4-chlorobenzoic acid (CBA, Sigma-Aldrich Corp.), CBA solution dissolved in methanol with concentration of 1 mg/ml was spin-coated at 3000 rpm on UV-ozone treated ITO substrates. After transferring samples into nitrogen-filled glove box, blend solution consisting of PTB7 (10 mg/ml) and $PC_{71}BM$ (15 mg/ml) dissolved in mixed solvent of chlorobenzene (CB) and 1,8-diiodooctane (DIO) (97:3 vol%) was spin-cast at 1200 rpm on top of PEDOT:PSS and CBA layer. Subsequently, Al electrode with a thickness of 100 nm was deposited on the active layer under vacuum ($5x10^{-6}$ Torr) via thermal evaporation

Device characterization

The *J-V* characteristics of the solar cells were measured by a Keithley 2400 Source Measure Unit. The solar cell performance was tested with an Air Mass 1.5 Global (AM 1.5 G) solar simulator with an irradiation intensity of 100 mW cm^{-2}. In order to test the solar cells under various light intensities, the intensity of the light was modulated with a series of two neutral density filters wheels of six filters apiece, allowing for up to 10 steps in intensity from 100 to 1 mW cm^{-2}. EQE measurements were obtained using the PV measurement OE system by applying monochromatic light from a xenon lamp under ambient conditions. The monochromatic light intensity was calibrated using a Si photodiode and chopped at 100 Hz. Masks (3.43 mm^2) made of thin black plastic were attached to each cell before measurement of the *J-V* characteristics and the EQE to accurately measure the performance of solar cells. All devices were tested in ambient air after UV-epoxy encapsulation.

3.3 Results and discussion

In this work, we report efficient PSCs with PCE = 8.48% by incorporating chlorobenzoic acid (CBA) as the small-molecule organic surface modifier applied by simple spin-coating to produce a high work function ITO electrode **(Figure 3.1)**. The CBA modification increases the work function of metal oxides and makes their surface hydrophobic.[56] Devices modified with CBA via spin-coating achieved higher PCE than control devices with PEDOT:PSS. This improvement is attributed to increased light absorption within the active layer because of higher transparency in visible wavelength region, efficient hole extraction from the active layer to anode by cascade energy level alignment, and reduced contact resistance at the ITO/active layer interface.

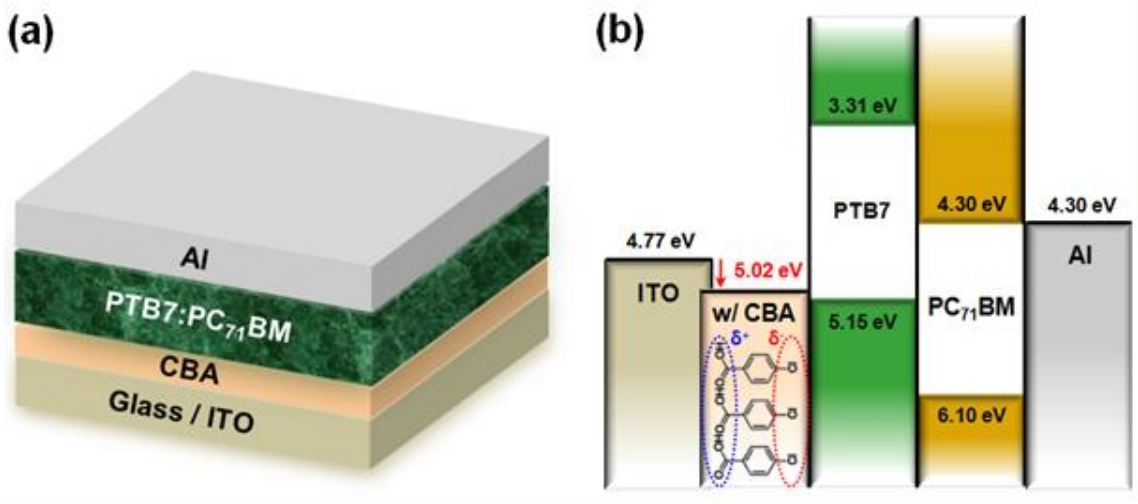

Figure 3. 1. (a) Device structure and (b) energy-band diagram of the devices incorporating CBA layer between ITO and the active layer.

To control the work function and modify surface property of ITO electrode, we introduced CBA at the interface between ITO and the active layer. CBA modification of the ITO electrode exhibited an increased work function and made the ITO surface more hydrophobic, The former was confirmed by ultraviolet photoelectron spectroscopy (UPS), and the latter was confirmed by contact angle measurement as shown in **Figure 3.2** and **Figure 3.3**, respectively. The hydrophilic carboxylic acid moiety of CBA tends to be located toward ITO surface, while the chlorine group with electron withdrawing property is located toward the active layer, leading to interfacial dipoles pointing toward the active layer **(Figure 3.1b)**. As a result, ITO modifications with CBA increased the work function of ITO from 4.77 eV to 5.02 eV; i.e. to a value comparable to that of PEDOT:PSS (5.16 eV). The formation of an Ohmic contact improved hole transport from the active layer to anode **(Figure 3.1b** and **Figure 3.2)**.

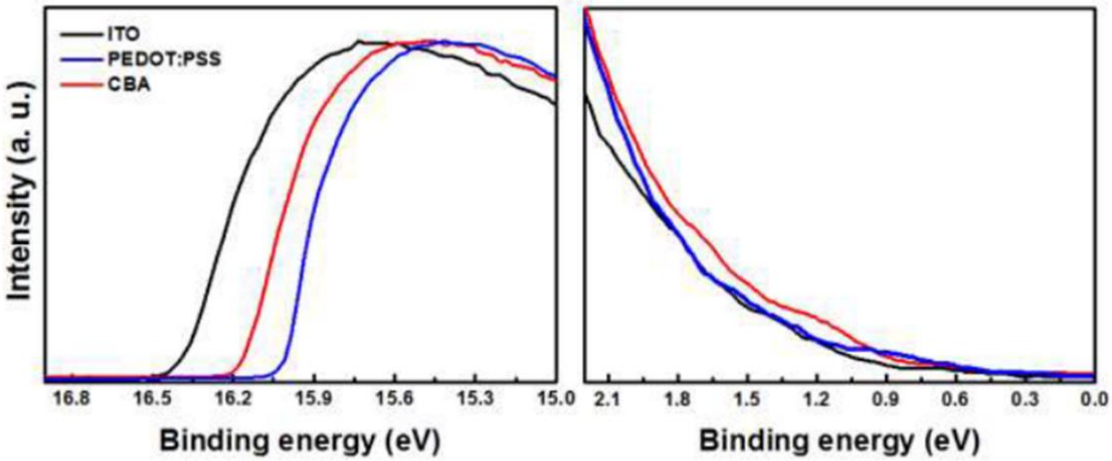

Figure 3. 2. Ultraviolet photoelectron spectra of bare ITO, PEDOT:PSS, and CBA spin-coated on top of ITO substrates. Calculated work functions were 4.77 eV, 5.16 eV, and 5.02 eV for bare ITO, PEDOT:PSS, and CBA, respectively**.**

In contact angle measurements, bare ITO and PEDOT:PSS-modified ITO had contact angles of 11.5° and 19.2°, respectively, whereas CBA-modified ITO exhibited contact angle of 67.7° (**Figure 3.3a-c**). These data imply that hydrophobic surface induced by CBA modification is more compatible with hydrophobic active layer solution than hydrophilic UV-ozone-treated ITO and PEDOT:PSS. We also compared surface morphology of ITO electrodes modified with PEDOT:PSS and CBA by measuring tapping mode atomic force microscopy (AFM). Compared to bare ITO (root-mean-square (rms) roughness: 0.63 nm), PEDOT:PSS led to uneven surface with rms roughness of 0.97 nm, whereas CBA modification exhibited unchanged surface morphology with rms roughness of 0.51 nm **(Figure 3.3d-f)**. Negligible morphology differences were observed between bare ITO and CBA-modified ITO, implying that ultrathin CBA layer (< 5 nm) was uniformly formed on ITO surface. This was confirmed by X-ray photoelectron spectroscopy (XPS) **(Figure 3.4)**.

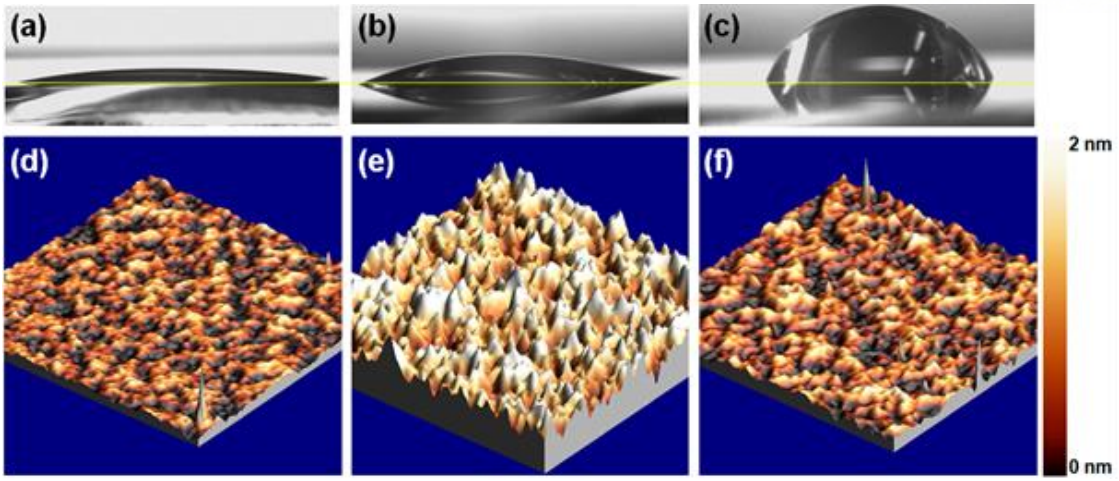

Figure 3. 3. Contact angle (upper row) and 3D AFM topography images (lower row) of bare ITO (a, d) PEDOT:PSS (b, e), and CBA (c, f) spin-coated on top of ITO substrates. The AFM imaging size is 3 μm x 3 μm

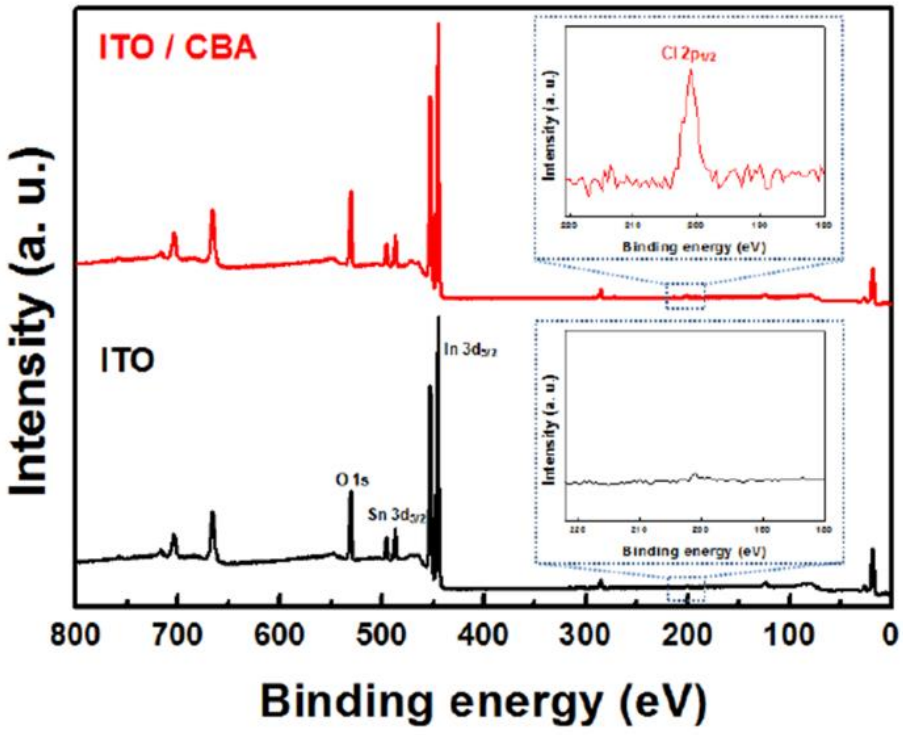

Figure 3. 4. X-ray photoelectron spectroscopy (XPS) spectra of bare ITO and CBA-modified ITO substrates. The inset shows Cl 2p1/2 peak, which is attributed to chlorine moiety of CBA.

We also compared the transmittance of ITO with PEDOT:PSS and CBA modification. In comparison with PEDOT:PSS spin-coated on ITO substrate, CBA-modified ITO exhibited lower transmittance in UV region (350-500 nm) and higher transmittance in visible region (500-700 nm)

(Figure 3.5a). The transmittance spectra of ITO and PEDOT:PSS were consistent with previously reported results.[47, 48] Replacing PEDOT:PSS with CBA can enhance device performance by improving light absorption within the active layer because visible light (44%) comprises a higher fraction of the solar radiation spectrum than UV light (7%).[58] To verify the CBA effect on light absorption, we measured absorption spectra of the active layer spin-coated on ITO substrates modified with PEDOT:PSS and CBA using the following BHJ system: poly[[4,8-bis[(2-ethylhexyl)oxy]benzo[1,2-b:4,5-b']dithiophene-2,6-diyl][3-fluoro-2-[(2-ethylhexyl)carbonyl]-thieno-[3,4-b]thiophenediyl]] (PTB7) as the electron donor and [6,6]-phenyl-C_{71} butyric acid methyl ester ($PC_{71}BM$) as the electron acceptor within the active layer. As expected from the transmittance results, the BHJ film on PEDOT:PSS had higher absorption in the range of 400-530 nm, whereas the BHJ film on CBA exhibited increased light absorption in the range of 550-750 nm **(Figure 3.5b)**. Interestingly, we observed a pronounced shoulder at 670 nm in the film on CBA, which may be attributed to optical interference and/or enhanced intermolecular orientation of polymer chains on hydrophobic CBA surface. The AFM topography images of BHJ films on different substrates indirectly supported this hypothesis **(Figure 3.6)**. Although all BHJ films had the same thickness of 130 ± 10 nm, the film on CBA was uniform with rms roughness of 1.2nm. Specifically, enhanced light absorption within the active layer resulted from higher transparency in the visible wavelength region as well as improved film morphology by hydrophobic CBA layer.

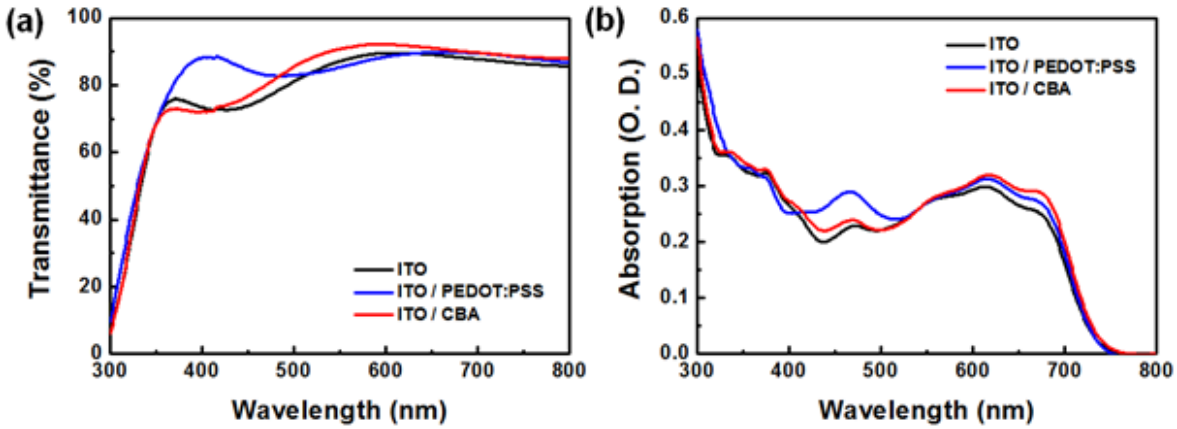

Figure 3. 5 (a) Comparison of transmittance between PEDOT:PSS and CBA on ITO substrate. (b) UV-vis absorption spectra of PTB7:$PC_{71}BM$ active layer on top of different substrates.

To verify the merits of CBA in real devices, we fabricated PSCs using the simple device configuration of ITO/PEDOT:PSS or CBA/PTB7:$PC_{71}BM$/Al **(Figure 3.1a)**. We also prepared a control device without any ITO modification for comparison. **Figure 3.7a** shows current density-voltage (*J-V*) curves of the devices with PEDOT:PSS and CBA. More than 40 devices were fabricated under each condition for device optimization. Predictably, the control device showed poor device

performance due to the absence of any HTL. The device with PEDOT:PSS had a PCE = 7.53% with short-circuit current density (J_{SC}) of 15.28 mA cm^{-2}, open-circuit voltage (V_{OC}) of 0.74 V, and fill factor (*FF*) of 0.67, which are comparable values with those of PTB7:$PC_{71}BM$ PSCs reported previously in the literature.[42, 59, 60] The device with CBA modification demonstrated a higher PCE = 8.48% than that of the device with PEDOT:PSS in spite of absence of a charge transport layer. V_{OC} and *FF* of the device with CBA (V_{OC}: 0.74 V and *FF*: 0.70) were similar to the device with PEDOT:PSS, whereas there was an improvement in J_{SC} (16.47 mA cm^{-2}). The detailed device parameters are summarized in **Table 3.1**.

Table 3. 1. Device parameters of PTB7:$PC_{71}BM$ PSCs with different ITO modification.

ITO modification	J_{SC} [mA cm^{-2}]	V_{OC} [V]	FF	Best PCE [%]	Average PCE [%]	J_{SC} (cal.)[a] [mA cm^{-2}]
None	14.96	0.62	0.61	5.67	5.33	14.88
PEDOT:PSS	15.28	0.74	0.67	7.53	7.31	15.63
CBA	16.47	0.74	0.70	8.48	8.19	16.53

[a] J_{SC} (Cal.): J_{SC} calculated from EQE curves.

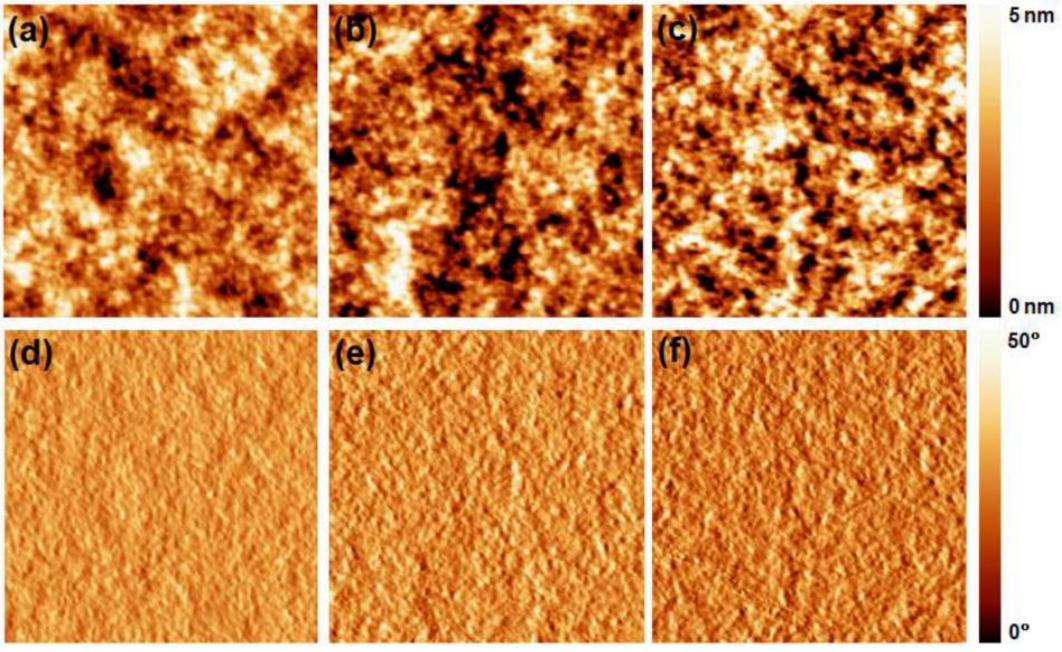

Figure 3. 6. AFM topography (a-c) and phase images (d-f) of PTB7:PC71BM blend films spincoated on top of bare ITO (a,d), PEDOT:PSS (b,e), and CBA (c,f).

To understand the enhancement of J_{SC} by replacing PEDOT:PSS with CBA, we measured the external quantum efficiency (EQE). The device with CBA showed higher EQE in the range of 550-750 nm and lower EQE in the range of 480-550 nm compared to the device with PEDOT:PSS **(Figure 3.7b)**. These EQE curves are in good agreement with the transmittance data obtained from PEDOT:PSS- and CBA-modified ITO substrates **(Figure 3.5a)** and UV-vis absorption spectra of PTB7:$PC_{71}BM$ films spin-coated on them **(Figure 3.5b)**. The high transparency in the visible region yielded EQE values approaching 80% in the spectral range from 610 nm to 680 nm, thereby giving rise to higher J_{SC}.

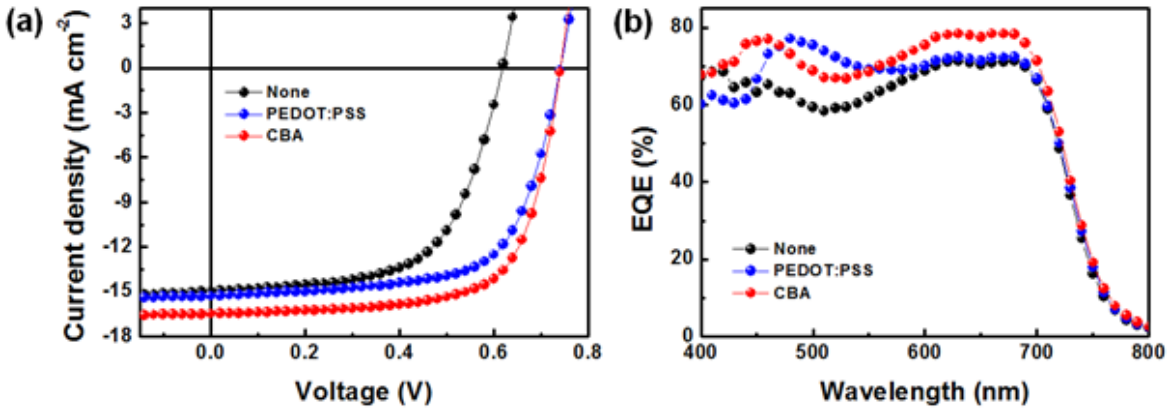

Figure 3. 7. (a) Current density-voltage (*J-V*) curves and (b) external quantum efficiency (EQE) of the devices with different ITO modification.

We also compared the stability of the devices with PEDOT:PSS and CBA in air atmosphere **(Figure 3.8)**. The control device exhibited longer device stability than the device with PEDOT:PSS. The efficiency of the device with PEDOT:PSS rapidly decreased because the acidic nature of PEDOT:PSS solution (pH value: 1.5-2.5 at room temperature) promotes corrosion within the device. In contrast, the device with CBA modification exhibited slower decrease in PCE and longer time air stability, consistent with the near-neutral pH of the CBA solution (pH value: 4-5).

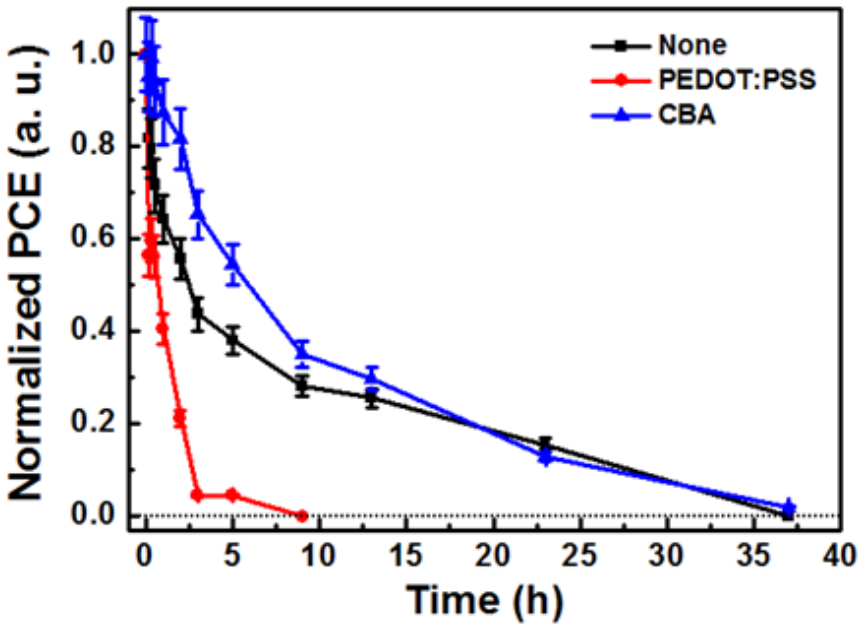

Figure 3. 8. Device stability of conventional-type PTB7:$PC_{71}BM$ PSCs with different ITO modification stored in air atmosphere condition without any encapsulation.

To elucidate the CBA effect on device performance, we investigated charge transport and recombination dynamics of the devices with PEDOT:PSS and CBA by measuring electrical impedance spectroscopy (EIS), dark *J-V* characteristics, dependence of V_{OC} on light intensity (V_{OC} vs light intensity), hole mobility obtained from hole-only device based on space-charge-limited current (SCLC) method. We measured EIS of the devices at V_{OC} condition under AM 1.5G irradiation (100 mW cm^{-2}). The EIS curve in the low frequency region depends on charge transport at the interface between active layer and electrode.[61] The devices with CBA exhibited slightly lower charge transfer resistance than the device with PEDOT:PSS, indicating that CBA effectively facilitates hole transport from the active layer to ITO anode **(Figure 3.9a)**. Dark *J-V* characteristics is also consistent with EIS results. The device with CBA showed low leakage current (approximately 10^{-3} mA cm^{-2}) and high rectification ratio (> 10^{5}), similar to those of the device with PEDOT:PSS **(Figure 3.9b)**.

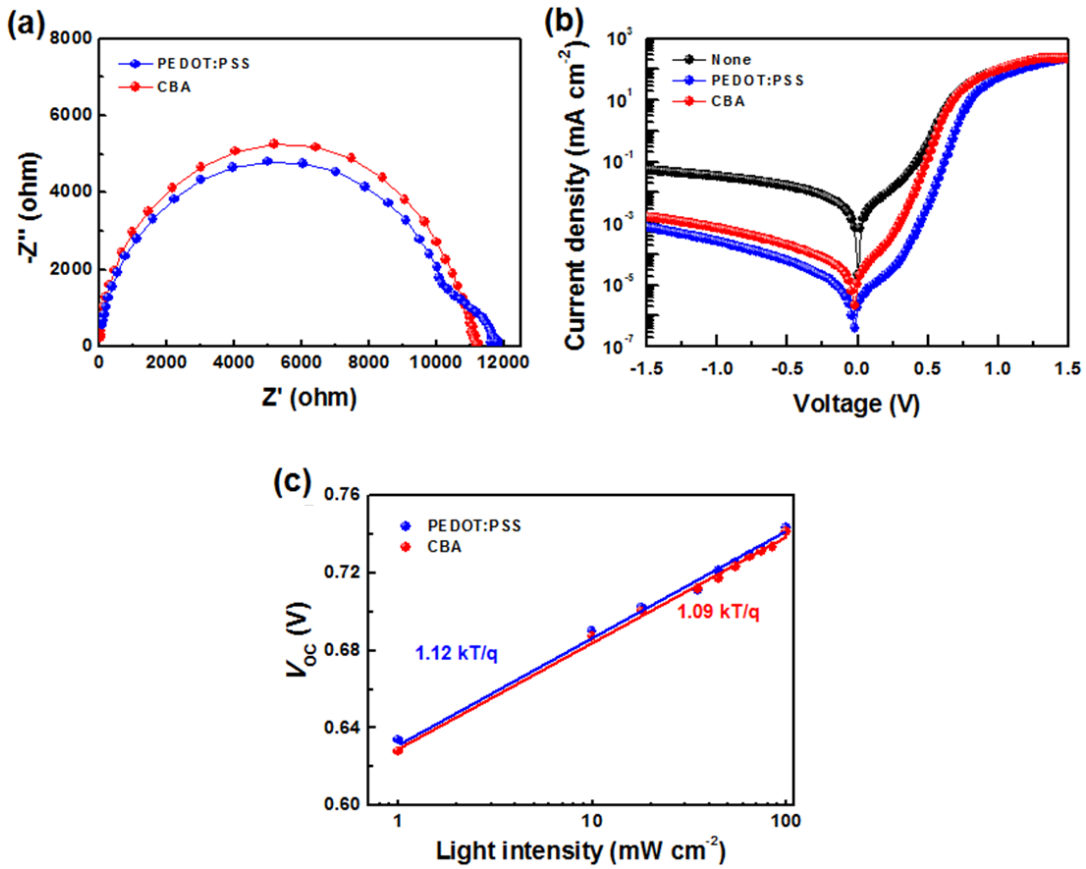

Figure 3. 9. a) Electrical impedance spectra, b) dark *J–V* curves, and c) V_{OC} dependence on light intensity of PTB7:PC 71 BM PSCs with PEDOT:PSS and CBA modification.

It is well-known that V_{OC} vs light intensity measurements provide information about trap-assisted recombination of the devices.[62-64] Semi-logarithmic plot between V_{OC} and incident light intensity exhibits linear relationship with a slope of kT/q, where k is Boltzmann's constant, T is Kelvin temperature, and q is elementary charge. The device with PEDOT:PSS and CBA exhibited V_{OC} dependence on light intensity with a slope of 1.12 kT/q and 1.09 kT/q, respectively **(Figure 3.9d)**. This V_{OC} vs light intensity measurement clearly shows that the device with CBA has minimized recombination at the interface between the active layer and ITO anode (at least comparable to the device with PEDOT:PSS). These various measurements confirm that CBA is an efficient organic surface modifier that can replace PEDOT:PSS by minimizing charge recombination and facilitating hole transport at the interface between the active layer and anode.

3.4 Conclusion

In conclusion, the small-molecule organic surface modifier CBA has been used to successfully produce ITO electrode with high work function and a hydrophobic surface. The device with CBA modification demonstrated PCE enhancement with measured values up to 8.48%. The increased PCE results from enhanced light absorption within the active layer by high transparency in visible range and the formation of an Ohmic contact for hole transport from the active layer to ITO anode by cascade energy level alignment. Furthermore, recombination loss is minimized. As an alternative to polymer- and metal oxides-type HTL, CBA is a promising organic surface modifier for flexible substrates and roll-to-roll mass-production because of its low cost and solution processability. In addition, CBA can be used as an intermediate layer for tandem solar cells because of its high transparency and excellent hole selectivity.

CHAPTER 4. Vapor Coating Method Using Small-Molecule Organic Surface Modifiers to Replace N-Type Metal Oxide Layer in Inverted Polymer Solar Cells

4.1 Research background

Polymer-fullerene bulk heterojunction (BHJ) polymer solar cells (PSCs) have been regarded as next-generation solar cells because of their advantages such as low-cost, light-weight, and flexible device fabrications.[65-68] Substantial efforts synthesizing new semiconducting polymers and metal nanoparticles, developing device architectures, and controlling the active layer morphology have improved power conversion efficiency (PCE) of conventional PSCs (cPSCs) up to 9%.[30, 34, 60, 69-71] In spite of dramatic improvement in device efficiency, there remained a major concern about device stability of cPSCs for commercialization.[72] Poor stability of cPSCs originates from acidic nature of poly(3,4-ethylenedioxythiophene):polystyrene sulfonic acid (PEDOT:PSS) and easily-oxidized low work function metal cathodes (e.g. calcium, aluminum).[45, 73] As an alternative solution, inverted PSCs (iPSCs) have been developed, where high work function metals (e.g. gold, silver) and metal oxides (e. g. titanium dioxide, zinc oxide, molybdenum oxide) were used as anode and electron/hole transport layer, respectively.[37, 68, 74-76] Metal oxides have been widely used for iPSCs because of high charge-carrier mobility and transparency in visible wavelength region.[77, 78] However, main drawbacks of metal oxides including inherent incompatibility between inorganic metal oxides and organic active layer, high temperature thermal treatment for calcinations, light absorption in UV region, and light interference effect, can limit the enhancement in device performance.[45, 54, 57, 79] To overcome these problems of metal oxides, polymer surface modifiers, such as polyethylenimine ethoxylated (PEIE) and poly[(9,9-bis(3′-(N,N-dimethylamino)propyl)-2,7-fluorene)-alt-2,7-(9,9-dioctylfluorene)] (PFN), have been employed to produce low function cathode without metal oxides layer in iPSCs.[68, 80, 81] In particular, PEIE layer deposited on top of various layers (metal oxides, metal, conducting polymer, and graphene, etc) via spin-coating method effectively reduced their work functions and exhibited excellent electron selectivity, leading to comparable device performance to the devices with metal oxide.[80] However, polymer surface modifiers require synthesis/purification process and should be dissolved in polar solvents (e.g. 2-methoxyethanol, methanol, isopropanol, etc) for spin-coating. In addition, its thickness should be adjusted for device optimization by controlling the solution concentration and spin-coating rate. In spite of demands for developing new surface modifiers and their coating methods, there have been no reports on small-molecule organic surface modifiers and new coating techniques for high performance iPSCs. (**Table 4.1**)

Table 4. 1. Comparison of our work with previous reports on inverted organic solar cells.

ETLs	Device configuration	J_{SC} [mA cm^{-2}]	V_{OC} [V]	*FF*	PCE [%]	*Ref.*
Metal oxide	ZnO/p-DTS(FBTTh2)2:PC70BM/MoOx/Ag	14.50	0.72	0.60	6.29	63
	ZnO(30nm)/PCDTBT:PC70BM/MoOx/Ag	10.41	0.88	0.69	6.33	75
	ZnO(60nm)/PTB7:PC70BM/MoO3/Au	13.40	0.71	0.65	6.26	82
	TiO2(30nm)/PTB7:PC70BM/MoO3/Ag	14.36	0.70	0.63	6.12	82
	TiO2:Cs/PTB7:PC70BM/MoO3/Ag	14.73	0.72	0.66	6.53	82
	ZnO(30nm)/PTB7:PC70BM/MoO3/Ag	14.72	0.72	0.69	7.22	74
	ZnO(40nm)/PBDT-DTNT:PC70BM/MoO3/Ag	15.20	0.69	0.55	6.10	83
	ZnO-R/PTB7:PC70BM/MoO3/Ag	13.70	0.71	0.69	6.71	84
	ZnO(50nm)/PTB7:PC70BM/MoO3/Au	12.50	0.74	0.65	6.00	This Work
Polymer surface modifier	PEIE(10nm)/p-DTS(FBTTh2)2:PC70BM/MoOx/Ag	12.60	0.77	0.54	5.18	63
	PFN(5nm)/PTB7:PC70BM/MoO3/Al	17.37	0.75	0.69	8.96	85
	PEIE(10nm)/PTB7:PC70BM/MoO3/Au	14.40	0.71	0.68	7.02	82
Metal oxide /buffer layer	ZnO/PEIE/p-DTS(FBTTh2)2:PC70BM/MoOx/Ag	15.20	0.77	0.67	7.88	63
	ZnO/PFN-Br/PBDT-DTNT:PC70BM/MoO3/Ag	17.40	0.75	0.61	8.40	83
	ZnO-R/polar solvent/PTB7:PC70BM/MoO3/Ag	16.76	0.71	0.73	8.69	84
Small molecule surface modifier	ETA-VC/PTB7:PC70BM/MoO3/Au	14.20	0.73	0.61	6.28	This Work
	ETA-VC/PTB7:PC70BM/MoO3/Au	14.23	0.73	0.67	6.99	

In this work, we demonstrate vapor coating method of small molecule-based organic surface modifier for high performance iPSCs. We chose ethanolamine (ETA) both as surface modifier of electrode and electron selective layer, since ETA is soluble in polar solvents and a volatile solvent as well as ETA can be easily deposited on ITO substrate via both spin- (ETA-SC) and vapor-coating (ETA-VC). The ETA treatment reduces work function of indium tin oxide (ITO) cathode, facilitates electron transport, and blocks hole transport from the active layer to cathode. Furthermore, ETA treatment maximizes light absorption within the active layer due to the absence of light absorption in UV region and interference by metal oxide layer, leading to enhancement in short-circuit current density (J_{SC}) and PCE.

4.2 Experimental details

PSCs fabrication and characterization.

ITO-coated glass substrates were cleaned by ultrasonication sequentially in deionized water, acetone and iso-propanol, and then dried in an oven for overnight. The ZnO precursor solution was prepared via sol-gel method.[86] For ZnO layer, this solution was spin-cast on ITO substrate at 3000 rpm for 25 sec and then annealed at 110 °C for 10 min. For ETA-SC, ETA solution dissolved in methanol (MeOH) (optimized concentration of 2 wt.%) and this solution was spin-cast on ITO substrate at 2000 rpm for 40 sec. To remove physically-adsorbed ETA molecules, ETA-SC-treated films were washed with pure MeOH by spin-coating MeOH on them, leading to formation of ETA monolayer (~5 nm). For ETA-VC, a few ETA droplets (40 μl) were dropped around ITO substrates inside Petri dish and closed lid. Subsequently, temperature elevated up to 50 °C and maintained it for 10 min. For deposition of the active layer, blend solutions of PTB7 (1 wt.%):$PC_{70}BM$ (1.5 wt.%) dissolved in mixed solvent of chlorobenzene and 1,8-diiodooctane were spin-coated on top of the different layer in a nitrogen-filled glove box. The thickness of the active layer was measured to be about 190 nm. The device was then pumped down under vacuum (< 10^{-6} Torr), and the p-type MoO_3 (5 nm) and Au (80 nm) electrode were then deposited on top of the active layer via thermal evaporation. The area of the Au electrode defines an active area of the device as 13.0 mm^2. For the characterization of PSCs, their current density-voltage (*J-V*) characteristics were measured using a Keithley 2635A Source Measure Unit. The solar cell performance was tested with an Air Mass 1.5 Global (AM 1.5 G) solar simulator under an irradiation intensity of 100 $mW \cdot cm^{-2}$. The EQE measurements were obtained using a PV measurement QE system by applying monochromatic light from a xenon lamp under ambient conditions. The monochromatic light intensity was calibrated using a Si photodiode and chopped at 100 Hz. A mask (13.0 mm^2) made of thin metal was used for *J-V* characteristics and EQE measurements.

Characterization of ITO electrodes with ZnO or ETA treatment.

Work function of ITO electrodes with ZnO layer and ETA treatment were obtained via ultraviolet photoelectron spectroscopy using He I (21.22 eV) radiation line from a discharge lamp. The AFM images (1.5 μm × 1.5 μm) were obtained using a VeecoAFM microscope in a tapping mode. Reflectance spectra were measured on a Varian Cary 5000 spectrophotometer and contact angle measurements were performed using DSA 100 instrument. Contact angles were measured using DSA100 (KRUSS, Germany). The impedance spectra were measured using electrical impedance spectroscopy (SI 1287 Solartron). The oscillation amplitude of the AC voltage was maintained at 10 mV for all impedance measurements.

4.3 Results and discussion

Figure 4.1a and **4.1b** show device structure and energy-band diagram of iPSCs with ZnO layer or ETA treatment, respectively. The ZnO nanoparticles were prepared via sol-gel method.[86] The ZnO layer was introduced between ITO and the active layer as an electron selective layer (**Figure 4.1a**) because of large band gap (3.2 eV) and well-matched energy levels with the components of the active layer (valence band of 7.8 eV and conduction band of 4.6 eV) to block hole extraction and facilitate electron transport from the active layer to cathode. For ETA-SC, ETA was dissolved in methanol (MeOH) and this solution was spin-coated on top of ITO substrate. Vapor-coating method is the similar to solvent annealing treatment of PSCs. After putting several ITO substrates in glass dish, 3~5 droplets (40 μl) of ETA were placed in the vicinity of substrates and covered the glass. Subsequently, temperature increased up to 50 °C and maintains it for 10 min. The details of ETA-SC and ETA-VC are described in the Experimental Section. As shown in **Figure 4.1b**, interfacial dipole by negative dipole moment of ETA-SC and ETA-VC shifts the vacuum level of ITO close to that of the active layer and effectively reduces work function of bare ITO (4.74 eV) to 4.52 eV and 4.48 eV, respectively (**Figure 4.2** and **Table 4.2**).

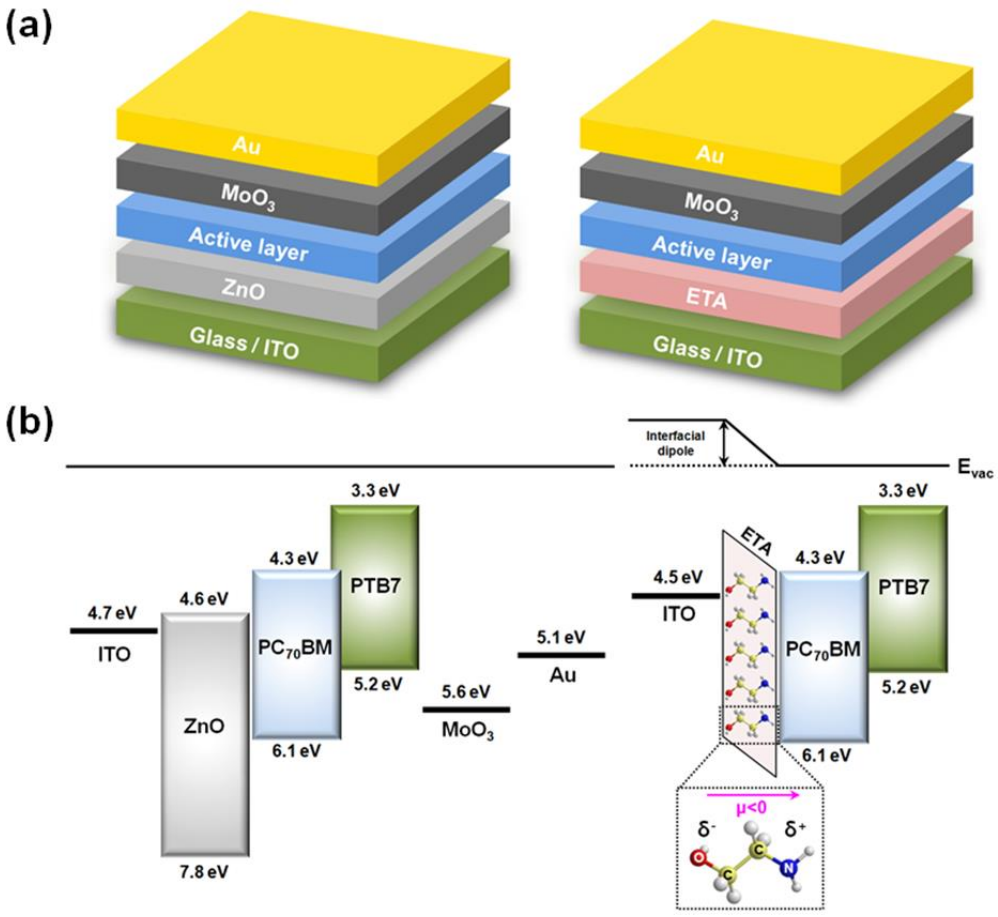

Figure 4. 1. (a) Device architecture and (b) energy band diagram of iPSCs with ZnO layer or ETA treatment.

This implies that only ETA treatment without metal oxide layer can facilitate electron transport from the active layer to cathode by reducing the energy barrier between them.

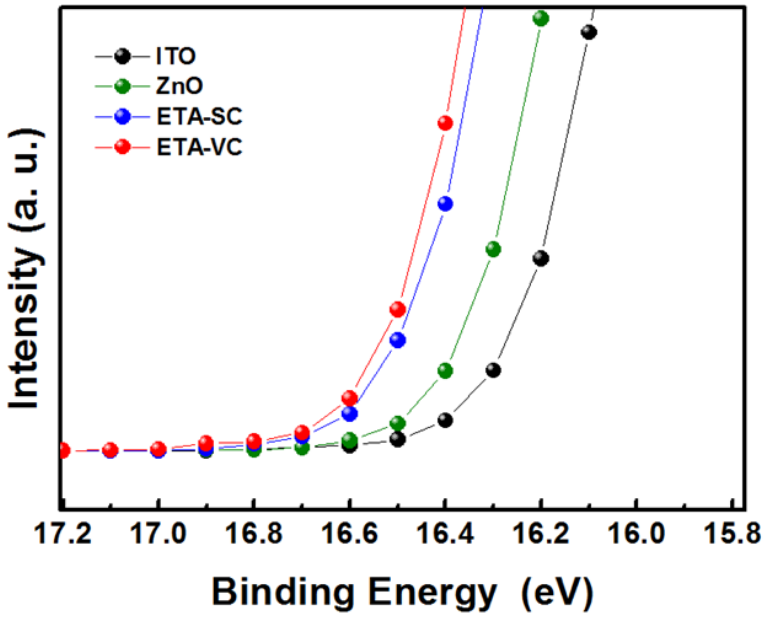

Figure 4. 2. Photoemission cutoff region obtained via UPS for ZnO-coated and ETA-treated ITO substrates.

To compare the effect of ZnO and ETA on device performance both as surface modifier and electron selective layer, iPSCs were fabricated using poly[[4,8-bis[(2-ethylhexyl)oxy]benzo[1,2-b:4,5-b']dithiophene-2,6-diyl][3-fluoro-2-[(2-ethylhexyl)carbonyl]-thieno-[3,4-b]thiophenediyl]] (PTB7) and [6,6]-phenyl-C_{70} butyric acid methyl ester ($PC_{70}BM$) as the active layer (**Figure 4.1a**). **Figure 4.3a** and **4.3b** exhibit current density-voltage (*J-V*) characteristics of PTB7:$PC_{70}BM$ iPSCs with different electron selective layer under AM 1.5 irradiation and dark condition, respectively. The device without any treatment was used as a reference. We also prepared the device with MeOH treatment to understand the only MeOH effect on device performance. There was negligible effect of MeOH treatment on device characteristics. The device with ZnO layer exhibited J_{SC} of 12.5 mA cm^{-1}, open-circuit voltage (V_{OC}) of 0.74 V, fill factor (*FF*) of 0.65, and PCE of 6.00%. Both ETA-SC and ETA-VC treatments instead of ZnO layer remarkably improved J_{SC} up to 14.20 mA cm^{-1}, whereas V_{OC} and *FF* remained almost similar (V_{OC} = 0.73 V, *FF* = 0.61 for ETA-SC and V_{OC} = 0.73 V, *FF* = 0.67 for ETA-VC). The detailed device characteristics are listed in **Table 4.3**.

Table 4. 2. Calculated work function of ITO substrates with different treatment.

	Bare ITO	**ZnO**	**ETA-SC**	**ETA-VC**
Work function (eV)	4.74	4.63	4.52	4.48

Compared to the device with ZnO, the device with ETA-SC showed decrease in *FF*, whereas there is slightly increased *FF* in the device with ETA-VC. Slight changes of *FF* by different treatments are consistent with differences in leakage current and rectification ratio of dark *J-V* characteristics (**Figure 4.3b**). These tendencies were also confirmed by series (R_s) and shunt resistance (R_{sh}) (**Table 4.3**). The PCE enhancement by both ETA-SC and ETA-VC treatments mainly resulted from ~14% increase in J_{SC}, which are clearly seen in EQE results (**Figure 4.3c**). Although the device with ZnO had the similar J_{SC} with reference device, we observed EQE curves with different shapes. The EQE values of the device with ZnO were lower in shorter wavelength region (below 560 nm) and higher in longer wavelength region (above 560 nm), compared to reference device. In contrast, both ETA-SC and ETA-VC treatment led to remarkable EQE enhancement over the whole wavelength region. Different shape of EQE curve and low EQE values of the device with ZnO may be attributed to combined effect of light absorption in UV region and light interference effect by ZnO layer. Since device stability in air condition is one of key factors for iPSCs, we also tested air stability of iPSCs with different electron selective layer over 120 h (**Figure 4.3d**). After air exposure of the devices with different electron selective layer for 120 h, reduction rate of device efficiencies were 32% for ZnO, 40% for ETA-SC, and 32% for ETA-VC, respectively. In spite of the absence of metal oxide layer, air stability of the devices with ETA-VC was comparable to ZnO device. Furthermore, ETA treatments are suitable for flexible devices and roll-to-roll mass production because of their solution processability at low temperature.

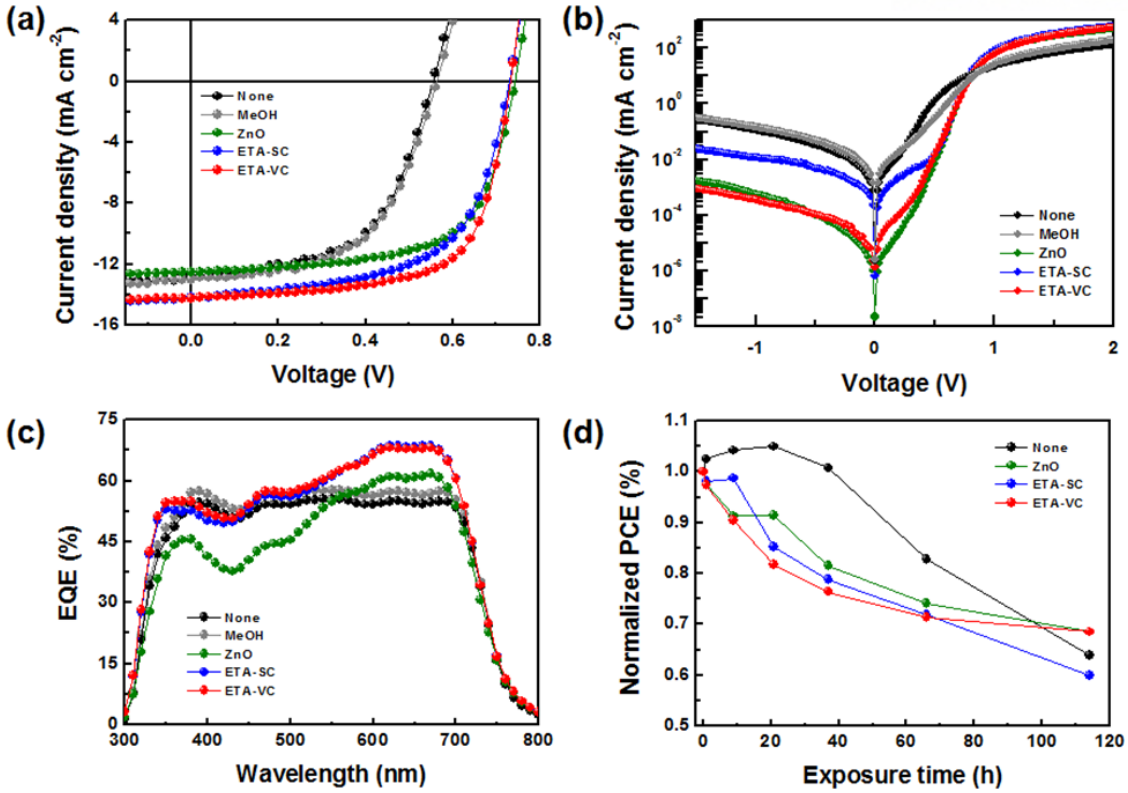

Figure 4. 3. *J-V* characteristics under (a) A.M. 1.5G illumination and (b) dark condition , (c) EQE, and (d) air stability of PTB7:$PC_{70}BM$-based iPSCs with different treatments.

Table 4. 3. Device characteristics of PTB7:$PC_{70}BM$-based iPSCs with different treatments.

Device configuration	J_{SC} [mA cm^{-2}]	V_{OC} [V]	*FF*	PCE [%]	J_{SC} [cal.] [mA cm^{-2}]	R_s[a] [Ω cm^2]	R_{sh}[a] [Ω cm^2]
ITO/PTB7:$PC_{71}BM$	12.90	0.56	0.56	4.02	12.50	1.53	270
ITO/MeOH/PTB7:$PC_{70}BM$	13.00	0.56	0.56	4.13	13.01	1.48	350
ITO/ZnO/PTB7:$PC_{70}BM$	12.50	0.74	0.65	6.00	12.11	1.10	791
ITO/ETA-SC/PTB7:$PC_{70}BM$	14.20	0.73	0.61	6.28	14.01	1.19	469
ITO/ETA-VC/PTB7:$PC_{70}BM$	14.23	0.73	0.67	6.99	14.08	1.02	1268

[a] R_s and R_{sh} were derived from the slope of *J-V* curves at open-circuit (I=0) and short-circuit (V=0) condition, respectively.

To understand the effect of ETA treatment on device performance, we investigated the changes in light absorption from reflectance measurements of the devices with different electron selective layer using three types of device configurations, which are the same structures with device fabrication (**Figure 4.4a**). **Figure 4.4b** exhibits reflectance spectra of the devices with different electron selective layer. The shapes of reflectance spectra were similar in all devices except for ZnO device. To clarify the changes in light absorption within the active layer by ZnO and ETA, we calculated absorption change (Δα) from the results of reflectance measurements (**inset of Figure 4.4b**).[30, 87] Compared to reference device, the device with ZnO layer showed significant decrease in light absorption by light interference, whereas both ETA treatments led to enhanced light absorption ranging from 400 to 750 nm. To find the origin of J_{SC} enhancement, we also compared the Δα and EQE enhancement (Δ EQE) by different ETA treatments. For calculation of Δ EQE, we subtracted corresponding EQE of the devices with ZnO layer from EQE of the devices with ETA treatments (**Figure 4.4c**). The Δ EQE spectra of ETA-SC and ETA-VC showed high and broad enhancement over the whole wavelength region, which were consistent with spectra of absorption change. This implies that enhanced J_{SC} by replacing ZnO with ETA originates from remarkable increase in light absorption within the active layer.

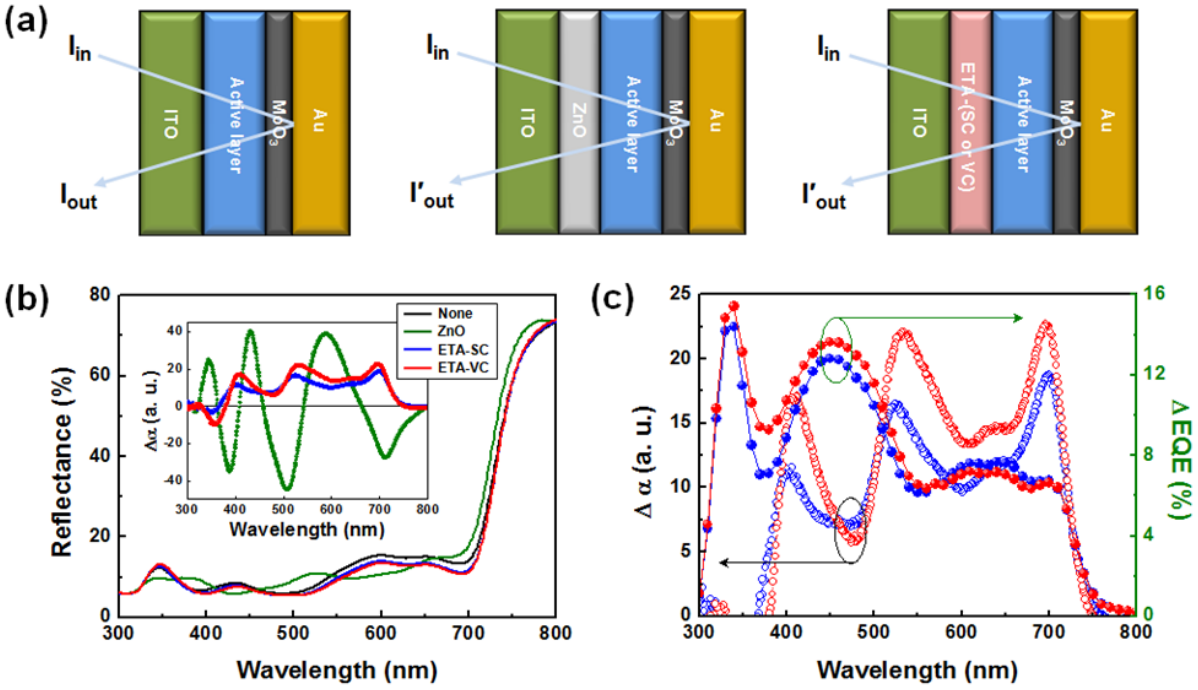

Figure 4. 4. (a) Device structures for reflectance measurement and (b) reflectance spectra of PTB7:$PC_{70}BM$-based iPSCs with different treatments. (c) Comparison of absorption change (Δα) with EQE enhancement (Δ EQE) by ETA-SC and ETA-VC treatments. The inset of Figure 3b shows Δα within the whole device architecute by ZnO layer or ETA treatment.

To investigate the changes in hydrophobicity and morphology of ITO surface by different treatments, we measured contact angles and atomic force microscopy (AFM) of ZnO-coated and ETA-treated ITO substrates (**Figure 4.5**). We prepared bare ITO as a reference. Reference ITO without UV ozone treatment showed contact of 79° (**Figure 4.5a**) and surface roughness of 0.80 nm (**Figure 4.5e**). After coating ZnO layer on ITO substrate, contact angle decreased to 33° (**Figure 4.5b**) and surface roughness also increased to 1.52 nm (**Figure 4.5f**). Compared to ZnO layer, both films with ETA-SC and ETA-VC treatment showed increased contact angles (SC: 44° and VC: 64°) (**Figure 4.5c and 4.5d**) and smooth roughness (SC: 0.48 nm and VC: 0.55 nm) (**Figure 4.5g and 4.5f**). For contact angle measurement of ETA-SC, combined effect of methanol and ETA led to resulting contact angle (**Figure 4.6**).

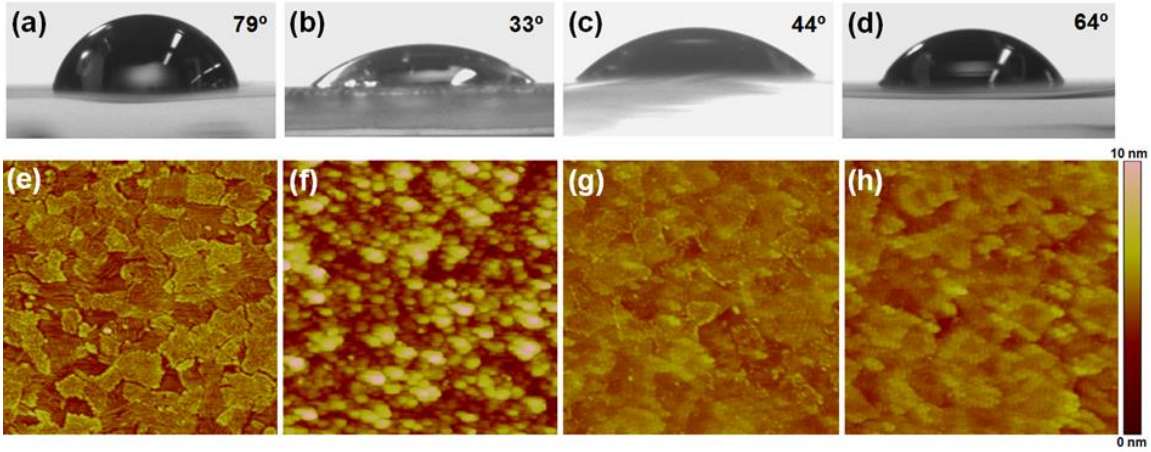

Figure 4. 5. Contact angle measurements (a-d) and AFM topography images (e-h) of bare ITO (a and e), ZnO-coated (b and f), ETA-SC-treated (c and g), and ETA-VC-treated (d and h) ITO substrates, respectively. AFM image size is 1.5 μm x 1.5 μm.

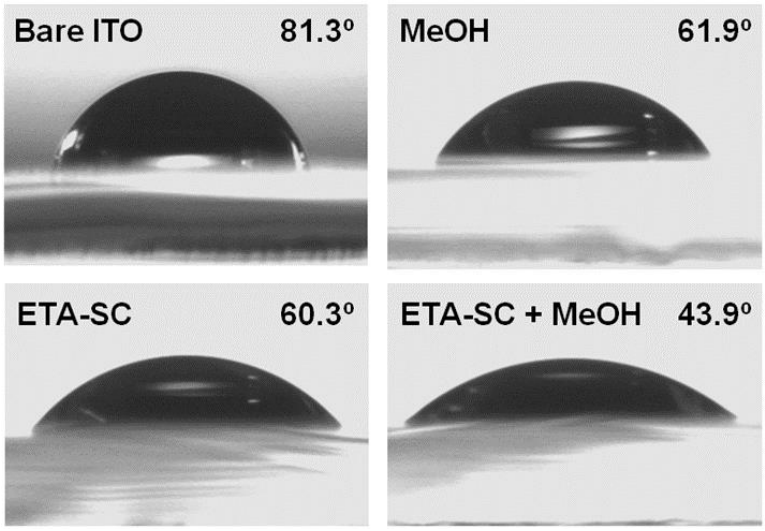

Figure 4. 6. Contact angles measurements of bare ITO and ITO substrates with MeOH, ETA-SC (before washing with MeOH), and ETA-SC + MeOH (after washing with MeOH) treatment.

To optimize the condition for ETA-VC, we fabricated the devices and measured contact angles as function of vapor time. Increasing the vapor time reduced J_{SC} and *FF*, which implies that lots of vapor adsorbed on ITO substrate is detrimental for device performance (**Figure 4.7** and **Table 4.4**). In contact angle measurements, there were negligible changes in contact angles by increasing vapor time (Δ contact angle between ETA-VC for 10 min and 90 min: 4°) (**Figure 4.8**).

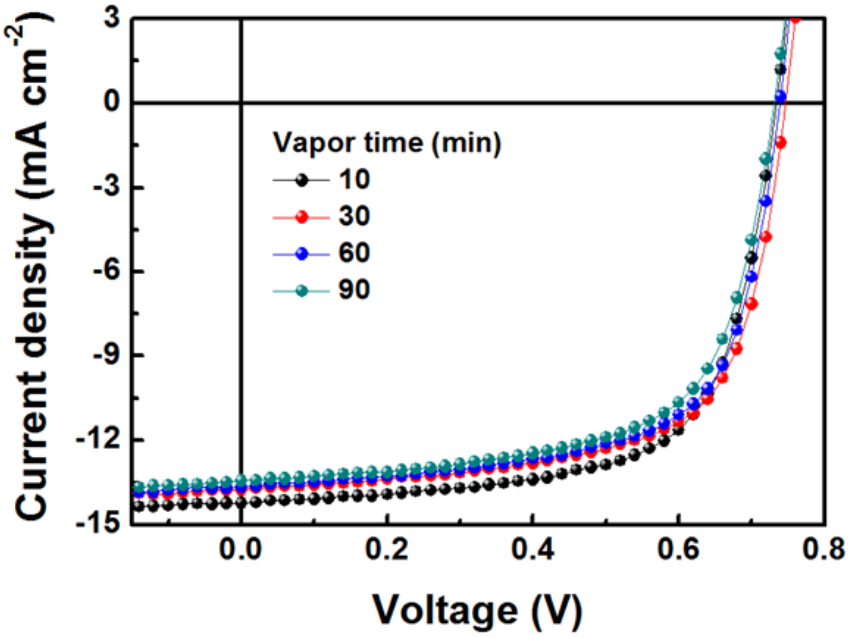

Figure 4. 7. *J-V* characteristics of PTB7:$PC_{70}BM$-based iPSCs with ETA-VC as a function of vapor time.

Table 4. 4. Device characteristics of the devices with ETA-VC as a function of vapor time.

Vapor time (min)	J_{sc} (mA cm^{-2})	V_{oc} (V)	*FF*	PCE (%)
10	14.23	0.73	0.67	6.99
30	13.77	0.75	0.67	6.84
60	13.65	0.74	0.66	6.65
90	13.43	0.73	0.65	6.36

Consequently, ETA-VC for 10 min is sufficient for depositing ETA molecules on ITO substrate and optimum condition for best device performance. Although ETA treatment increases hydrophobicity and makes the surface of electrode smoother, there are no effect of ETA treatment on morphologies and thickness of the PTB7:$PC_{70}BM$ active layer (**Table 4.5**). Root-mean-square roughness (1.50 ± 0.05 nm) and thicknesses (190 ± 25 nm) of upper active layer on ITO substrates with different treatments were almost identical regardless of ZnO and ETA treatments.

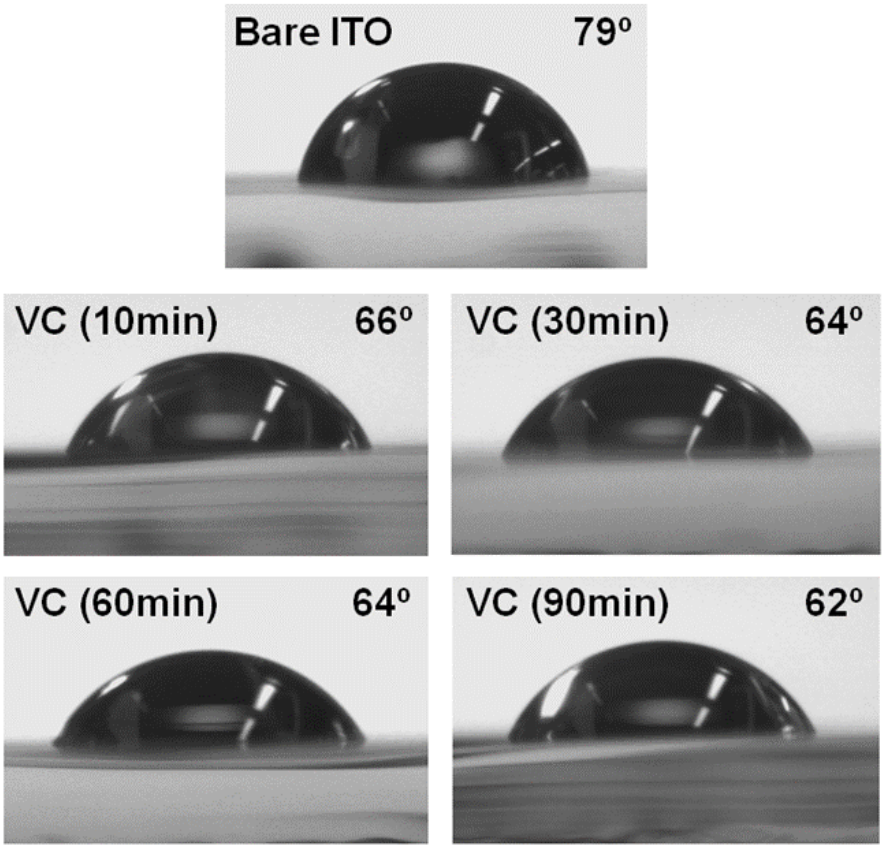

Figure 4. 8. Contact angles measurements of ITO substrates as a function of process time of ETA-VC.

Table 4. 5. Surface morphology and thickness of PTB7:$PC_{70}BM$ BHJ films spin-coated on different substrates.

	ITO	ITO / ZnO	ITO / ETA-SC	ITO / ETA-VC
Topography image	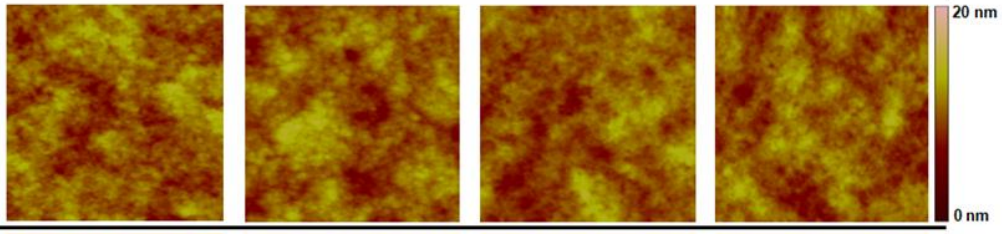			
Phase image	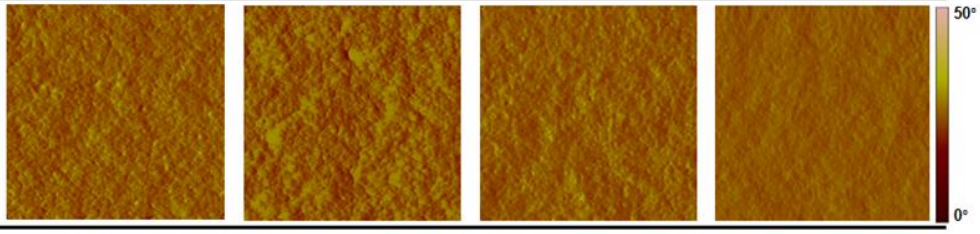			
Surface roughness (nm)	1.50±0.02	1.52±0.03	1.46±0.03	1.47±0.03
Thickness (nm)	190±20	190±15	190±15	190±15

To elucidate the influence of ETA treatment on recombination loss and charge transport between organic active layer and inorganic metal oxide, we measured the dependence of V_{OC} on the logarithm of the light intensity and electrical impedance spectroscopy (EIS). The light intensity dependence of V_{OC} provides the order of the recombination processes in BHJ PSCs.[62, 63, 88] Linear dependence of V_{OC} on light intensity with slope of kT q^{-1} was commonly observed in BHJ PSCs due to bimolecular recombination,

$$\delta V_{OC} = \left(\frac{kT}{q}\right) \ln(I) + constant \quad (4\text{-}1)$$

where k is Boltzmann's constant, T is Kelvin temperature, and q is the elementary charge.[62, 89] As shown in **Figure 4.9a**, the device with ETA-SC showed stronger dependence of V_{OC} on light intensity with slope of 1.20 $kT\,q^{-1}$ than ZnO device (1.09 $kT\,q^{-1}$). In contrast, the device with ETA-VC exhibited reduced dependence of V_{OC} on light intensity with slope nearly equal to 1.0 $kT\,q^{-1}$. Since strong dependence of V_{OC} on light intensity indicates high trap-assisted recombination, ETA-VC treatment remarkably reduced recombination at the interface of the active layer and ITO cathode, compared to ZnO and ETA-SC. The EIS results were also consistent with these data (**Figure 4.9b**). The device with ETA-SC showed higher charge transfer resistance (R_{CT}) than ZnO device, whereas ETA-VC treatment remarkably reduced R_{CT}. The decreases in trap-assisted recombination and R_{CT} by ETA-VC

treatment improves charge collection probability and electron transport from the active layer to cathode, leading to high J_{SC} and *FF*.

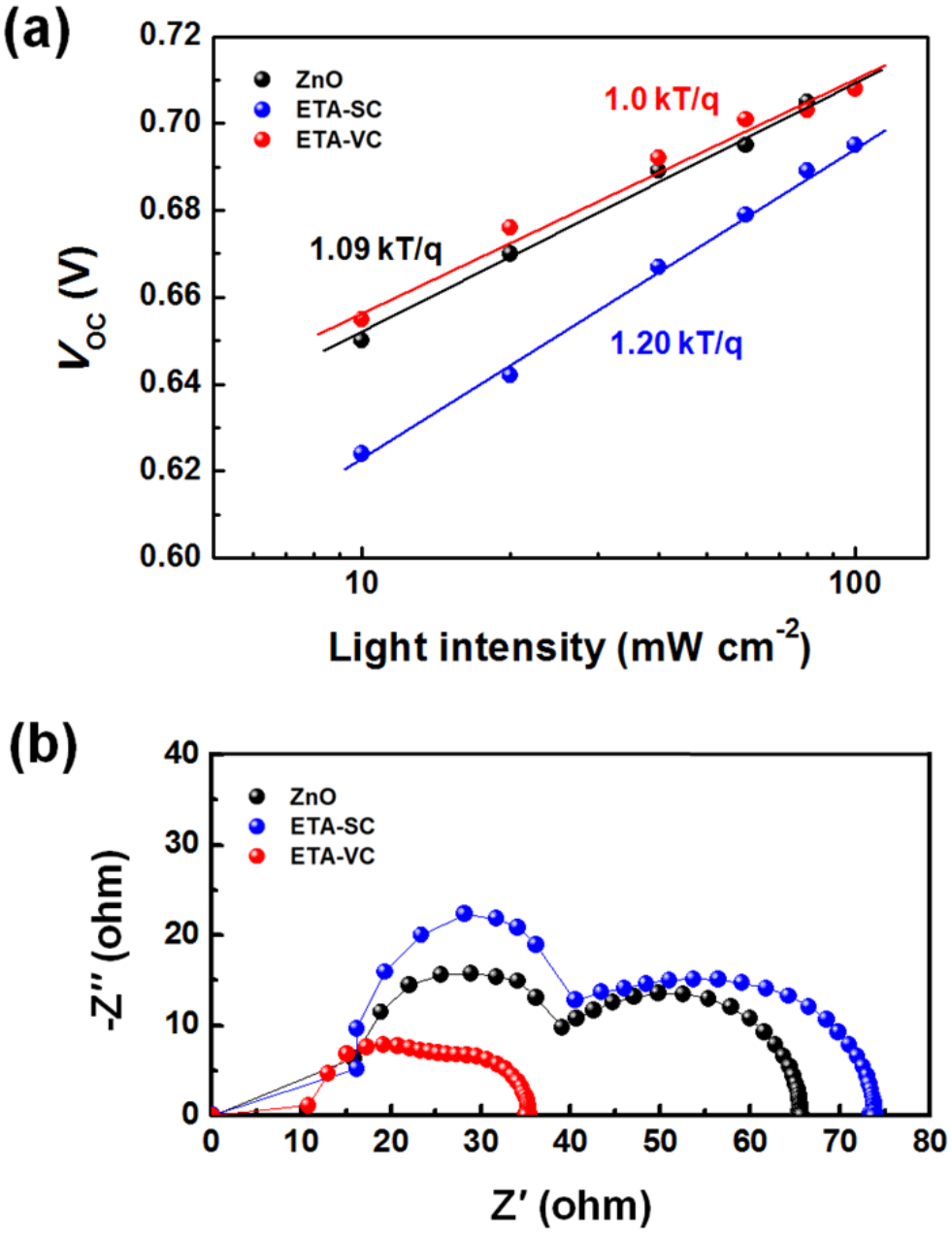

Figure 4. 9. (a) Dependence of V_{OC} on light intensity and (b) electrical impedance measurement of PTB7:$PC_{70}BM$ iPSCs with different treatments.

4.4 Conclusion

In conclusion, vapor coating method of ETA between the active layer and ITO electrode has been developed for high performance iPSCs. The ETA-VC treatment both as surface modifier for low work function electrode and electron selective layer reduces contact resistance and improves compatibility and electron transport between the active layer and ITO cathode while maximizing light absorption within the active layer, leading to remarkable enhancement in J_{SC} and PCE. This approach provides an effective way to apply to flexible devices and improve their device performance by replacing metal oxide layer with organic surface modifier in organic optoelectronic devices.

CHAPTER 5. Conjugated Polyelectrolyte Hole Transport Layer for High-Performance Inverted-Type Perovskite Solar Cells

5.1 Research background

Organic-inorganic hybrid perovskites have attracted considerable attention as possible next-generation thin-film solar cells because of advantages such as the low-cost of precursors, easy tuning of the bandgap, broad light absorption throughout the visible wavelength region, long exciton diffusion length, and solution-processability[18, 90-93]. Efforts dedicated toward improving device architectures and optimization of perovskite film morphology have improved power conversion efficiencies (PCEs) of perovskite solar cells (pero-SCs) up to 19%[94-99]. The fabrication of conventional pero-SCs, however, high-temperature annealing is required for the metal oxides (titanium oxide and zinc oxide are commonly used as the electron transport layer). The high-temperature annealing is not consistent with the use of flexible plastic substrates.

Table 5. 1. Summary of chemical structures, optical, electrochemical properties of various CPEs.

	CPE-K	CPE-Na	CPEPh-Na	PFBT-Na
Chemical structure	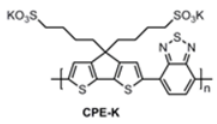 CPE-K	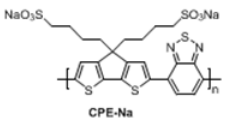 CPE-Na	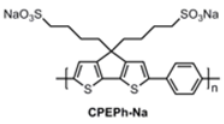 CPEPh-Na	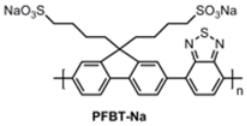 PFBT-Na
HOMO level (eV)	4.92	4.92	4.90	5.38
LUMO level (eV)	3.54	3.54	2.76	2.94
Optical bandgap (eV)	1.38	1.38	2.14	2.44
Film conductivity (S cm^{-1})	0.024	0.160	0.022	Not conductive

Inverted-type pero-SCs (ipero-SCs) have emerged as an alternative to conventional pero-SCs because of their low-temperature solution-processability. In this strategy, poly(3,4-ethylenedioxythiophene):poly-styrene sulfonate (PEDOT:PSS) is used as the hole transport layer (HTL). However, there is evidence that the acidic nature of PEDOT:PSS is detrimental to long-term device performance and stability[45]. As an alternative to PEDOT:PSS, inorganic HTLs previously

developed for polymer solar cells have been introduced into ipero-SCs. Docampo *et al.* reported that hole transport through vanadium oxide (V_2O_5) and nickel oxide (NiO) are comparable to that of PEDOT:PSS. However, ipero-SCs based on inorganic HTLs and methylammonium lead trihalide ($MAPbI_{3-X}Cl_X$)/[6,6]-phenyl-C_{61} butyric acid methyl ester (PCBM) planar heterojunction structures exhibited poor device performance due to incomplete surface coverage as a result of different surface energies of perovskite solution and V_2O_5 or NiO substrates[100]. Recently, ipero-SCs based on methylammonium lead iodide ($MAPbI_3$) achieved PCEs of ~9.5% by using mesoporous NiO as the HTL[101]. However, thermal annealing treatment over 400 °C was needed to convert amorphous NiO into nanocrystalline NiO films. Moreover, the power conversion efficiencies were still lower than those of the devices with PEDOT:PSS. It is therefore necessary to find new HTLs that are compatible with perovskite precursor solution and low-temperature solution-processing. To the best of our knowledge, there have been few reports on high-performance ipero-SCs using organic HTLs instead of PEDOT:PSS and p-type metal oxides[98, 102, 103].

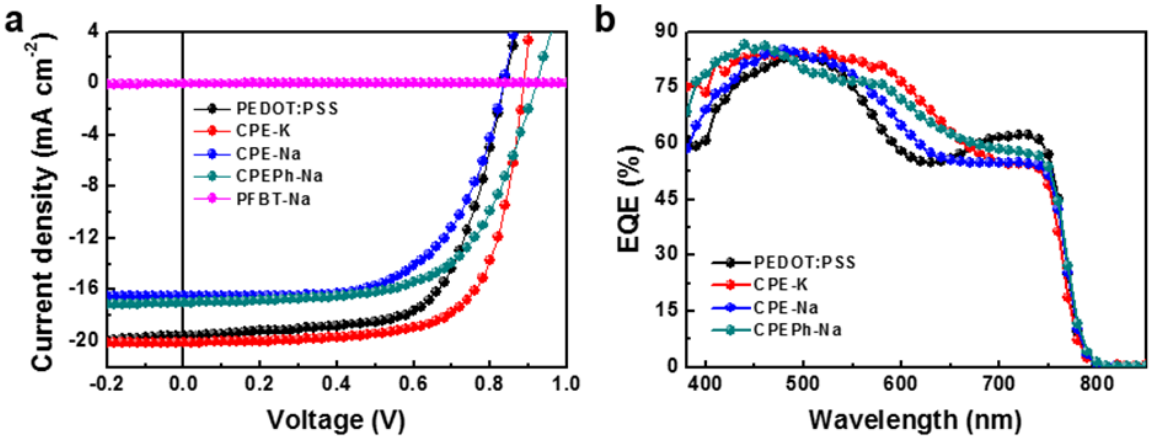

Figure 5. 1. (a) *J-V* curves and (b) EQE of ipero-SCs with different HTLs.

Here, we report ipero-SCs that take advantage of a novel pH-neutral and low-temperature solution-processable conjugated polyelectrolyte (CPE) as the HTL. Among various CPEs (**Table 5.1**), we employ a poly[2,6-(4,4-bis-potassiumbutanylsulfonate-4H-cyclopenta-[2,1-b;3,4-b']-dithiophene)-alt-4,7-(2,1,3-benzothiadiazole)] (CPE-K) because CPE-K results in highest PCE (**Figure 5.2** and **Table 5.2**), which is previously used in polymer solar cells[42]. These devices with CPE-K achieve a PCE of over 12% with enhanced device stability under ambient conditions. These improvements are attributed the excellent wetting of perovskite precursor solution on the CPE layer, efficient hole selectivity between the perovskite and indium tin oxide (ITO) anode, and pH-neutral CPE-K solution.

Table 5. 2. Device characteristics of ipero-SCs with different HTL.

HTL	J_{SC} (mA cm^{-2})	V_{OC} (V)	FF	PCE (%)
PEDOT:PSS	19.58	0.84	0.66	10.77
CPE-K	20.10	0.89	0.70	12.51
CPE-Na	16.48	0.84	0.62	8.52
CPEPh-Na	16.97	0.92	0.63	9.77
PFBT-Na	0.04	0.84	0.22	0.01

We employed four conjugated polyelectrolytes (CPEs) with different anionic polymer backbones and counter ions. Chemical structures and a variety property of these CPEs were listed in **Table 5.1**. To compare the effect of different CPEs on device performance, we fabricated ipero-SCs using CPEs as the HTL. **Figure 5.1a** and **Figure 5.1b** show *J-V* curves and EQE of the devices as a function of HTLs, respectively. The detailed device parameters are listed in **Table 5.2**. The device with PFBT-Na showed poor device performance, whereas CPE-Na and CPEPh-Na led to comparable PCE to that of the device with PEDOT:PSS. However, the devices with CPE-K exhibited highest PCE of 12.51% among various CPEs. Measured J_{SC} values from *J-V* curves were consistent with J_{SC} integrated from EQE curves (**Figure 5.1b**).

5.2 Experimental details

Preparation of perovskite precursor solution.

Lead chloride ($PbCl_2$) was purchased from Sigma-Aldrich and used without purification. Methylammonium iodide (MAI) was synthesized using synthetic routes in previous literature[97]. MAI and $PbCl_2$ with molar ratio of 3:1 were dissolved in *N,N*-dimethylformamide (DMF) at concentration of 40 wt.% and this solution was stirred at 60 °C for 6h in nitrogen-filled glovebox.

Film preparation and characterization.

We prepared perovskite films on different substrates for various measurements by using same procedures that were used for optimum devices. SEM images were obtained using FEI XL40 Sirion FEG digital scanning microscope. XRD measurements were carried out using a Bruker, D8 ADVANCE at a scan rate of 2.4° min^{-1}. UV-vis absorption was measured using a OLIS 14 spectrophotometer. AFM images were obtained using a Asylum MFP-3D standard system AFM microscope in a tapping mode. Contact angle measurements were carried out using DSA 100 (KRUSS, Germany).

Solar cell fabrication.

ITO-coated glass substrates were cleaned using sequential ultrasonication in deionized water (DI water), acetone, and isopropanol for 10 min each. A poly(3,4-ethylenedioxythiophene):polystyrene sulfonate (PEDOT:PSS, Clevios™ P VP AI 4083, Heraeus) was spin-cast at 5000 rpm on UV ozone-treated ITO substrates and dried at 140 °C for 10 min. We prepared CPE-K by following synthetic routes in previous reports[104, 105]. For CPE-K layer (thickness: 10 nm), we spin-cast CPE-K solution with concentration of 0.25 wt.% in solvent mixture of DI water and methanol (1:1 vol.%) and film was dried at 80 °C for 10 min. After transferring samples into nitrogen-filled glovebox, precursor solutions of $MAPbI_{3-X}Cl_X$ perovskite were spin-cast at 7000 rpm on top of PEDOT:PSS and CPE-K layer, and baked at 90 °C for 60 min. A PCBM solution with concentration of 1.3 wt.% in chloroform was spin-cast at 3000 rpm on top of perovskite layer. Subsequently, an Al electrode with thickness of 100 nm was deposited on top of the PCBM under vacuum ($<10^{-6}$ Torr) by thermal evaporation. The area of the Al electrode defines the active area of the device as 3.30 mm^2.

Solar cell characterization.

The *J-V* characteristics of the solar cells were measured by a Keithley 2400 Source Measure Unit. The solar cell performance was tested with an Air Mass 1.5 Global (AM 1.5 G) solar simulator with an irradiation intensity of 100 mW cm^{-2}. EQE measurements were obtained using the PV measurement QE system by applying monochromatic light from a xenon lamp under ambient conditions. The monochromatic light intensity was calibrated using a Si photodiode and chopped at 100 Hz. Masks (1.70 mm^2) made of thin black plastic were attached to each cell before measurement of the *J-V* characteristics and the EQE to accurately measure the performance of solar cells. All devices were tested in ambient air after UV-epoxy encapsulation.

5.3 Results and discussion

Optical properties.

We first compared the transmittance of PEDOT:PSS and CPE-K and absorption of perovskite films coated on top of them. **Figure 5.2a** provides the transmittance spectra of PEDOT:PSS and CPE-K films spin-coated on ITO substrates. Bare ITO is also included for comparison. Compared to PEDOT:PSS, CPE-K showed lower transmittance in the range of 350-500 nm and 600-850 nm because of its narrow bandgap (1.4 eV)[105]. Prior to depositing perovskite films on different substrates, we tested whether CPE-K film is washed out by the solvent used for perovskite precursor deposition, namely *N,N*-dimethylformamide (DMF). Although the absorption of the CPE-K film was slightly reduced after spin-coating from DMF **(Figure 5.3)**, the perovskite film can be deposited on CPE-K without complete removal of underlayer, as confirmed by the absorption spectra of $MAPbI_{3-X}Cl_X$ perovskite films spin-coated on PEDOT:PSS and CPE-K (**Figure 5.4**). Perovskite films on CPE-K exhibited slightly higher optical density than perovskite on PEDOT:PSS in the range of 500-850 nm due to absorption of CPE-K **(Inset of Figure 5.3)**. Regardless of substrates, both perovskite films with thickness of 250 ± 20 nm exhibited broad and high light absorption in visible wavelength region.

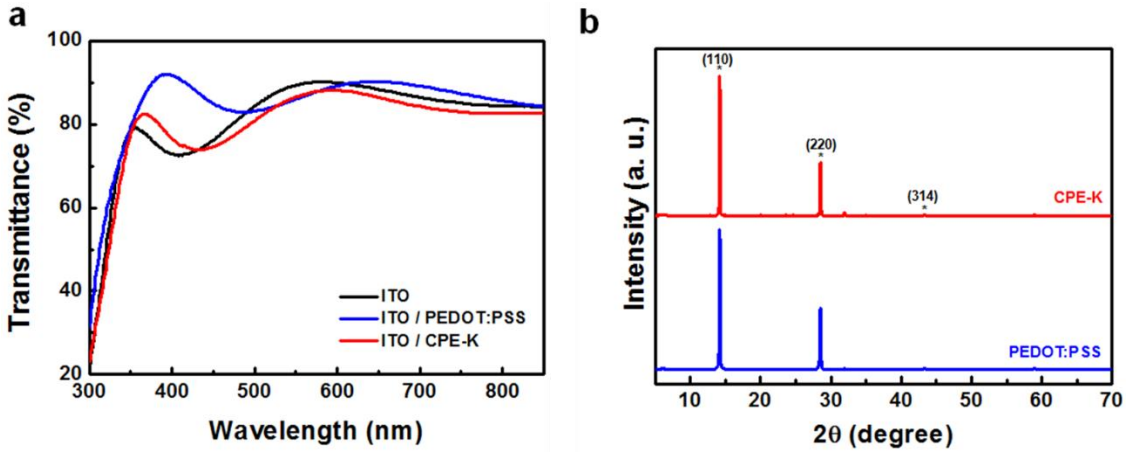

Figure 5. 2. Effect of PEDOT:PSS and CPE-K on optical property and perovskite crystallinity. (a) Comparison of transmittance between PEDOT:PSS and CPE-K on ITO substrate. (b) XRD patterns of perovskite films on PEDOT:PSS and CPE-K layer.

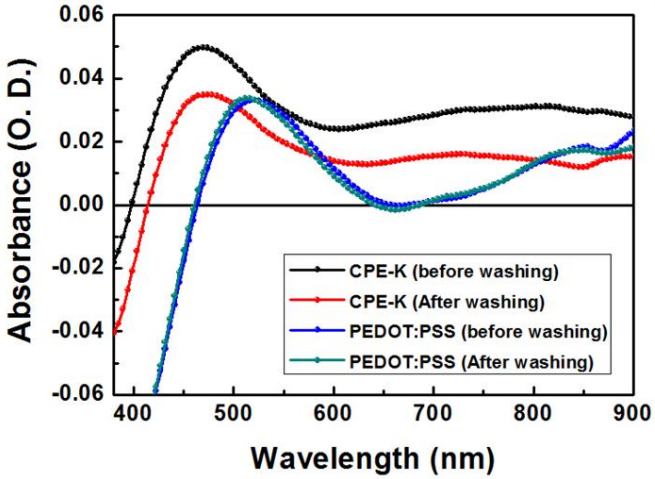

Figure 5. 3. Absorption spectra of PEDOT:PSS and CPE-K films before and after washing with DMF. ITO substrate was used as baseline.

Figure 5.3 shows absorption spectra of PEDOT:PSS and CPE-K before and after washing them with DMF. DMF is a solvent for dissolving two perovskite precursor materials, MAI and $PbCl_2$. Absorption spectrum of PEDOT:PSS was unchanged after washing with DMF, whereas we observed 30% decrease in optical density (OD) of CPE-K. Although washing process with DMF slightly removed CPE-K film, this layer was still existed on ITO substrate without complete washing out. Absorption spectra of perovskite film on PEDOT:PSS and CPE-K were shown in **Figure 5.4**. The film on CPE-K exhibited slightly higher OD than that of the film on PEDOT:PSS owing to higher absorption of CPE-K in visible wavelength region. Absorption difference between perovskite films on PEDOT:PSS and CPE-K (**Inset of Figure 5.4**) was consistent with absorption difference between PEDOT:PSS and CPE-K (**Figure 5.3**).

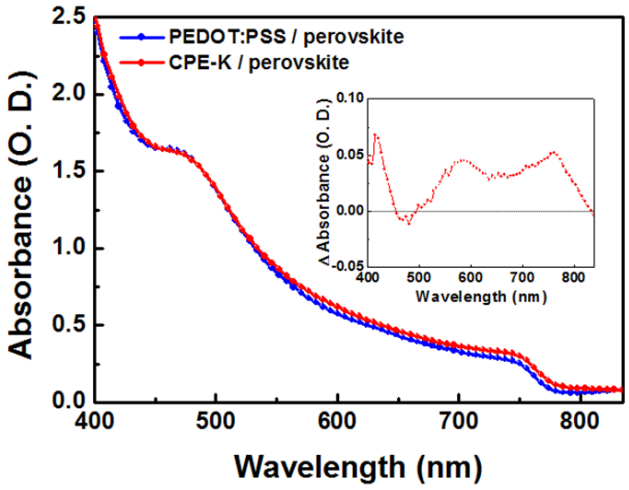

Figure 5. 4. UV-vis absorption spectra of $MAPbI_{3-X}Cl_X$ perovskite films spin-coated on top of PEDOT:PSS and CPE-K. Inset shows absorption difference between them.

Film morphology.

To investigate the influence of PEDOT:PSS and CPE-K on perovskite crystallinity, we performed X-ray diffraction (XRD) measurement. We prepared perovskite films on top of glass substrates coated with PEDOT:PSS and CPE-K. Both films exhibited diffraction peaks at 14.15°, 28.47°, and 43.12°, corresponding to (110), (220), and (314) planes of the tetragonal perovskite phase **(Figure 5.2b)**. These peaks are consistent with XRD results in previous reports on pero-SCs[92, 93, 106]. There were negligible differences in the intensity of diffraction peaks between the two underlayers, implying that both PEDOT:PSS and CPE-K are appropriate substrates for transforming perovskite precursor materials into the desirable perovskite crystal phase.

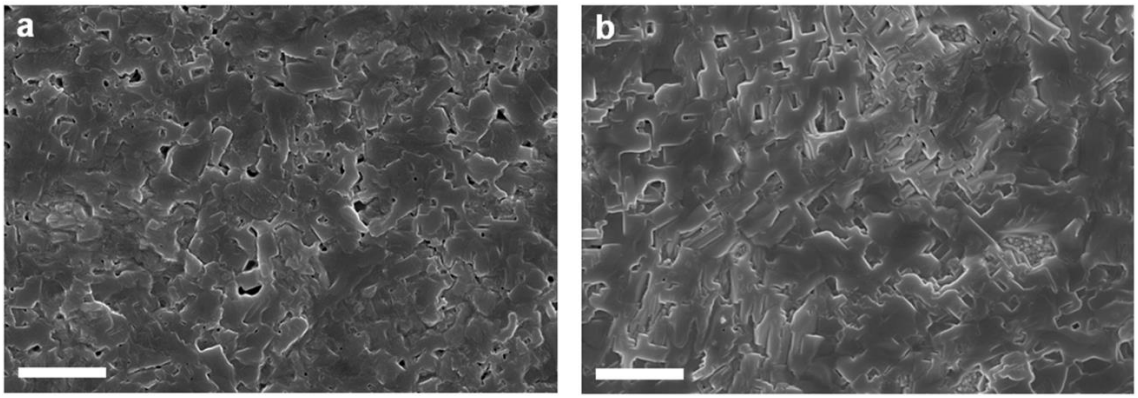

Figure 5. 5. Perovskite film morphology. SEM top-view images of perovskite films spin-coated on top of (a) PEDOT:PSS and (b) CPE-K. Scale bar is 2 μm.

Surface coverage and the morphology of perovskite film on specific substrates are crucial for determining resultant performance of pero-SCs[94, 96]. To compare the morphology of perovskite films on PEDOT:PSS and CPE-K, we utilized scanning electron microscopy (SEM) and atomic force microscopy (AFM). **Figure 5.5** presents the top-view SEM images of perovskite films. Spin coating atop PEDOT:PSS leads to incomplete surface coverage with small voids between crystal boundaries (**Figure 5.5a**), whereas the CPE-K layer provides a uniform perovskite film without voids (**Figure 5.5b**). AFM topography images were consistent with SEM results. Although both PEDOT:PSS and CPE-K layers provided uniform films with root-mean-square (rms) roughness of 1.0 nm (**Figure 5.6**), the perovskite film on CPE-K showed a more even surface with high surface coverage and a roughness of 14.7 nm compared to films deposited on PEDOT:PSS (roughness: 15.6 nm) (**Figure 5.7**).

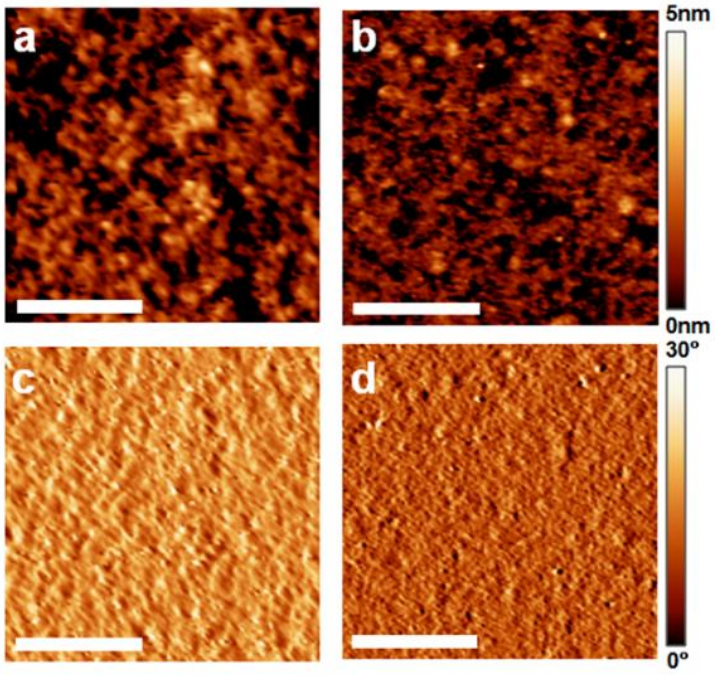

Figure 5. 6. AFM topography (upper row) and phase images (lower row) of PEDOT:PSS (a and c) and CPE-K (b and d), respectively. Scale bar is 1 μm in all AFM images.

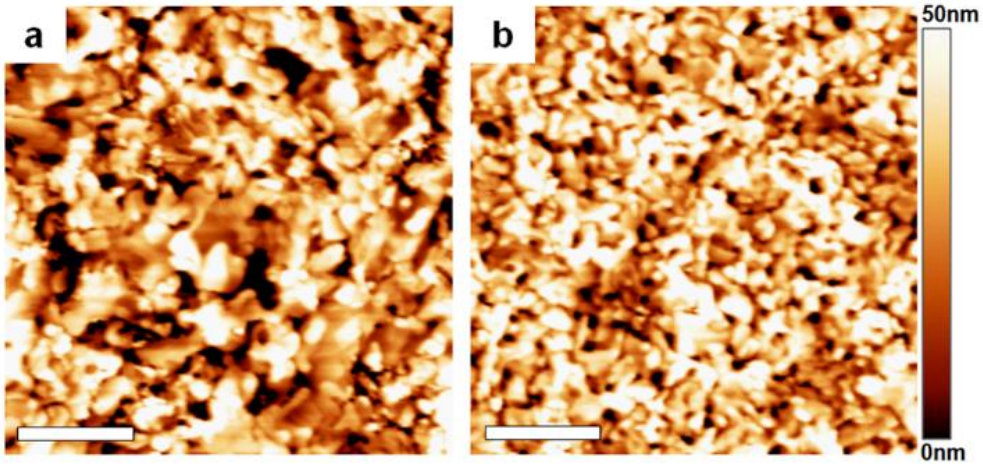

Figure 5. 7. AFM topography images of perovskite films on (a) PEDOT:PSS and (b) CPE-K. Scale bar is 2 μm.

We also studied the surface energy of PEDOT:PSS and CPE-K by performing contact angle measurements. Contact angles of PEDOT:PSS and CPE-K films to DMF were extremely low (< 3°, **Figure 5.8**) and therefore both layers provide excellent wettability with DMF. These results reveal that the physical properties of CPE-K relevant for fabrication of devices, such as wettability and hydrophilicity, are compatible with perovskite solution and enable formation of high coverage uniform perovskite films.

To investigate the influence of different substrates on perovskite film morphology, we first performed AFM measurements for PEDOT:PSS and CPE-K. In spite of small differences in topography and phase images, both films exhibited smooth surface with root-mean-square (rms) roughness of 1.0 nm (**Figure 5.6**). However, different morphology was clearly seen in perovskite films spin-coated on PEDOT:PSS and CPE-K (**Figure 5.7**). Perovskite film on CPE-K was uniform with complete surface coverage and rms roughness of 14.7 nm (**Figure 5.7a**), whereas film on PEDOT:PSS exhibited uneven surface with rms roughness of 15.6 nm and large number of voids between crystal boundaries (**Figure 5.7b**).

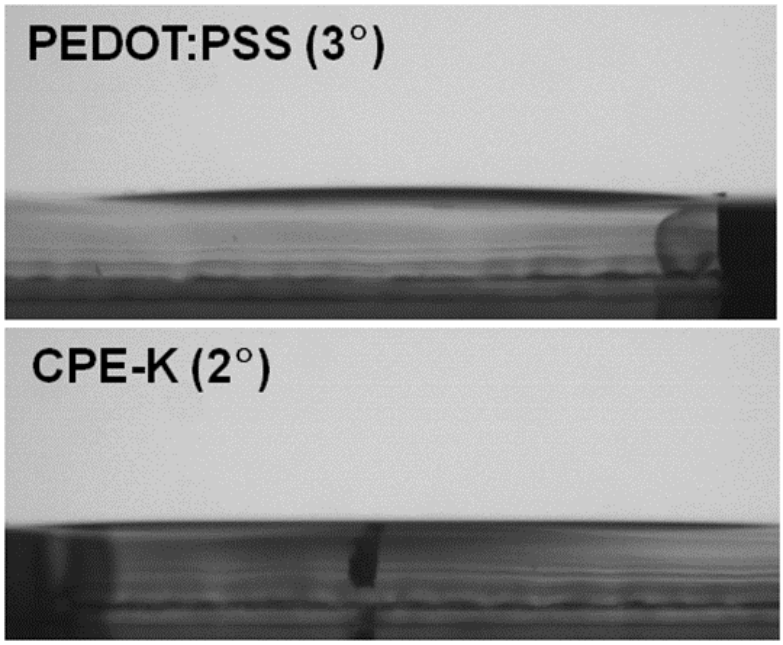

Figure 5. 8. Contact angles of PEDOT:PSS and CPE-K films to DMF.

This implies that CPE-K results in more uniform perovskite film with higher surface coverage than PEDOT:PSS. We also studied surface energy of PEDOT:PSS and CPE-K by performing contact angle measurements. Both film exhibited extremely low contact angles to DMF below 3° (**Figure 5.8**), indicating that super-hydrophilic surfaces of both PEDOT:PSS and CPE-K films are compatible with perovskite precursor solution and thus enable successful formation of perovskite film on them.

Charge transfer dynamics.

To investigate hole selectivity of the perovskite light absorber to ITO anode, we carried out photoluminescence (PL) and time-resolved PL decay measurements. We prepared samples with configuration of glass / (PEDOT:PSS or CPE-K) / perovskite, where thick perovskite film (thickness: 250±20 nm) were used for optimum device performance. CPE-K led to perovskite with more efficient PL quenching than PEDOT:PSS, with quenching efficiencies of 71% and 99% for PEDOT:PSS and CPE-K, respectively **(Figure 5.9a)**. **Figure 5.9b** presents the time-resolved PL decay transients on different substrates. From the calculation of decay values, we obtained average PL decay time (τ_{aver}) of 153 ns for bare glass/perovskite, 91 ns for glass/PEDOT:PSS/perovskite, and 1.41 ns for glass/CPE-K/perovskite. These values are comparable to the PL decay time of $MAPbI_{3-X}Cl_X$ perovskite reported previously[91]. Compared to the perovskite on PEDOT:PSS, CPE-K significantly reduced the PL decay time, implying that holes separated from photo-generated excitons within perovskite layer are efficiently extracted from perovskite to CPE-K. PL quenching and time-resolved PL decay measurements confirm the capability of CPE-K to extract and transport holes from the perovskite layer to the ITO anode. This result is in good agreement with data obtained using CPE-K as the hole extraction layer in polymer solar cells.[15]

For PL decay transients, we prepared three types of samples (glass/perovskite, glass /PEDOT:PSS/perovskite, and glass/CPE-K/perovskite) using perovskite film with optimum thickness (250±20 nm) for best device performance. We excited samples at 405 nm and collected PL decay transients at 770 nm. Perovskite film on CPE-K exhibited faster average PL decay time (1.41 ns) compared to those of films on bare glass and PEDOT:PSS (Bare glass: 153 ns and PEDOT:PSS: 91 ns). These values are in good agreement with PL lifetimes for $MAPbI_{3-X}Cl_X$ perovskite film reported previously[91]. PL decay time measurement reveals that CPE-K has superior capability for hole transport from perovskite light absorber to ITO anode.

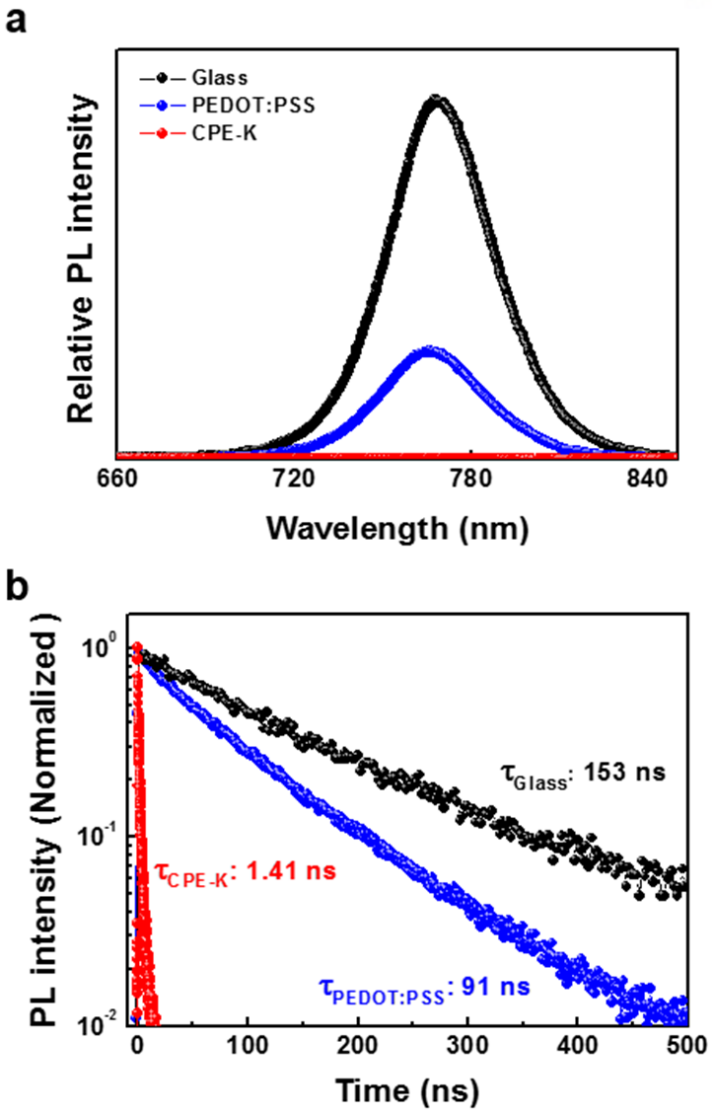

Figure 5. 9. Photoluminescence response of perovskite films on different substrates. (a) Steady-state PL spectra and (b) time-resolved PL decay transients of perovskite films on different substrates. PL decay transients were collected at 770 nm for all films in vacuum after excitation at 405 nm.

Solar cell performance.

To verify the merits of CPE-K in devices, we fabricated ipero-SCs using the simple architecture ITO/PEDOT:PSS or CPE-K/$MAPbI_{3-X}Cl_X$ perovskite/PCBM/Al **(Figure 5.10a)**.The highest occupied molecular orbital (HOMO) and lowest unoccupied molecular orbital (LUMO) levels of CPE-K (HOMO: 4.9 eV and LUMO: 3.5 eV) are well matched with the valence (VB) and conduction band (CB) of the perovskite (VB: 5.4 eV and CB: 3.9 eV), respectively, thereby facilitating hole transport and blocking electron transport from perovskite to the ITO anode (**Figure 5.10b**). PCBM was used as electron transport layer because of the well-known efficient electron transport/hole blocking capability from perovskite to the Al cathode.

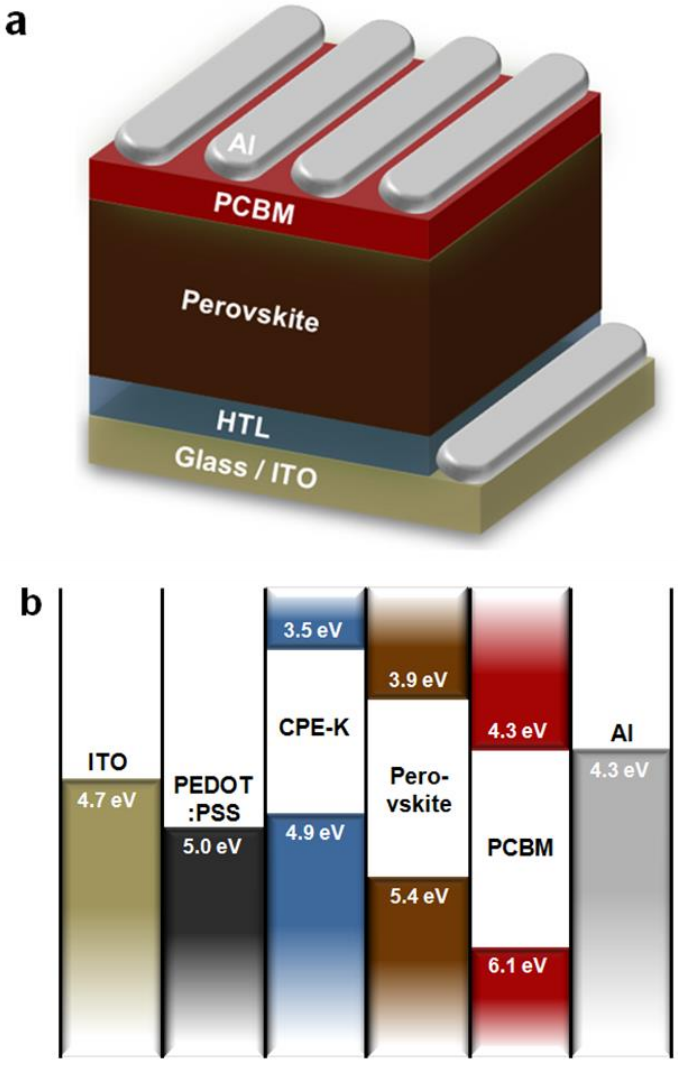

Figure 5. 10. Structure of perovskite solar cells. (a) Device architecture and (b) energy-band diagram of the devices with PEDOT:PSS and CPE-K as the HTL.

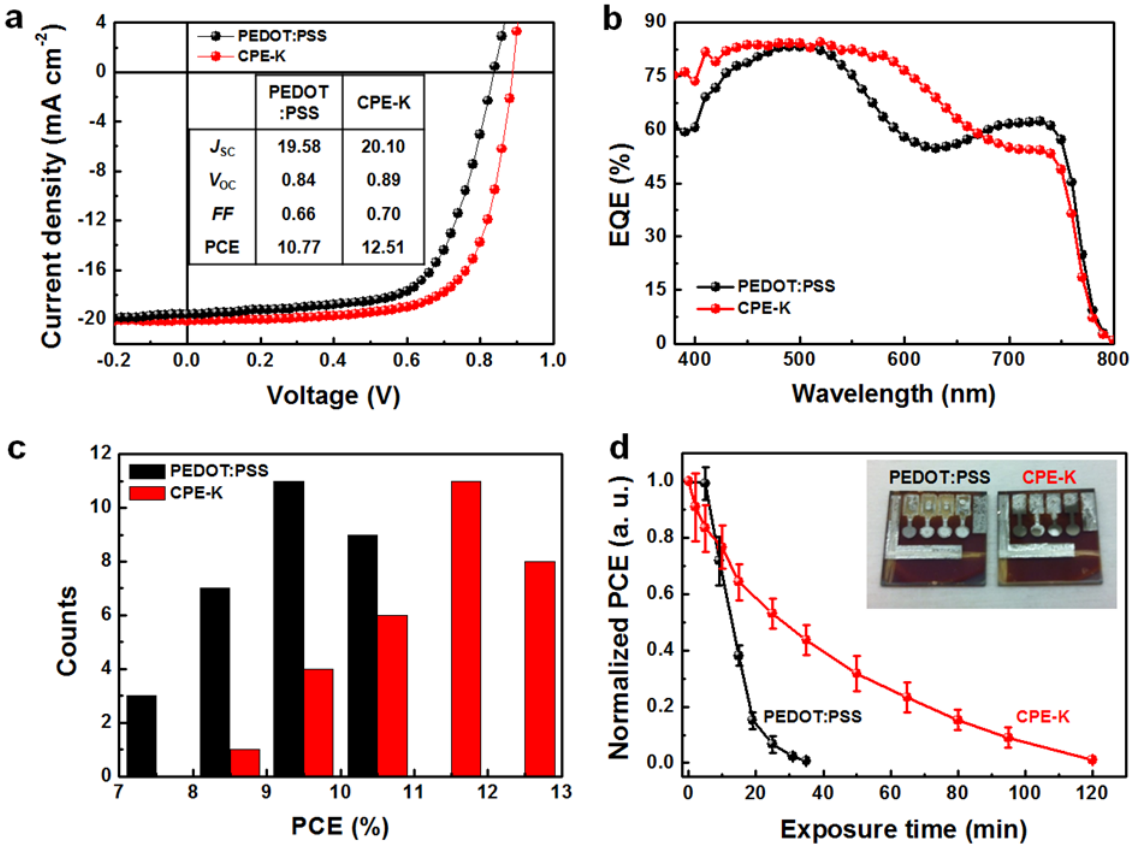

Figure 5. 11. Solar cell performance and stability. (a) Current density-voltage (*J-V*) curves, (b) external quantum efficiency (EQE), (c) efficiency distribution diagram, and (d) device stability of ipero-SCs with PEDOT:PSS and CPE-K in ambient air condition. Inset table of Fig. (a) indicates solar cell parameters, J_{SC} (mA cm^{-2}), V_{OC} (V), *FF*, and PCE (%). Inset images of Fig. (d) exhibit the photos of real devices with PEDOT:PSS and CPE-K after air exposure for 12 h.

Figure 5.11a presents current density-voltage (*J-V*) curves of best ipero-SCs using PEDOT:PSS and CPE-K as the HTL. Devices with PEDOT:PSS exhibited power conversion efficiency (PCE) of 10.77% with short-circuit current density (J_{SC}) of 19.58 mA cm^{-2}, open-circuit voltage (V_{OC}) of 0.84 V, fill factor (*FF*) of 0.66. Replacing PEDOT:PSS with CPE-K led to a significant enhancement in device efficiency. The device with CPE-K yielded a PCE of 12.51% with J_{SC} of 20.10 mA cm^{-2}, V_{OC} of 0.89 V, and *FF* of 0.70. The detailed solar cell parameters are listed in the **inset table in Figure 5.11a**. The high J_{SC} of the devices with PEDOT:PSS and CPE-K is consistent with calculated J_{SC} from external quantum efficiency (EQE) curves (PEDOT:PSS: 18.56 mA cm^{-2} and CPE-K: 19.71 mA cm^{-2}) (**Figure 5.11b**). The margin of error between J_{SC} from *J-V* and EQE measurements was ± 5%. Interestingly, the EQE curve shape of the device with CPE-K differed from that of the device with PEDOT:PSS. Compared to EQE values of the device with PEDOT:PSS, EQE values of the device with CPE-K showed higher EQE values in the range of 400-650 nm and lower EQE values in the

range of 660-800 nm. This phenomenon may be attributed to distinct differences in light absorption and interference effect between PEDOT:PSS and CPE-K. We also tested hysteresis of the devices with PEDOT:PSS and CPE-K. There were slight hysteresis in both devices that may be attributed to interfacial traps induced in HTL or ferroelectric property of perovskite (**Figure 5.12** and **Table 5.3**)[107, 108].

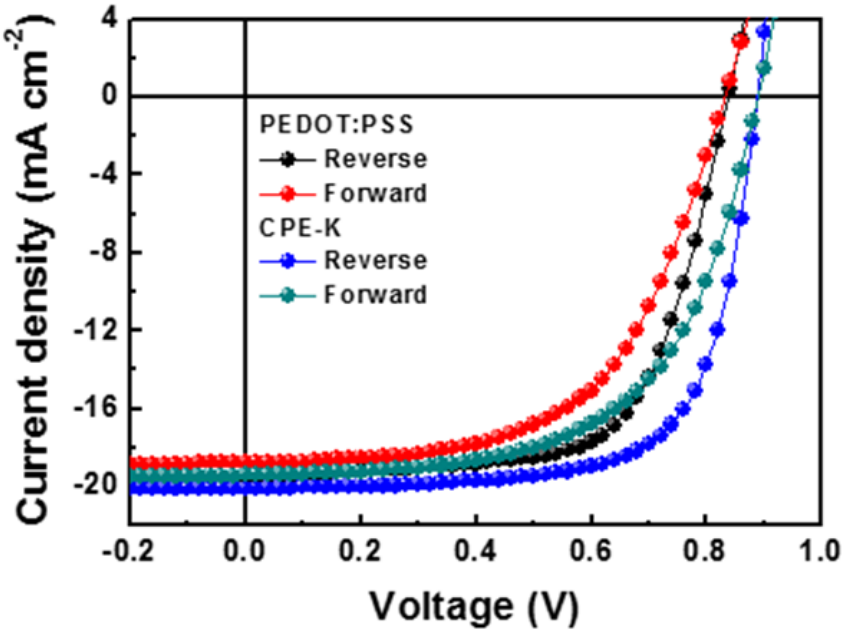

Figure 5. 12. *J-V* curves of pero-SCs with PEDOT:PSS and CPE-K measured by forward and reverse scans with 20 mV voltage steps and 10 ms delay times under AM 1.5G illumination.

To confirm the reproducibility of device performance, we tested 30 devices that were fabricated using PEDOT:PSS and CPE-K with optimum thickness. **Figure 5.11** presents a histogram of device efficiencies for ipero-SCs based on PEDOT:PSS and CPE-K. Average PCEs of the devices with CPE-K (11.20%) were higher than those of the device with PEDOT:PSS (9.37%). Devices with either PEDOT:PSS or CPE-K exhibited similar V_{OC} (0.84-0.90 V) with high reproducibility, whereas J_{SC} and *FF* of the device with CPE-K were mainly higher than those of the device with PEDOT:PSS (**Figure 5.13**). Although we also utilized the simple device structure (ITO/HTL/perovskite/PCBM/Al), the average PCEs of the devices with PEDOT:PSS reported here are comparable to or higher than those of ipero-SCs with similar structure reported in the previous literature (< 8%)[106, 109, 110]. Furthermore, the PCE > 12% of the device with CPE-K is one of the highest values in ipero-SCs with various hole and electron transport materials (NiO_X, TiO_X, and LiF, etc)[97, 100, 101, 111, 112].

Table 5. 3. Device characteristics of ipero-SCs with PEDOT:PSS and CPE-K measured by forward and reverse scans

HTL	Scan direction	J_{SC} (mA cm^{-2})	V_{OC} (V)	FF	PCE (%)
PEDOT:PSS	Reverse	19.58	0.84	0.66	10.77
	Forward	18.79	0.83	0.58	9.04
CPE-K	Reverse	20.10	0.89	0.70	12.51
	Forward	19.41	0.89	0.60	10.30

Figure 5.12 exhibits *J-V* characteristics of ipero-SCs with PEDOT:PSS and CPE-K measured by forward and reverse scan. The detailed device parameters were listed in **Table 5.3**. We performed scans with 20 mV voltage steps and 10ms delay times at 100 mW cm^{-2} irradiation. There was slight hysteresis in both devices which may result from interfacial traps induced in HTL or ferroelectric property of perovskite.

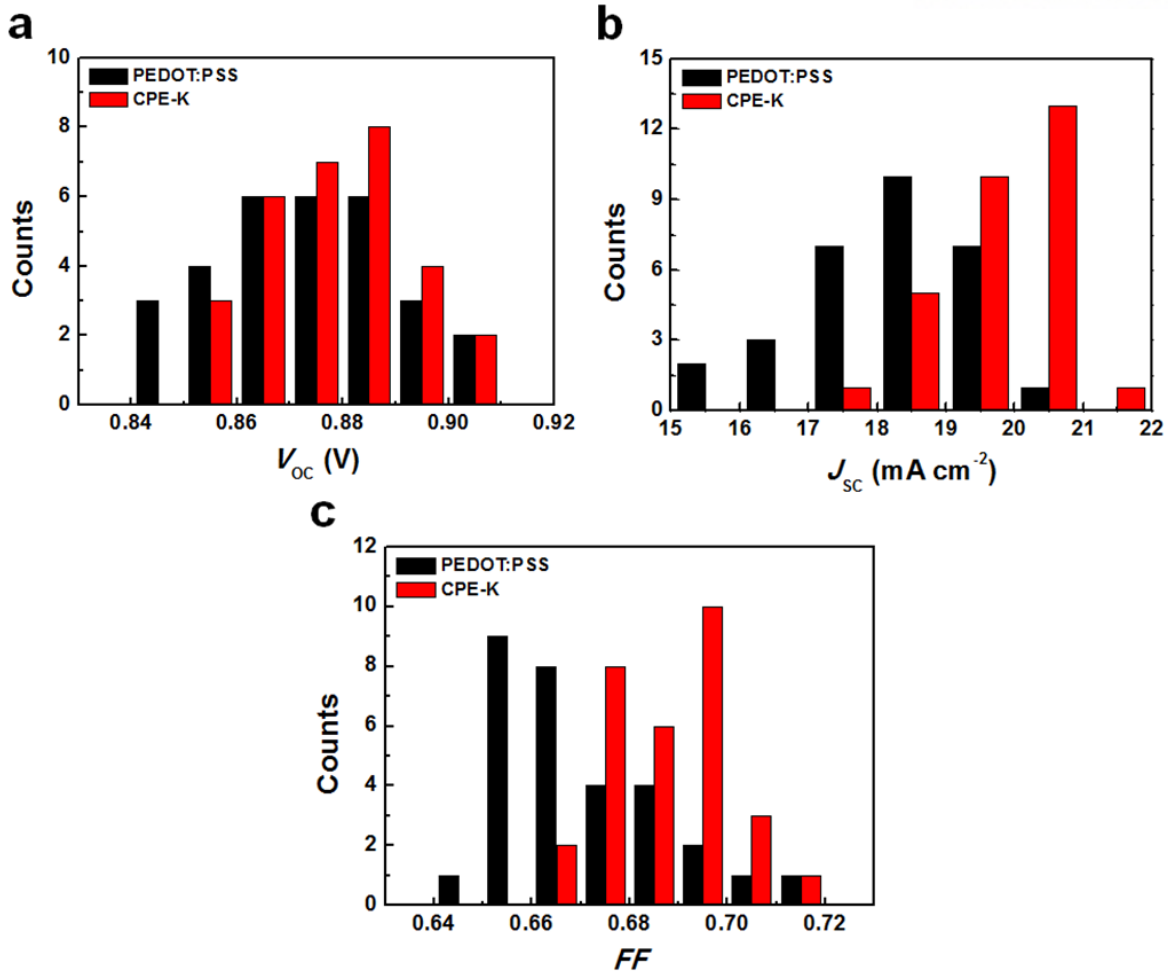

Figure 5. 13. Histograms of device parameters for 30 separate ipero-SCs with PEDOST:PSS and CPE-K. a) J_{SC}, b) V_{OC}, and c) *FF*.

Figure 5.13 shows distribution histograms of three solar cell parameters for 30 separate devices with PEDOT:PSS and CPE-K. Both devices had similar V_{OC} values (0.84-0.91 V) (**Figure 5.13a**), whereas the devices with CPE-K exhibited higher J_{SC} and *FF* than those of the devices with PEDOT:PSS (**Figure 5.13b** and **Figure 5.13c**). As a result, the device with CPE-K yielded higher average PCE (11.20%) than that of the device with PEDOT:PSS (9.37%). This high device efficiency was attributed to improved perovskite film morphology (**Figure 5.5**) and efficient hole transport from perovskite to ITO anode (**Figure 5.9**) by CPE-K HTL.

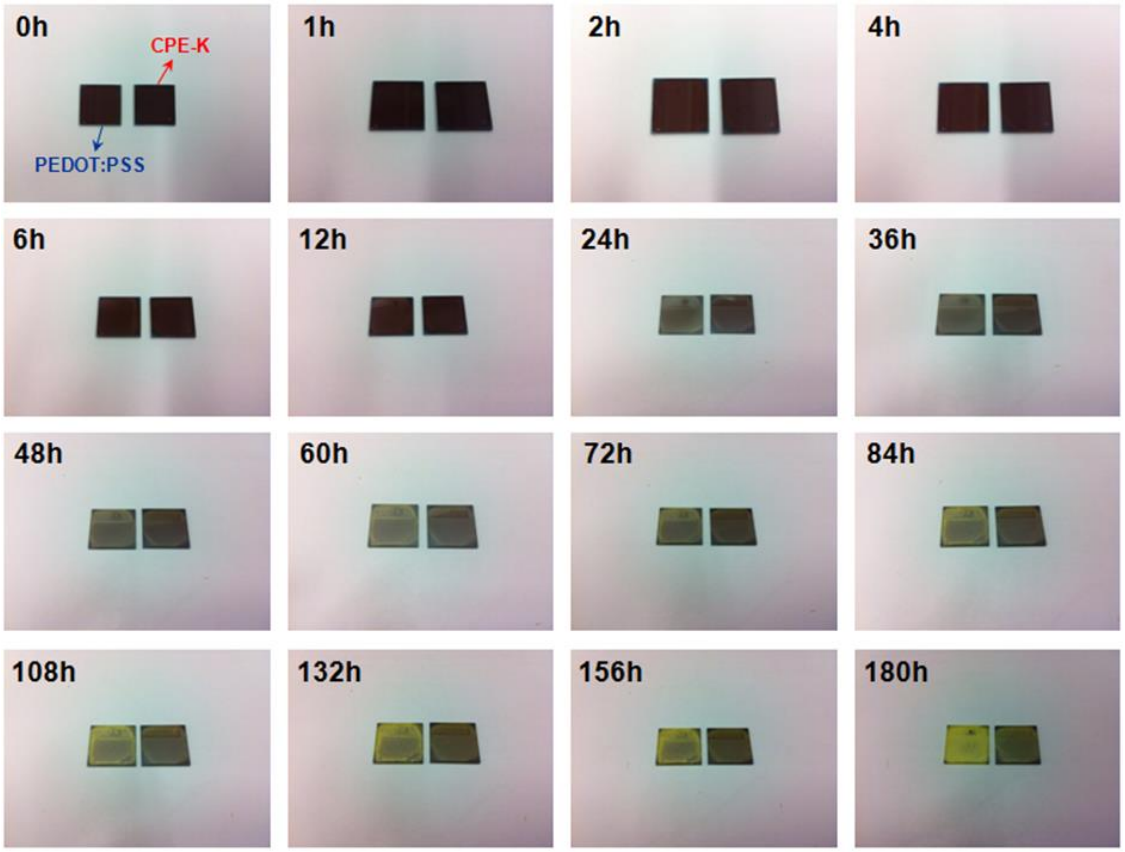

Figure 5. 14. Real images of perovskite films coated on PEDOT:PSS and CPE-K illustrating visible degradation as a function of air exposure time. Average temperature and humidity were 20 ± 3 °C and 40 ± 10% for air stability, respectively.

We also tested the stability of perovskite films and the devices with different HTL in ambient air condition. Average temperature and humidity were 20 ± 3 °C and 40 ± 10% for testing, respectively. We observed degradation in only perovskite film coated on PEDOT:PSS after exposure to air for 12 h (**Figure 5.14**). After 24 h, although the film on CPE-K started to degrade, its degradation rate was slower than that of the film on PEDOT:PSS. After 108 h, the color of the perovskite film on PEDOT:PSS had changed from dark brown to yellow, whereas the film on CPE-K retained the brown color. This suggests that the acidic nature of PEDOT:PSS accelerates the degradation of the perovskite film. **Figure 5.11d** presents normalized PCEs of ipero-SCs with PEDOT:PSS and CPE-K as a function of air exposure time. As expected from the film stability test, the devices with PEDOT:PSS exhibited a more rapid decrease in device efficiency than the devices with CPE-K. After air exposure for 35 min, the reduction rate of PCEs was 99% for the device with PEDOT:PSS and 55% for the device with CPE-K. Long air exposure times, over 12 h, resulted in severe corrosion of Al electrode caused by decomposition of perovskite film in the device with PEDOT:PSS (**Inset of Figure 5.11d**)[113, 114], which further confirms that CPE-K is beneficial for improving device stability.

Figure 5.14 presents visible degradation of perovskite films on PEDOT:PSS and CPE-K as a function of air exposure time. We tested film stability in ambient air condition with average temperature of 20±3° and humidity of 40±10%. We observed the same dark-brown films on both PEDOT:PSS and CPE-K. After 24 h, although visible degradation occurred in the film on CPE-K, degradation rate of film on PEDOT:PSS was much faster than that of film on CPE-K. After 180 h, perovskite film on CPE-K still maintained dark brown color, whereas film on PEDOT:PSS was completely changed to yellow solid, indicating decomposition of perovskite phase into PbI_2 by the presence of water[114]. These results reveal that acidic nature of PEDOT:PSS has bad influence on perovskite film stability and thus is detrimental for device stability in air condition (**Figure 5.11d**).

5.4 Conclusion

In summary, we have successfully employed pH-neutral and low-temperature solution-processable CPE-K as the hole transport layer in inverted-type perovskite solar cells. Excellent wetting of perovskite precursor solution on the CPE-K layer with leads to uniform active layer film with complete surface coverage and superior hole selectivity for facilitating hole transport from perovskite to the ITO anode. As a result, the device with CPE-K exhibits higher device efficiency, over 12%, than that of the device fabricated with widely used PEDOT:PSS. Furthermore, CPE-K improves the device stability in air because of the neutral pH of the underlayer. As an alternative to PEDOT:PSS and p-type metal oxides, CPE-K is a promising hole transport material for efficient perovskite/fullerene planar heterojunction solar cells which can be used on flexible substrates via roll-to-roll processing. This strategy also offers a new approach to design hybrid tandem solar cells employing CPE-K as intermediate layer, and combining organometallic perovskites and small bandgap organic semiconductors as the active layer.

CHAPTER 6. Perovskite-Based Light-Emitting Solar Cells

6.1 Research background

In a short period of time, methyl ammonium (MA) lead halide perovskite semiconductors have proven themselves as incredibly effective solar cell (SC) materials[115-118] as their power conversion efficiencies (PCEs) have surpassed every other emerging solar technology and matched the performance of well-established technologies like polycrystalline silicon, CdTe and Cu(InGa)Se_2 devices.[119] Concurrently, interest in perovskite-based light emitting diodes (LEDs) has grown in recent months[120-122] and the performance of perovskite LEDs has also progressed rapidly. Given the similar architectures of perovskite LED and SCs, one interesting possibility is perovskite light emitting solar cells (LESCs), or devices which reversibly transduce optical energy into electrical energy or electrical energy into optical energy.

Although perovskite SCs and LEDs share similarities, they perform fundamentally different functions; the electronic band structures of SCs are designed to make it energetically favorable for electrons and holes to separate and migrate out of the active perovskite layer and towards the electrodes,[123, 124] whereas LEDs are designed to make it energetically favorable for electrons and holes to migrate towards the active perovskite layer where they combine to emit light. An LESC must be able to perform both functions and act as a reversible opto-electronic transducer; that is absorb light in an active layer and extract photo-generated electron-hole pairs under illumination to generate power, while also being able to inject electron-hole pairs and promote radiative charge recombination in the same active layer when connected to an external power supply. These concepts are illustrated schematically in **Figure 6.1a**.

The low exciton binding energies and high charge carrier mobilities of perovskite materials allow them to convert electron-hole pairs into photons and vice-versa with minimal energy loss, while at the same time efficiently transporting electrical charges into or out of the active layer. The solution-processability and ability to tune bandgaps throughout the visible spectrum makes perovskite materials uniquely suited for this application and we will refer to this type of perovskite based LESC as a “peroptronic” device.

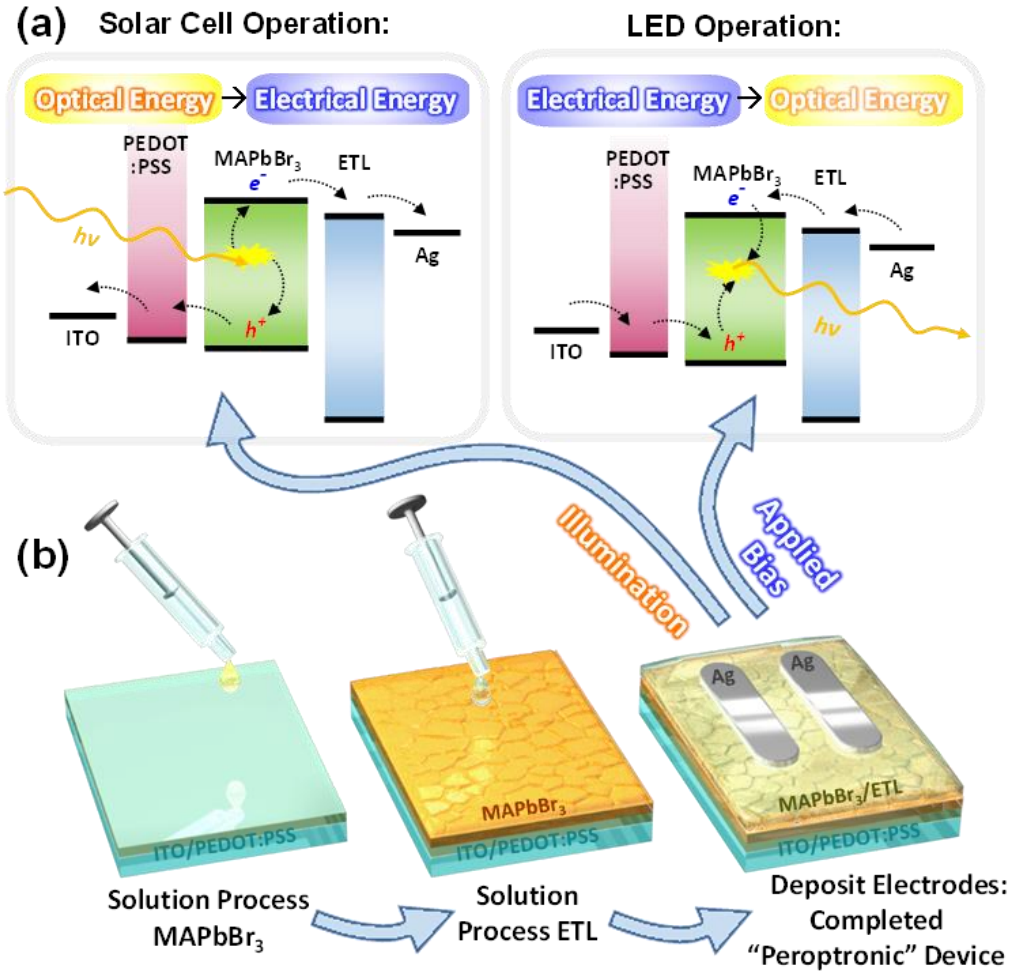

Figure 6. 1. Schematic diagrams. (a) Flow of charge carriers in a peroptronic device under SC and LED operation and (b) fabrication of $MAPbBr_3$ based LESCs**.**

Recent reports have demonstrated that perovskite solar cells based on $CsPbI_3$ or mixed MA / formamidinium lead halides are able to exhibit excellent solar cell performance as well as efficient light emission at near-infrared wavelengths.[125, 126] For instance, Bi *et al* reported electroluminescence quantum efficiencies of up to 0.5% for infrared LESCs with a band gap of 1.6 eV and photovoltaic power conversion efficiency (PCE) of 19.9%, but did not report detailed LED characteristics.[125] Swarnkar *et al* reported $CsPbI_3$ quantum dot LESCs with PCE of 10.8% and electroluminescence near 700 nm, but also did not include detailed LED characteristics.[126] Despite these interesting results with infrared emitting solar cells, peroptronic devices which emit light in the visible region and function efficiently as solar cells, to the best of our knowledge, have not yet been reported.

While it is academically interesting to pursue perovskite devices which are able to reversibly convert energy between light and electrical potential, such devices are interesting from practical points of view as well. For instance, solar lamps, which use SCs to harvest solar energy during the day and LEDs to emit light at night have found wide use in consumer and public lighting applications and are envisioned as replacements for oil lamps in developing countries which lack electrical infrastructure, if they can be produced inexpensively.[127] Integrating an LESC with a rechargeable battery would allow it to function as a solar lamp with reduced the complexity and cost compared to existing solar lamps. Additionally, LESCs have the potential to greatly improve performance in applications which rely on the weak photovoltaic effect of LEDs, such as fiber optic communications and atmospheric sensors.[128, 129]

6.2 Experimental details

Materials.

Lead bromide ($PbBr_2$) was purchased from Alfa Aesar, anhydrous N-methyl-2-pyrrolidone (NMP), anhydrous *N*,*N*-dimethylformamide (DMF), anhydrous isopropanol (IPA) and anhydrous Dimethyl sulfoxide (DMSO) were purchased from Sigma-Aldrich. All materials were used without purification.

Methylammonium bromide (MABr) was prepared by mixing 30 ml CH_3NH_2 (40 wt% in water, Sigma Aldrich) and 30 ml Hydrobromic acid (48 wt% aqueous solution, Sigma Aldrich) in a 250 mL, three-neck flask at 0 ℃ for 2 hr with stirring. The precipitate was recovered by evaporation under vacuum at 60 ℃ for 1 hr. To purify, the MABr precursor was re-dissolved in ethanol and recrystallized from diethyl either. Finally, the MABr product was dried at 60 ℃ under vacuum oven for 24 hr.

PEI BIm_4 was prepared as follows: The conjugate acid of BIm_4 ($HBIm_4$) was first prepared in an adaptation of a previously reported method.[130] Briefly, 250 mg $NaBIm_4$ was dissolved in 20 mL of deionized water. 825 μL of 1M HCl was added to this solution via micropipette and the mixture was shaken. A fine white material ($HBIm_4$) precipitated which was collected by centrifuging. The solid was washed three times with 5 mL water, twice with methanol (3 mL) and dried under vacuum to yield 141 mg of $HBIm_4$. To 100 mg of $HBIm_4$, 1.23 mL of a 50 mg/mL solution of PEI in IPA was added and the mixture was allowed to stir vigorously for at least 2 hr. Some $HBIm_4$ remained un-dissolved. The mixture was filtered through a 0.45 μm PTFE syringe filter to yield a clear solution which was diluted with 25 volumes of IPA before being used for device fabrication. Integration of a ^{1}HNMR spectrum indicated approximately 1 BIm_4 anion for every 6 ethylenimine repeat units. ^{1}HNMR (400 MHz, D_2O) δ 7.33 (1H, s), 7.06 (1H, s), 6.88 (1H, s), 2.5-2.8 (8.3H, br).

General Methods.

Scanning electron microscope measurements (SEM) were performed using an S-4800 Hitachi high-Technology microscope. SEM samples were prepared by coating perovskite presursor solutions onto glass substrates by spin-coating at 3000 rpm. For X-ray diffraction (XRD) measurements, perovskite films were coated on PEDOT:P SS-coated glass substrates and diffractorams were collected using a Bruker D8 ADVANCE diffractometer at a scan rate of 2.4° min-1. UV-vis absorption was measured using a Varian Cary 5000 spectrophotometer

Perovskite Films.

One-step method: To prepare $MAPbBr_3$ precursor solutions for the one-step method, MABr and $PbBr_2$ were dissolved at a 1.05:1 molar ratio in a mixture of DMF and DMSO solvents (7:3 [v/v]) with a concentration of 37.5 wt%. This solution was stirred with a magnetic stir-bar at 60 °C for 2 hr prior to use.

Two-step method: To prepare $PbBr_2$ solutions for the two-step method, $PbBr_2$ was dissolved in a mixture of DMF and NMP (9:1 [v/v]) at a concentration of 367 mg/ml. An MABr solution was prepared by dissolving MABr in IPA with a concentration of 20 mg/ml. Both solutions were stirred with a magnetic stir-bar at room temperature for 2 hr prior to use.

Device fabrication.

ITO-coated glass substrates were cleaned by ultra-sonication in deionized water, acetone and isopropanol for 10 min each. A poly(3,4-ethylenedioxythiophene):polystyrene sulfonic acid (PEDOT:PSS) layer was deposited on cleaned ITO substrates by spin-coating at 3000 rpm for 40 s, followed by annealing at 150 °C for 15 min. On top of the PEDOT:PSS (AI 4083) layer, the perovskite ($MAPbBr_3$) precursor solution (one-step method) was spin-cast at 500 rpm and 3000rpm for 5 s and 50 s, respectively. During the second spin-coating step, the film was treated by dropping chlorobenzene onto it after 30 s of spinning. The two step method was carried out as follows: a $PbBr_2$ solution was first spin cast at 5000 rpm for 30 s. Directly on top of $PbBr_2$ layer, an MABr solution was dropped and left to stand for 20 s, then the substrate was spun at 3000 rpm for 30 s. Various electron transport layers were deposited by spin-coating at 2500 rpm for 40 s as described below. Finally, devices were completed by thermal evaporation under high vacuum ($<10^{-6}$ Torr) using Ag electrodes with a thickness of 120 nm.

Electron Transport Layer Deposition.

On top of the perovskite layer, one of the following ETLs solutions was spin cast: A 50 mg/ml solution of ZnO NPs in chloroform or 10 mg/ml TPBI solution in chlorobenzene or 2mg/ml PEI or PEI BIm_4 solutions in isopropanol were spin-cast at 2500 rpm for 40s. It should be noted that ZnO is known to react with $MAPbI_3$ upon thermal annealing,[131] however, we found that the ZnO NP ETL did not noticeably affect the stability of devices if it was deposited on top of the $MAPbBr_3$ layer without thermal annealing.

Solar Cell and LED Characterization.

The current density-voltage (*J-V*) characteristics of the solar cells were measured using a Keithley 2635A Source Measure Unit. Solar cell performance was carried out under illumination by an Air Mass 1.5 Global (AM 1.5 G) solar simulator with an irradiation intensity of 100 mW cm^{-2}. Apertures (13.0 mm^2) made of thin metal were attached to each cell before measurement for *J-V* characteristics. External quantum efficiency (EQE) measurements were obtained with a PV measurements QE system under ambient conditions, with monochromated light from a xenon arc lamp. The monochromatic light intensity was calibrated with a Si photodiode and chopped at 100 Hz. LED measurments were performed using a Keithley 2400 source measurement unit and a Konica Minolta spectroradiometer (CS-2000, Minolta Co.).

6.3 Results and discussion

Perovskite Materials and Processing

To design an efficient peroptronic device, we chose $MAPbBr_3$ as an active layer material, as it possesses an appropriate band gap (E_g, 2.18 eV) for this application. $MAPbBr_3$ absorbs light strongly below 540 nm, which allows it to generate significant photocurrent[132, 133] and exhibits fluorescence in the middle of the visible spectrum (at ~520 – 560 nm), which is desirable for LED devices.[134]

In general, perovskite SCs tend to exhibit optimal performance when the crystal grain size of the active layer is large, whereas perovskite LEDs tend to perform better with smaller grain sizes and smoother films.[135] Thus, the active layer morphology of peroptronic devices must be designed to allow charge separation and charge recombination to both occur with minimal losses. We observed that small grain sizes inevitably led to poor SC performance, whereas intermediate to large grain sizes (greater than ~ 100 nm) could produce reasonably good LED performance with the use of suitable buffer layers. Two processing approaches were found to yield $MAPbBr_3$ films with suitable morphologies including a single step[94] and two-step[136] approach. A one-step, solvent-engineering method involved spin-coating an $MAPbBr_3$ film from a dimethylformamide (DMF) and dimethylsulfoxide solvent mixture, followed by dropping a non-solvent (chlorobenzene) on the drying film while as it was still spinning. Additionally, a two-step, layer-by-layer method was employed. In the two-step method, a $PbBr_2$ film was first spin-cast from a solution in DMF, followed by conversion to $MAPbBr_3$ by spin-coating a solution of MABr in isopropanol (IPA). A schematic illustration of the device fabrication process is shown in **Figure 6.1b**

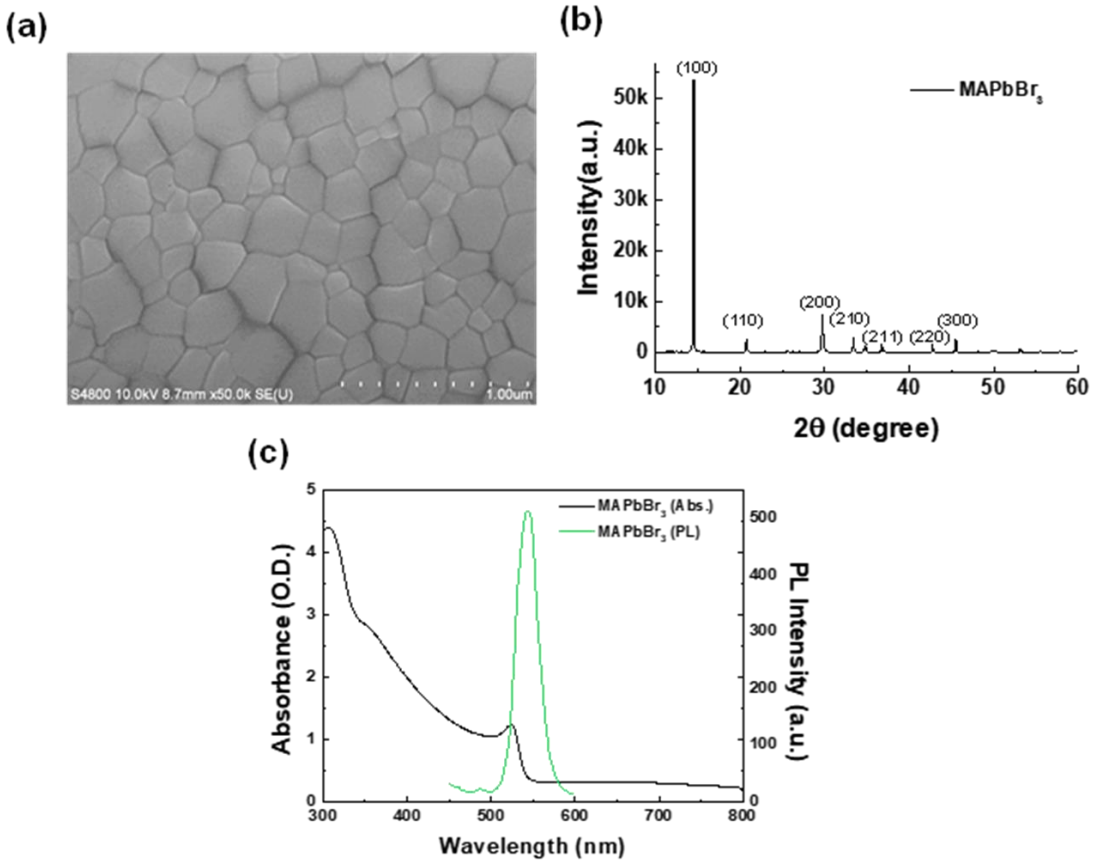

Figure 6. 2. Material properties. (a) SEM image of solution-processed $MAPbBr_3$ film. (b) X-ray diffractogram of MAPbBr3 layer. (c) Absorption and photoluminescence of $MAPbBr_3$ layer.

Both techniques yielded functioning LESC devices, however, we observed superior performance in the one-step processed films and we will focus on data for this method. A scanning electron microscope (SEM) image of a $MAPbBr_3$ films processed by the one-step method is shown in **Figure 6.2a**. Characteristics of $MAPbBr_3$ films processed by the two-step method are included in **Figure 6.3**. The films exhibit average grain sizes of about 250 nm and 330 nm, for one-step and two-step processing, respectively. The one-step method yields grains which are somewhat smaller, but more closely packed than the two-step method, while the two-step method showed larger cracks between crystal grains. X-ray diffraction (XRD) patterns of the one-step method films (**Figure 6.2b**) exhibit peaks at 14.48˚, 29.69˚, and 45.51˚ that can be assigned to (100), (200), (300) diffraction planes of the Pm3m cubic structure of $MAPbBr_3$.[137] There are no differences in the position of XRD peaks for the two processing methods, however, with the two-step method, we observed very strong diffraction peaks corresponding to the (100), (200), (300) planes. The higher intensity, narrower peak width, and predominance of (100), (200), (300) peaks observed in the two-step method film can be attributed to larger grain size[138] and anisotropic growth of the 100 crystal plane relative to the substrate

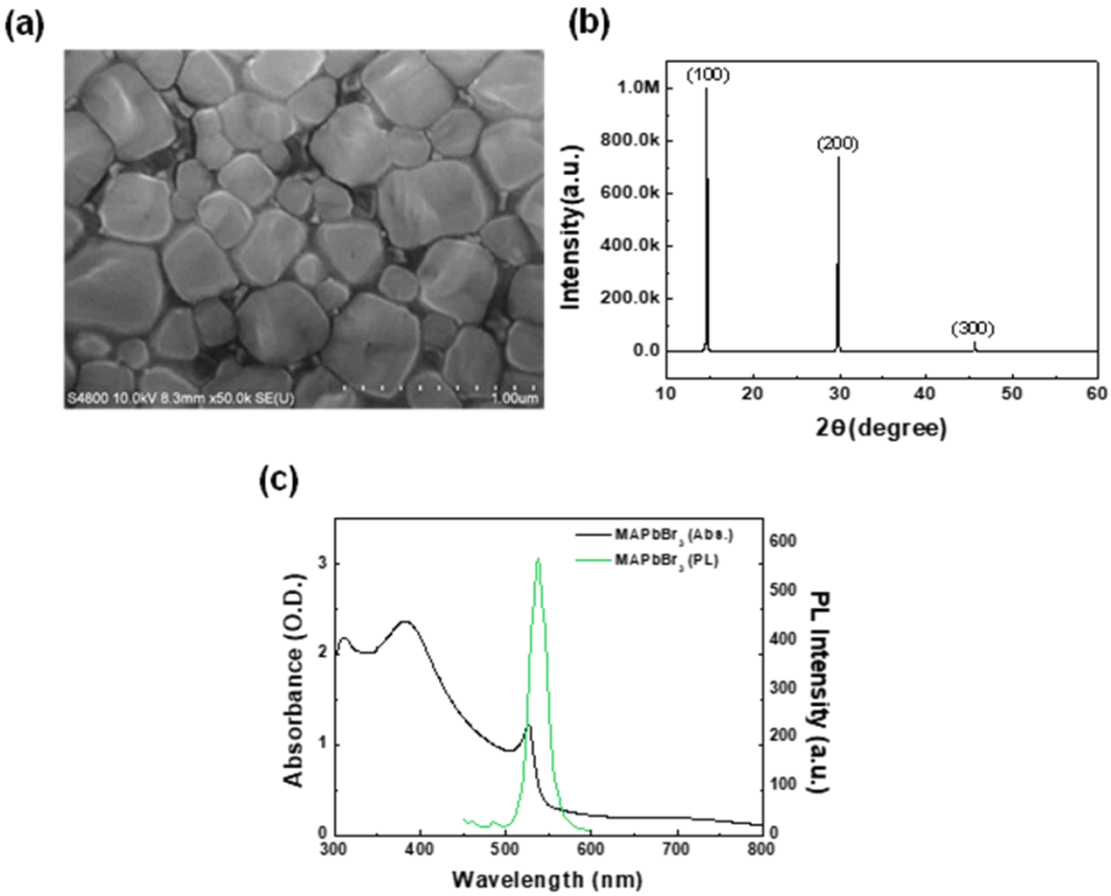

Figure 6. 3. Characteristics of two-step, solution-processed $MAPbBr_3$ films. (a) SEM image. (b) X-ray diffractogram. (c) Absorption and photoluminescence spectra.

The absorption and photoluminescence (PL) spectra of one-step $MAPbBr_3$ films are shown in **Figure 6.2c**. Films processed by one-step and two-step procedures exhibit local absorption maxima 524 and 526 nm, respectively, with fluorescence maxima at 543 and 537 nm, respectively. The Stoke's shift and FWHM of the two-step film (11 nm and 20 nm, respectively) are noticeably smaller than the one-step film (19 nm and 29 nm, respectively). The Stoke's shift and FWHM for one-step films are typical for previously reported $MAPbBr_3$ films,[139] however, the two-step film shows a small shift and narrower emission linewidth than usual. The linewidth of emission from $MAPbBr_3$ films has been correlated to Frölich coupling between charge carriers and longitudinal optical phonons.[140] It is unlikely that the differences in crystal growth during one-step and two-step processing methods would affect the Frölich coupling constant, therefore, we speculate that differences in the film thickness or dielectric properties may have caused small variations in the emission spectra via optical cavity effects.[141] In any case, both processing methods yielded $MAPbBr_3$ films with satisfactory material properties and were used in peroptronic devices.

Electronic Band Structure

Successful perovskite based SCs and LEDs both utilize sandwich architectures in which perovskite active layers are nested between charge-selective carrier-transport layers. Of critical importance in the design of LESC devices is choosing carrier transport layers which do not impose significant energy barriers to either the injection of charge carriers or the extraction of charge carriers. Furthermore, the carrier transport layers must possess a high conductivity, to minimize the series resistance in SC operation, while at the same time efficiently blocking carriers of the opposite polarity, in order to ensure that charge carriers are trapped, and forced to radiatively recombine within the perovskite layer under forward bias. Selecting appropriate charge carrier transport layers which fulfill these functions was the most critical design criterion to realizing effective peroptronic devices.

Poly(3,4-ethylenedioxythiophene):poly(4-styrenesulfonate) (PEDOT:PSS) has been demonstrated as a hole transporting layer (HTL) which effectively forms Ohmic, p-type contacts in both LED and SC devices while blocking electron back-diffusion, thus we employed PEDOT:PSS coated indium tin oxide (ITO) substrates as the anodes in our devices. Choosing an appropriate electron transporting layer (ETL) was somewhat more challenging. In LED devices, low conductivity ETLS such as 1,3,5-tris(N-phenylbenzimidazol-2-yl) benzene (TPBI),[142] poly(9,9-di-n-octylfluorenyl-2,7-diyl)[143] and spirobifluorene[144] tend to be favored. These materials possess high-lying lowest unoccupied molecular orbital (LUMO) energy bands, which trap electrons within the active layer, forcing carrier recombination and consequently luminescence from within the active layer. In the context of SCs however, such high-lying LUMO energy bands are undesirable as they create an energetic barrier (Φ_{ext}) to the extraction of electrons. In contrast, SCs tend to favor high conductivity ETLs which allow electrons to be rapidly extracted from the active layer, however may introduce an energetic barrier to electron injection (Φ_{inj}) from the ETL into the conduction band (CB) of the active layer, and lead to non-radiative recombination in LED devices. Additionally, some popular n-type acceptor materials such as fullerenes or perylenetetracarboxylic acid derivatives which work well in SCs are known to quench electroluminescence in LED devices.[145] In this study, we chose to focus on ETLs including ZnO, a wide E_g inorganic semiconductor with high electron mobility, which has been effectively used in both LEDs[143] and SCs[146] as well as polyethyleneimine (PEI), which has been shown to be an outstanding n-doping / interfacial dipole material in both LEDs and SCs.[80]

One additional ETL that we found to work exceptionally well, as will be described later, was a polyelectrolyte based on a partially protonated PEI backbone with tetraimadazolylborate anions (PEI BIm_4). We designed this ETL with inspiration from conventional perovskite SCs which employ ionically doped HTLs[147] and considered that an ionically doped ETL might function well with a perovskite active layer. We also drew from past experience in organic electronics, in which it has been observed repeatedly that conjugated polyelectrolytes and oligoelectrolytes which incorporate the BIm_4

anion give rise to large interfacial dipoles[148] and outstanding LED, SC and FET performance.[149, 150] PEI BIm_4 was synthesized by preparing the conjugate acid of the BIm_4 anion[130] and neutralizing it with a basic solution of PEI in IPA. This scheme yields a polyelectrolyte in which approximately one out of every 6 ethylenimine repeat units was protonated and charge-compensated by a BIm_4 anion. Notably, IPA is known as a solvent which is compatible with perovskite films[136] and we observed that IPA solutions of PEI BIm_4 could be spin-cast on top of perovskite films without adversely affecting the underlying $MAPbBr_3$ layer.

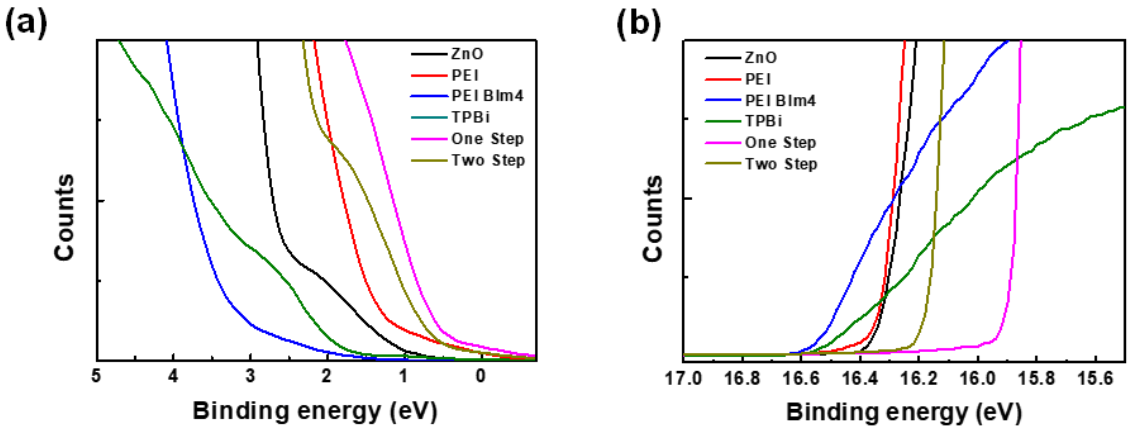

Figure 6. 4. UPS spectra. (a) Close-up of Fermi edge region of different films. (b) Close-up of secondary edge region of different films. For these measurements, thin ETL layers were deposited onto one-step $MAPbBr_3$ layers.

Table 6. 1. Energy levels of different films deposited on $MAPbBr_3$ derived from UPS and UV-vis data.

Structure	***WF*** **(eV)**	***E_{VB}*** ***(eV)***	***E_{CB}*** ***(eV)***	***E_g*** **(eV)**
$MAPbBr_3$	5.31	5.74	3.46	2.28
ZnO	4.88	7.53	4.18	3.35
PEI	4.86	7.17	1.13	6.04
PEI Blm_4	4.64	7.31	2.14	5.17
TPBI	4.66	6.53	3.08	3.45

In order to understand the energy band structure of our devices, ultraviolet photoelectron spectroscopy (UPS) experiments were carried out (**Figure 6.4**). The valence band (VB) energies (E_{VB}) of inorganic materials or highest occupied molecular orbital (HOMO) band energies (E_{HOMO}) of organic materials were derived from the Fermi edge of each material relative to a gold reference. Work functions (φ) were derived from the secondary edge (E_{SE}) via the equation $\varphi = h\nu - E_{SE}$, where $h\nu$ is the energy of the UV light source (21.2 eV). Conduction band (CB) energies (E_{CB}) of inorganic materials or LUMO band energies (E_{LUMO}) of organic materials were derived from the E_{VB} or E_{HOMO} energies, respectively, by subtracting their E_gs taken from UV-vis absorption data. These values are summarized in **Table 6.1** and were used to construct energy band diagrams (**Figure 6.5**).

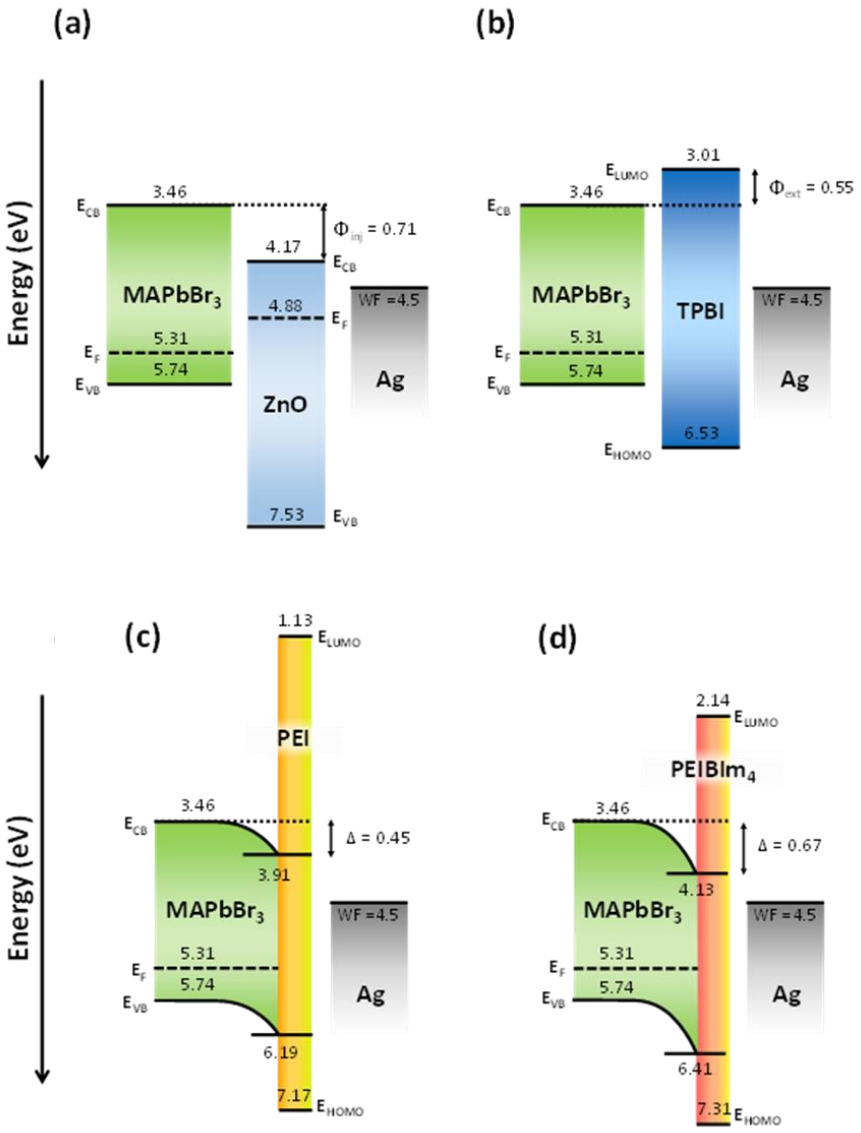

Figure 6. 5. Energy band diagrams for devices with the architecture ITO/PEDOT:PSS/$MAPbBr_3$/ ETL/Ag. (a) Using ZnO as an ETL. (b) Using TPBI as an ETL. (c) Using PEI as an ETL. (d) Using PEI BIm_4 as an ETL.

Devices using a ZnO ETL have an offset between the E_{CB} of the $MAPbBr_3$ and the E_{CB} of ZnO (**Figure 6.5a**). After electrons are excited to the conduction band of $MAPbBr_3$ by photon absorption, this offset makes electron transfer from the E_{CB} of $MAPbBr_3$ to ZnO energetically favorable, however, it also imposes an energy barrier (Φ_{inj}) of 0.71 eV to electron injection, which is expected to hinder LED operation. Devices using a TPBI ETL (**Figure 6.5b**) have an opposite offset between the E_{CB} of the $MAPbBr_3$ and the LUMO of TPBI; this allows facile injection of electrons into the CB of $MAPbBr_3$ under forward bias, but imposes an energetic barrier for extraction of electrons (Φ_{ext}) of 0.55 eV from the CB of $MAPbBr_3$ in SC operation.

PEI and PEI BIm_4 films deposited on $MAPbBr_3$ (**Figure 6.5c, 6.5d**) both caused a strong shift in the secondary edge of their UPS spectra. In the context of inorganic semiconductors, this would normally be interpreted as a change in the workfunction (WF) or Fermi energy (E_F) of the material that is conventionally described by bending of the VB and CB bands. In the context of organic semiconductors, this would be interpreted as a shift in the vacuum energy, or formation of an interfacial dipole. We have chosen to interpret this as a change in the E_F and band bending, although either interpretation would be consistent with the observed experimental results. The WF of pristine $MAPbBr_3$ was found to be 5.31 eV, and decreased to 4.86 eV after application of a PEI ETL, and decreased further to 4.64 eV after application of a PEI BIm_4 ETL, indicating that both ETLs caused n-doping relative to the pristine film, with corresponding band offsets (Δ) of 0.45 eV with PEI or 0.67 eV with PEI BIm_4

Solar Cell and LED Characterization

Peroptronic devices were prepared with the architecture ITO/PEDOT:PSS/ $MAPbBr_3$/ETL/Ag, and characterized as both SCs and LEDs. The current voltage and electroluminescence characteristics for devices based on one-step processed active layers are summarized in **Table 6.2** while the relevant data are plotted in **Figure 6.6**. Although the two-step processed $MAPbBr_3$ active layers appeared to have superior crystallinity, they showed slightly inferior performance, likely due to cracks in the active layer.

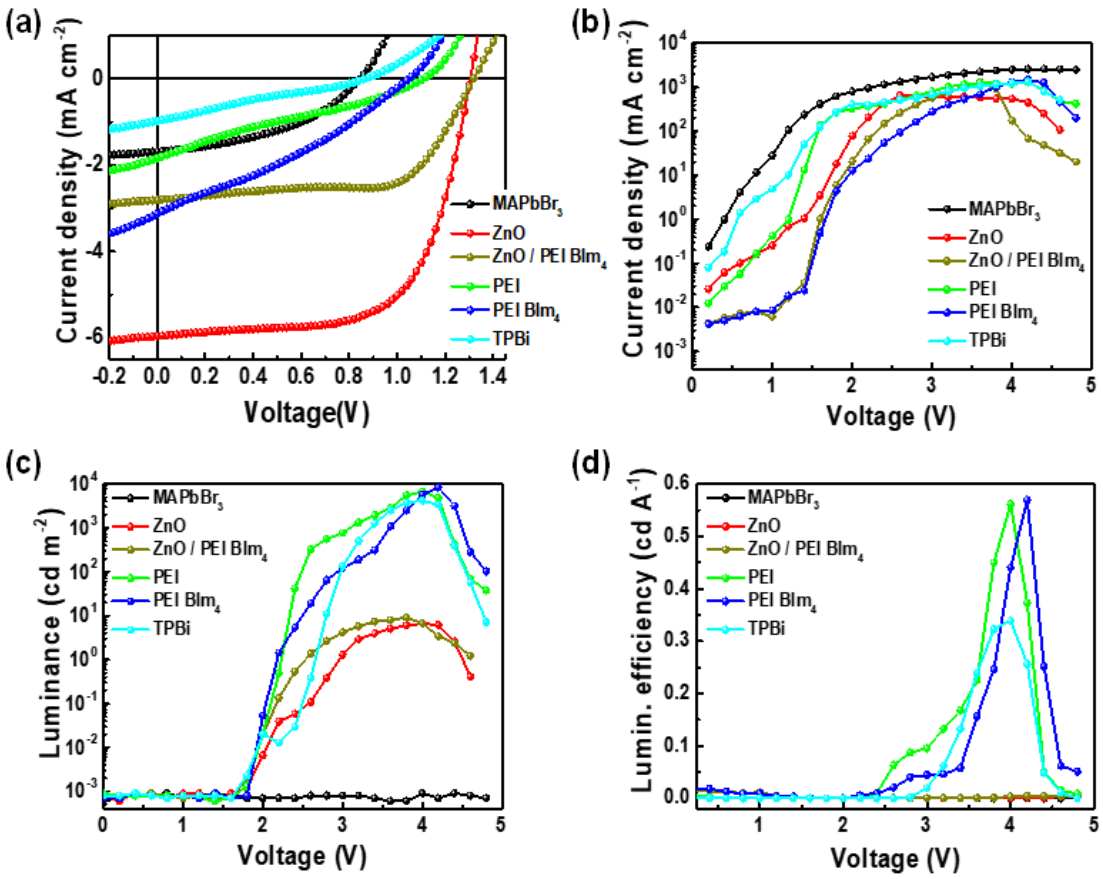

Figure 6. 6. Solar cell and LED characteristics. (a) J-V characteristics under 100 $mWcm^{-2}$ simulated solar irradiation. (b) J-V characteristics under forward bias. (c) Luminance vs applied bias. (d) Luminous efficiency vs applied bias.

As expected, these devices yielded reasonably good LED performance with a luminance of over 4000 cdm^{-2}, current efficiency of 0.34 cdA^{-1} and luminous efficiency of 0.27 lmW^{-1}. The SC performance, however, was rather poor (~0.2%), presumably due the Φ_{ext} caused by the high-lying TPBI LUMO band.

ZnO was employed as an ETL which led to good SC performance including a *J*sc *V*oc, *FF* and PCE of 5.96 $mAcm^{-2}$, 1.31 V, 0.65 and 5.02%, however, almost no electroluminescence was observed in this device. This behavior is consistent with the large barrier (Φ_{inj} = 0.71 eV) for electrons being injected into the conduction band of $MAPbBr_3$. Thus, it is apparent that electrons accumulate at the $MAPbBr_3$/ZnO interface and non-radiatively recombine with holes in the VB of $MAPbBr_3$ under forward bias in this architecture.

Table 6. 2. Optoelectronic characteristics of peroptronic devices.

ETL	Solar Cell Characteristics				LED Characteristics*			
	J_{SC} ($mAcm^{-2}$)	V_{OC} (V)	FF	PCE (%)	L_{max} (cdm^{-2})	$\eta_{current}$ (cdA^{-1})	$\eta_{luminance}$ (lmW^{-1})	EQE (%)
none	1.69	0.85	0.43	0.61	0.0009 @ 4.0	0 @ 4.0	0 @ 4.0	0 @ 4.0
ZnO	5.96	1.31	0.65	5.02	6.7 @ 4.0	0.0014 @ 4.2	0.001 @ 4.2	0.0003 @ 4.0
PEI	1.84	1.11	0.26	0.53	6700 @ 4.0	0.56 @ 4.0	0.44 @ 4.0	0.12 @ 4.0
PEI BIm_4	3.12	1.05	0.31	1.02	8400 @ 4.2	0.57 @ 4.2	0.43 @ 4.2	0.12 @ 4.2
ZnO/PEI BIm_4	2.80	1.32	0.65	2.41	9.0 @ 3.8	0.05 @ 4.2	0.0038 @ 4.2	0.0011 @ 4.2
TPBI	0.98	0.87	0.23	0.19	4200 @ 4.0	0.34 @ 4.0	0.27 @ 3.8	0.075 @ 4.0

The data corresponding to these devices are included in **Figure 6.7, Table 6.3**. Control devices were prepared using TPBI, which has previously been used effectively in perovskite LEDs as ETLs.[142]

We anticipated that PEI, which is known as an exceptionally effective ETL in a variety of devices, would function well in both LED and SC operation. We found that the performance in LED operation was good (brightness of 6700 cdm^{-2}, current efficiency of 0.56 cdA^{-1} and luminous efficiency of 0.44 lmW^{-1}) while the SC PCE was modest (0.5 %).

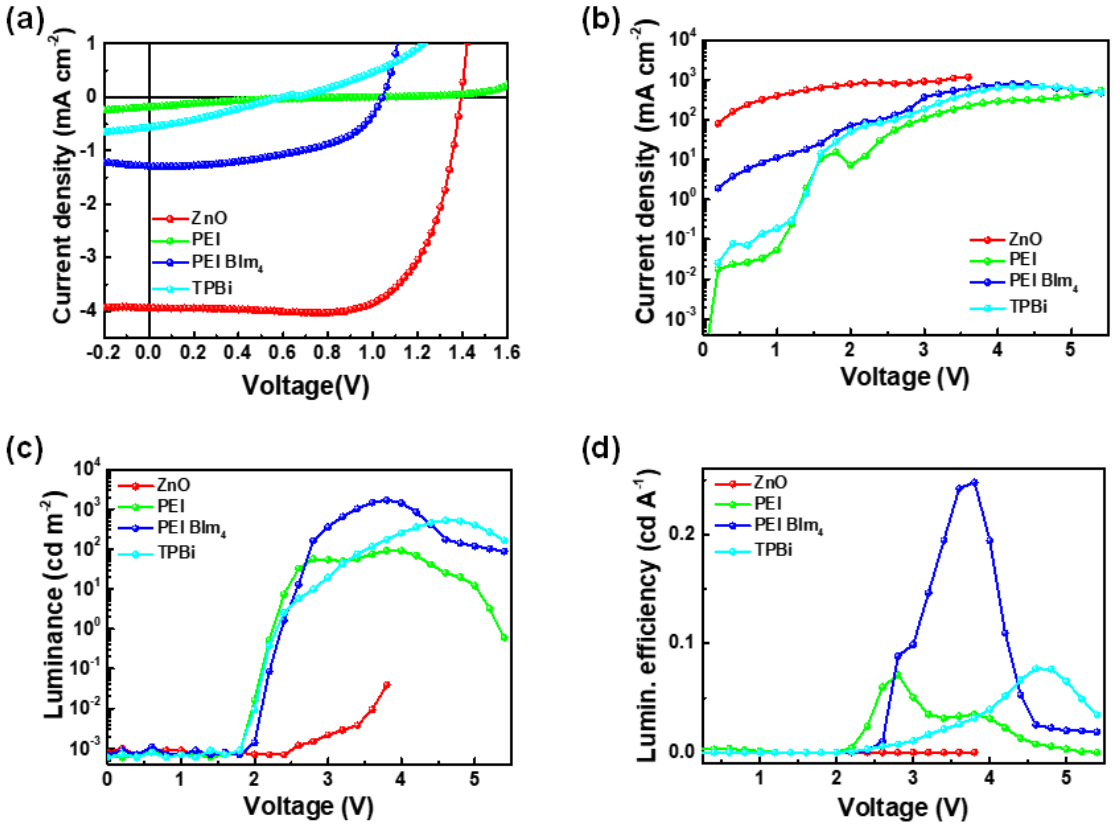

Figure 6. 7. Solar cell and LED characteristics of $MAPbBr_3$ devices prepared using the 2-step method. (a) J-V characteristics under 100 mW/cm-2 simulated solar irradiation. (b) J-V characteristics under forward bias. (c) Luminance vs applied bias. (d) Luminous efficiency vs applied bias.

We found that the performance in LED operation was good (brightness of 6700 cdm^{-2}, current efficiency of 0.56 cdA^{-1} and luminous efficiency of 0.44 lmW^{-1}) while the SC PCE was modest (0.5 %). In particular, a low J_{SC} was produced by SCs incorporating only a PEI layer; considering the low current in these devices relative to other ETLs, it appears that the PEI layer causes an excessive increase in series resistance.

Although the SC performance of peroptronic devices employing PEI BIm_4 as an ETL was somewhat less than ZnO, the LED performance was better than any other ETL explored in this study and led to a good balance between LED and SC performance. These devices exhibited SC performance including a J_{sc}, V_{oc}, FF and PCE of 3.1 $mAcm^{-2}$, 1.05 V, 0.31 and 1.02 %, with LED characteristics including a brightness of 8400 cdm^{-2}, current efficiency of 0.57 cdA^{-1} and luminous efficiency of 0.43 lmW^{-1}. The high performance observed in these devices can be attributed to a larger band-bending effect and higher conductivity for the ironically doped ETL compared to pristine PEI. For comparison, devices incorporating both ZnO and PEI BIm_4 layers were investigated. These devices showed intermediate SC performance between ZnO and PEI BIm_4 devices, with poor LED performance, indicating that the ZnO in the binary ETL still promoted non-radiative carrier recombination.

Table 6. 3. Optoelectronic characteristics of LESC devices with $MAPbBr_3$ prepared by the two-step method.

ETL	Solar Cell Characteristics				LED Characteristics*			
	J_{sc} (mA/cm^2)	V_{oc} (V)	FF	PCE (%)	L_{max} [cd m^{-2}]	L_{max} [cd A^{-}]	L_{max} [lm W^{-}]	EQE [%]
ZnO	3.93	1.39	0.72	3.92	0.039 @ 3.8	0.00002 @ 3.8	0.000016 @ 3.8	0
PEI	0.18	0.85	0.17	0.025	91.55 @ 3.8	0.071 @ 2.8	0.08 @ 2.8	0.016 @ 2.8
PEI Blm_4	1.29	1.04	0.52	0.70	1685.30 @ 3.8	0.25 @ 3.8	0.21 @ 3.6	0.056 @ 3.8
TPBI	0.56	0.59	0.29	0.096	525.65 @ 4.6	0.077 @ 4.6	0.052 @ 4.6	0.017 @ 4.6

6.4 Conclusion

We have demonstrated, for the first time, peroptronic devices based on solution processed $MAPbBr_3$ active layer which exhibit photovoltaic PCEs of over 1% and luminous efficiencies of over 0.4 lmW^{-1}. It is apparent that PEI and its derivative PEI BIm_4 are able to overcome the problem of simultaneously achieving efficient electron injection and extraction from perovskite active layers. We have interpreted the mechanism of these ETLs as causing an increase in the E_F of the $MAPbBr_3$ layer, or n-doping. Considering that no electron accepting material is present, this result implies that these ETLs result in the formation of a $MAPbBr_3$ homojunction, which is consistent with the observation of LESC behavior in some high-quality inorganic semiconductor homojunctions such as GaAs.[151] It is worth noting that a hole injection barrier exists between the PEDOT:PSS and $MAPbBr_3$ layers; we anticipate that improved performance can be achieved if the hole injection / extraction issue in this architecture is investigated in greater detail as well.[152, 153] This type of device opens the possibility for an interesting new range of applications for perovskite semiconductors, such as low-cost optical communications elements or self-powered displays

CHAPTER 7. Summary

In this thesis, I focused on various interfacial engineering which are organic surface modifiers (OSMs) effect using both 4-chlorobenzoic acid (CBA) and ethanolamine (ETA) as a self-assembled mono layer with small molecule materials in both conventional and inverted organic solar cells, and hole transport layer (HTL) using conjugated polyelectrolytes (CPEs) materials with perovskite based solar cells. And light-emitting solar cells (LESCs) of novel device architecture with a polyelectrolyte based on a partially protonated PEI backbone with tetraimadazolylborate anions (PEI BIm_4) resulting in minimize energetic barrier to provide two functions to single device, well-shift energy level to make selective good pathway for holes and electrons, and overcoming problem of LESCs, respectively, for the enhanced performance optoelectronic devices.

Firstly, I successfully replacement PEDOT:PSS as a hole transport layer (HTL) using organic modifier. The organic modifier incorporated chlorobenzoic acid (CBA) exhibited a high work function of ITO electrode, high transparency, and a hydrophobic surface by a simple spin-coating method produces. As an alternative to PEDOT:PSS, CBA modification achieves efficiency enhancement up to 8.5%, which is attributed to enhanced light absorption within the active layer and smooth hole transport from the active layer to the anode.

Secondly, I successfully replacement metal oxide as an electron transport layer (ETL) using small-molecule organic modifier. That investigate a simple fabrication method for vapor coating small-molecule organic interlayers as replacements for metal oxide films. The interfacial layers, which serve both as both surface modifiers to reduce the work function of substrate and electron selective layers, maximize light absorption within the active layer while improving electron transport and compatibility between the active layer and cathode, enhancement in power conversion efficiency and similar air stability compared to devices using a ZnO layer.

Thirdly, I successfully employed pH-neutral and low-temperature solution-processable conjugated polyelectrolytes (CPEs), particularly CPE-K as the HTL in inverted-type perovskite based solar cells. Excellent wetting of perovskite precursor solution on the CPE-K layer leads to uniform active layer film with complete surface coverage and superior hole selectivity for facilitating hole transport from perovskite to the ITO anode. As a result, the device with CPE-K shows higher device efficiency, more than 12% higher than the efficiency of the device fabricated with commonly used PEDOT:PSS. Furthermore, CPE-K improves the device stability in ambient air because of the neutral pH of the

under layer. As an alternative to PEDOT:PSS and p-type metal oxides, CPE-K is a promising hole transport material for efficient p-i-n planar heterojunction perovskite solar cells that can be used on flexible substrates via roll-to-roll processing due to solution process method produces. This procedure also offers a new approach to design hybrid tandem solar cells employing CPE-K as the intermediate layer, and combining organometallic perovskites and small bandgap organic semiconductors as the active layer.

Finally, I demonstrated, for the first time, a novel architecture that performs two functions in a single device using a polyelectrolytes ETLs by combination synthesis PEI and tetraimadazolylborate anions (PEI BIm_4) and are able to overcome the problem of simultaneously achieving efficient electron injection and extraction from perovskite active layers. As a result, the devices based on solution-processable perovskite active layer ($MAPbBr_3$) which shows solar cells efficiencies of over 1% and luminous efficiencies of over 0.4 lm/W. The interpretation of mechanism is demonstrated by shifted Fermi level (E_F) of the perovskite active layer, these ETLs as causing an increase in n-doping. If considering that no n-type acceptor material is existent, this result suggests that these ETLs result in the creation of perovskite homojunction, which is consistent with the observation of LESC behavior in some high-quality inorganic homojunctions semiconductor such as GaAS. The novel approach for band structure engineering via interfacial layer enables two functions of a single device and provides more chances for researchers to improve the performance of optoelectronic devices. Furthermore, we expect that improved performance can be achieved if the charge carrier injection or extraction issue in this architecture is investigated in greater detail as well. This type of device chances the possibility for interesting new applications for perovskite semiconductors, such as self-powered displays.

I have demonstrated interfacial engineering of small molecule and polyelectrolyte materials for optoelectronic device applications. The research was designed focusing on simple fabrication, low cost, and low temperature solution processing in optoelectronic devices while maintaining high performance efficiency. In the case of LESCs, I have attempt to apply to suit both solar cells and light-emitted diodes as efficient ETLs (or EILs) by considering its advantage that two functions are required to efficiently operation a single device. These studies have diverse advantages and it will offer a great potential for optoelectronic device application with simple method, flexibility films and significantly reduced cost.

References

1. Becquerel, A., Recherches sur les effets de la radiation chimique de la lumière solaire au moyen des courants électriques. *C. R. Acad. Sci.* **1839,** *9*, 145-149.
2. Volmer, M., Die verschiedenen lichtelektrischen Erscheinungen am Anthracen, ihre Beziehungen zueinander, zur Fluoreszenz und Dianthracenbildung. *Ann. d. Phys., Lpz.* **1913,** *345* (4), 775-796.
3. Tang, C. W., Two-layer organic photovoltaic cell. *Appl. Phys. Lett.* **1986,** *48* (2), 183-185.
4. Sariciftci, N. S.; Smilowitz, L.; Heeger, A. J.; Wudl, F., Photoinduced Electron Transfer from a Conducting Polymer to Buckminsterfullerene. *Science* **1992,** *258* (5087), 1474-1476.
5. Morita, S.; Zakhidov, A. A.; Yoshino, K., Doping effect of buckminsterfullerene in conducting polymer: Change of absorption spectrum and quenching of luminescene. *Solid State Commun.* **1992,** *82* (4), 249-252.
6. Yu, G.; Gao, J.; Hummelen, J. C.; Wudl, F.; Heeger, A. J., Polymer Photovoltaic Cells: Enhanced Efficiencies via a Network of Internal Donor-Acceptor Heterojunctions. *Science* **1995,** *270* (5243), 1789-1791.
7. Siddiki, M. K.; Li, J.; Galipeau, D.; Qiao, Q., A review of polymer multijunction solar cells. *Energy Environ. Sci.* **2010,** *3* (7), 867-883.
8. Saunders, B. R.; Turner, M. L., Nanoparticle–polymer photovoltaic cells. *Adv. Colloid Interface Sci.* **2008,** *138* (1), 1-23.
9. Heremans, P.; Cheyns, D.; Rand, B. P., Strategies for increasing the efficiency of heterojunction organic solar cells: material selection and device architecture. *Acc. Chem. Res.* **2009,** *42* (11), 1740-1747.
10. Brédas, J.-L.; Norton, J. E.; Cornil, J.; Coropceanu, V., Molecular understanding of organic solar cells: the challenges. *Acc. Chem. Res.* **2009,** *42* (11), 1691-1699.
11. Peumans, P.; Yakimov, A.; Forrest, S. R., Small molecular weight organic thin-film

photodetectors and solar cells. *J. Appl. Phys.* **2003,** *93* (7), 3693-3723.

12. Brabec, C. J.; Cravino, A.; Meissner, D.; Sariciftci, N. S.; Fromherz, T.; Rispens, M. T.; Sanchez, L.; Hummelen, J. C., Origin of the open circuit voltage of plastic solar cells. *Adv. Funct. Mater.* **2001,** *11* (5), 374-380.
13. Li, G.; Shrotriya, V.; Yao, Y.; Huang, J.; Yang, Y., Manipulating regioregular poly (3-hexylthiophene):[6, 6]-phenyl-C 61-butyric acid methyl ester blends—route towards high efficiency polymer solar cells. *J. Mater. Chem.* **2007,** *17* (30), 3126-3140.
14. Ameri, T.; Dennler, G.; Lungenschmied, C.; Brabec, C. J., Organic tandem solar cells: a review. *Energy Environ. Sci.* **2009,** *2* (4), 347-363.
15. Gur, I.; Fromer, N. A.; Chen, C.-P.; Kanaras, A. G.; Alivisatos, A. P., Hybrid solar cells with prescribed nanoscale morphologies based on hyperbranched semiconductor nanocrystals. *Nano Lett.* **2007,** *7* (2), 409-414.
16. Schilinsky, P.; Waldauf, C.; Hauch, J.; Brabec, C. J., Simulation of light intensity dependent current characteristics of polymer solar cells. *J. Appl. Phys.* **2004,** *95* (5), 2816-2819.
17. Riordan, C.; Hulstron, R. In *What is an air mass 1.5 spectrum? (solar cell performance calculations)*, IEEE Conference on Photovoltaic Specialists, 21-25 May 1990; 1990; pp 1085-1088 vol.2.
18. Kojima, A.; Teshima, K.; Shirai, Y.; Miyasaka, T., Organometal Halide Perovskites as Visible-Light Sensitizers for Photovoltaic Cells. *J. Am. Chem. Soc.* **2009,** *131* (17), 6050-6051.
19. Kim, H.-S.; Lee, C.-R.; Im, J.-H.; Lee, K.-B.; Moehl, T.; Marchioro, A.; Moon, S.-J.; Humphry-Baker, R.; Yum, J.-H.; Moser, J. E.; Grätzel, M.; Park, N.-G., Lead Iodide Perovskite Sensitized All-Solid-State Submicron Thin Film Mesoscopic Solar Cell with Efficiency Exceeding 9%. *Sci. Rep.* **2012,** *2*, 591.
20. Lee, M. M.; Teuscher, J.; Miyasaka, T.; Murakami, T. N.; Snaith, H. J., Efficient Hybrid Solar Cells Based on Meso-Superstructured Organometal Halide Perovskites. *Science* **2012,** *338* (6107), 643.

21. Prasanna, R.; Gold-Parker, A.; Leijtens, T.; Conings, B.; Babayigit, A.; Boyen, H.-G.; Toney, M. F.; McGehee, M. D., Band Gap Tuning via Lattice Contraction and Octahedral Tilting in Perovskite Materials for Photovoltaics. *J. Am. Chem. Soc.* **2017,** *139* (32), 11117-11124.

22. Noh, J. H.; Im, S. H.; Heo, J. H.; Mandal, T. N.; Seok, S. I., Chemical Management for Colorful, Efficient, and Stable Inorganic–Organic Hybrid Nanostructured Solar Cells. *Nano Lett.* **2013,** *13* (4), 1764-1769.

23. Hill, R., Energy-gap variations in semiconductor alloys. *J. Phys. C Solid State Phys.* **1974,** *7* (3), 521.

24. Venugopal, R.; Lin, P.-I.; Chen, Y.-T., Photoluminescence and Raman Scattering from Catalytically Grown ZnxCd1-xSe Alloy Nanowires. *J. Phys. Chem. B* **2006,** *110* (24), 11691-11696.

25. Chueh, C.-C.; Li, C.-Z.; Jen, A. K. Y., Recent progress and perspective in solution-processed Interfacial materials for efficient and stable polymer and organometal perovskite solar cells. *Energy Environ. Sci.* **2015,** *8* (4), 1160-1189.

26. Braun, S.; Salaneck, W. R.; Fahlman, M., Energy-Level Alignment at Organic/Metal and Organic/Organic Interfaces. *Adv. Mater.* **2009,** *21* (14-15), 1450-1472.

27. Zenasni, O.; Jamison, A. C.; Lee, T. R., The impact of fluorination on the structure and properties of self-assembled monolayer films. *Soft Matter* **2013,** *9* (28), 6356-6370.

28. Walker, B.; Choi, H.; Kim, J. Y., Interfacial engineering for highly efficient organic solar cells. *Curr. Appl. Phys.* **2017,** *17* (3), 370-391.

29. Cabanetos, C.; El Labban, A.; Bartelt, J. A.; Douglas, J. D.; Mateker, W. R.; Fréchet, J. M. J.; McGehee, M. D.; Beaujuge, P. M., Linear Side Chains in Benzo[1,2-b:4,5-b′]dithiophene–Thieno[3,4-c]pyrrole-4,6-dione Polymers Direct Self-Assembly and Solar Cell Performance. *J. Am. Chem. Soc.* **2013,** *135* (12), 4656-4659.

30. Kim, J. Y.; Kim, S. H.; Lee, H. H.; Lee, K.; Ma, W.; Gong, X.; Heeger, A. J., New

Architecture for High-Efficiency Polymer Photovoltaic Cells Using Solution-Based Titanium Oxide as an Optical Spacer. *Adv. Mater.* **2006,** *18* (5), 572-576.

31. Kim, J. Y.; Lee, K.; Coates, N. E.; Moses, D.; Nguyen, T.-Q.; Dante, M.; Heeger, A. J., Efficient Tandem Polymer Solar Cells Fabricated by All-Solution Processing. *Science* **2007,** *317* (5835), 222-225.
32. Chang, C.-Y.; Zuo, L.; Yip, H.-L.; Li, C.-Z.; Li, Y.; Hsu, C.-S.; Cheng, Y.-J.; Chen, H.; Jen, A. K. Y., Highly Efficient Polymer Tandem Cells and Semitransparent Cells for Solar Energy. *Adv. Energy Mater.* **2014,** *4* (7), 1301645.
33. Chen, C.-C.; Chang, W.-H.; Yoshimura, K.; Ohya, K.; You, J.; Gao, J.; Hong, Z.; Yang, Y., An Efficient Triple-Junction Polymer Solar Cell Having a Power Conversion Efficiency Exceeding 11%. *Adv. Mater.* **2014**, *26* (32), 5670-5677.
34. Chen, H.-C.; Chen, Y.-H.; Liu, C.-C.; Chien, Y.-C.; Chou, S.-W.; Chou, P.-T., Prominent Short-Circuit Currents of Fluorinated Quinoxaline-Based Copolymer Solar Cells with a Power Conversion Efficiency of 8.0%. *Chem. Mater.* **2012,** *24* (24), 4766-4772.
35. Cheng, P.; Hou, J.; Li, Y.; Zhan, X., Layer-by-Layer Solution-Processed Low-Bandgap Polymer-PC61BM Solar Cells with High Efficiency. *Adv. Energy Mater.* **2014,** *4* (9), 1301349.
36. Gu, C.; Chen, Y.; Zhang, Z.; Xue, S.; Sun, S.; Zhong, C.; Zhang, H.; Lv, Y.; Li, F.; Huang, F.; Ma, Y., Achieving High Efficiency of PTB7-Based Polymer Solar Cells via Integrated Optimization of Both Anode and Cathode Interlayers. *Adv. Energy Mater.* **2014,** *4* (8), 1301771.
37. Choi, H.; Park, J. S.; Jeong, E.; Kim, G.-H.; Lee, B. R.; Kim, S. O.; Song, M. H.; Woo, H. Y.; Kim, J. Y., Combination of Titanium Oxide and a Conjugated Polyelectrolyte for High-Performance Inverted-Type Organic Optoelectronic Devices. *Adv. Mater.* **2011,** *23* (24), 2759-2763.
38. Nguyen, T. L.; Choi, H.; Ko, S. J.; Uddin, M. A.; Walker, B.; Yum, S.; Jeong, J. E.; Yun, M. H.; Shin, T. J.; Hwang, S.; Kim, J. Y.; Woo, H. Y., Semi-crystalline photovoltaic polymers with efficiency exceeding 9% in a 300 nm thick conventional single-cell device.

Energy Environ. Sci. **2014**. 7, 3040-3051

39. Woo, S.; Hyun Kim, W.; Kim, H.; Yi, Y.; Lyu, H.-K.; Kim, Y., 8.9% Single-Stack Inverted Polymer Solar Cells with Electron-Rich Polymer Nanolayer-Modified Inorganic Electron-Collecting Buffer Layers. *Adv. Energy Mater.* **2014,** *4* (7), 1301692.
40. Ye, L.; Zhang, S.; Zhao, W.; Yao, H.; Hou, J., Highly Efficient 2D-Conjugated Benzodithiophene-Based Photovoltaic Polymer with Linear Alkylthio Side Chain. *Chem. Mater.* **2014,** *26* (12), 3603-3605.
41. *IEEE Journal of Selected Topics in Quantum Electronics* **2010,** *16* (6), 1656.
42. Zhou, H.; Zhang, Y.; Mai, C.-K.; Collins, S. D.; Nguyen, T.-Q.; Bazan, G. C.; Heeger, A. J., Conductive Conjugated Polyelectrolyte as Hole-Transporting Layer for Organic Bulk Heterojunction Solar Cells. *Adv. Mater.* **2014,** *26* (5), 780-785.
43. Wang, F.; Xu, Q.; Tan, Z. a.; Li, L.; Li, S.; Hou, X.; Sun, G.; Tu, X.; Hou, J.; Li, Y., Efficient polymer solar cells with a solution-processed and thermal annealing-free RuO2 anode buffer layer. *J. Mater. Chem. A Mater.* **2014,** *2* (5), 1318-1324.
44. Xu, Q.; Wang, F.; Tan, Z. a.; Li, L.; Li, S.; Hou, X.; Sun, G.; Tu, X.; Hou, J.; Li, Y., High-Performance Polymer Solar Cells with Solution-Processed and Environmentally Friendly CuOx Anode Buffer Layer. *ACS Appl. Mater. Interfaces* **2013,** *5* (21), 10658-10664.
45. Chen, L.-M.; Hong, Z.; Li, G.; Yang, Y., Recent Progress in Polymer Solar Cells: Manipulation of Polymer:Fullerene Morphology and the Formation of Efficient Inverted Polymer Solar Cells. *Adv. Mater.* **2009,** *21* (14-15), 1434-1449.
46. Berny, S. p.; Tortech, L.; Véber, M.; Fichou, D., Dithiapyrannylidenes as Efficient Hole Collection Interfacial Layers in Organic Solar Cells. *ACS Appl. Mater. Interfaces* **2010,** *2* (11), 3059-3068.
47. Tan, Z. a.; Qian, D.; Zhang, W.; Li, L.; Ding, Y.; Xu, Q.; Wang, F.; Li, Y., Efficient and stable polymer solar cells with solution-processed molybdenum oxide interfacial layer. *J. Mater. Chem. A Mater.* **2013,** *1* (3), 657-664.
48. Tan, Z. a.; Zhang, W.; Cui, C.; Ding, Y.; Qian, D.; Xu, Q.; Li, L.; Li, S.; Li, Y.,

Solution-processed vanadium oxide as a hole collection layer on an ITO electrode for high-performance polymer solar cells. *Phys. Chem. Chem. Phys.* **2012,** *14* (42), 14589-14595.

49. Xie, F.; Choy, W. C. H.; Wang, C.; Li, X.; Zhang, S.; Hou, J., Low-Temperature Solution-Processed Hydrogen Molybdenum and Vanadium Bronzes for an Efficient Hole-Transport Layer in Organic Electronics. *Adv. Mater.* **2013,** *25* (14), 2051-2055.

50. Knesting, K. M.; Ju, H.; Schlenker, C. W.; Giordano, A. J.; Garcia, A.; Smith, O. N. L.; Olson, D. C.; Marder, S. R.; Ginger, D. S., ITO Interface Modifiers Can Improve VOC in Polymer Solar Cells and Suppress Surface Recombination. *J. Phys. Chem. Lett.* **2013,** *4* (23), 4038-4044.

51. Wang, H.; Gomez, E. D.; Guan, Z.; Jaye, C.; Toney, M. F.; Fischer, D. A.; Kahn, A.; Loo, Y.-L., Tuning Contact Recombination and Open-Circuit Voltage in Polymer Solar Cells via Self-Assembled Monolayer Adsorption at the Organic–Metal Oxide Interface. *J. Phys. Chem. C* **2013,** *117* (40), 20474-20484.

52. Choi, H.; Lee, J.; Lee, W.; Ko, S.-J.; Yang, R.; Lee, J. C.; Woo, H. Y.; Yang, C.; Kim, J. Y., Acid-functionalized fullerenes used as interfacial layer materials in inverted polymer solar cells. *Org. Electron.* **2013,** *14* (11), 3138-3145.

53. Bulliard, X.; Ihn, S.-G.; Yun, S.; Kim, Y.; Choi, D.; Choi, J.-Y.; Kim, M.; Sim, M.; Park, J.-H.; Choi, W.; Cho, K., Enhanced Performance in Polymer Solar Cells by Surface Energy Control. *Adv. Funct. Mater.* **2010,** *20* (24), 4381-4387.

54. Yip, H.-L.; Jen, A. K. Y., Recent advances in solution-processed interfacial materials for efficient and stable polymer solar cells. *Energy Environ. Sci.* **2012,** *5* (3), 5994-6011.

55. Hau, S. K.; Yip, H.-L.; Acton, O.; Baek, N. S.; Ma, H.; Jen, A. K. Y., Interfacial modification to improve inverted polymer solar cells. *J. Mater. Chem.* **2008,** *18* (42), 5113-5119.

56. Beaumont, N.; Hancox, I.; Sullivan, P.; Hatton, R. A.; Jones, T. S., Increased efficiency in small molecule organic photovoltaic cells through electrode modification with self-assembled monolayers. *Energy Environ. Sci.* **2011,** *4* (5), 1708-1711.

57. Ma, H.; Yip, H.-L.; Huang, F.; Jen, A. K. Y., Interface Engineering for Organic Electronics. *Adv. Funct. Mater.* **2010,** *20* (9), 1371-1388.

58. Zayat, M.; Garcia-Parejo, P.; Levy, D., Preventing UV-light damage of light sensitive materials using a highly protective UV-absorbing coating. *Chem. Soc. Rev.* **2007,** *36* (8), 1270-1281.

59. Liang, Y.; Xu, Z.; Xia, J.; Tsai, S.-T.; Wu, Y.; Li, G.; Ray, C.; Yu, L., For the Bright Future—Bulk Heterojunction Polymer Solar Cells with Power Conversion Efficiency of 7.4%. *Adv. Mater.* **2010,** *22* (20), E135-E138.

60. Choi, H.; Ko, S.-J.; Choi, Y.; Joo, P.; Kim, T.; Lee, B. R.; Jung, J.-W.; Choi, H. J.; Cha, M.; Jeong, J.-R.; Hwang, I.-W.; Song, M. H.; Kim, B.-S.; Kim, J. Y., Versatile surface plasmon resonance of carbon-dot-supported silver nanoparticles in polymer optoelectronic devices. *Nat. Photon.* **2013,** *7* (9), 732-738.

61. Kim, G.-H.; Song, H.-K.; Kim, J. Y., The effect of introducing a buffer layer to polymer solar cells on cell efficiency. *Sol. Energy Mater. Sol. Cells* **2011,** *95* (4), 1119-1122.

62. Cowan, S. R.; Roy, A.; Heeger, A. J., Recombination in polymer-fullerene bulk heterojunction solar cells. *Phys. Rev. B* **2010,** *82* (24), 245207.

63. Kyaw, A. K. K.; Wang, D. H.; Gupta, V.; Zhang, J.; Chand, S.; Bazan, G. C.; Heeger, A. J., Efficient Solution-Processed Small-Molecule Solar Cells with Inverted Structure. *Adv. Mater.* **2013,** *25* (17), 2397-2402.

64. Choi, H.; Kim, H.-B.; Ko, S.-J.; Kim, G.-H.; Kim, J. Y., Vapor Coating Method Using Small-Molecule Organic Surface Modifiers to Replace N-Type Metal Oxide Layers in Inverted Polymer Solar Cells. *ACS Appl. Mater. Interfaces s* **2014,** *6* (9), 6504-6509.

65. Yu, G.; Gao, J.; Hummelen, J. C.; Wudl, F.; Heeger, A. J., Polymer photovoltaic cells: enhanced efficiencies via a network of internal donor-acceptor heterojunctions. *Science* **1995,** *270*, 1789-1791.

66. Kim, J. Y., Efficient tandem polymer solar cells fabricated by all-solution processing. *Science* **2007,** *317*, 222-225.

67. Park, S. H., Bulk heterojunction solar cells with internal quantum efficiency approaching 100%. *Nat. Photon.* **2009,** *3*, 297-302.

68. He, Z.; Zhong, C.; Su, S.; Xu, M.; Wu, H.; Cao, Y., Enhanced power-conversion efficiency in polymer solar cells using an inverted device structure. *Nat. Photon.* **2012,** *6* (9), 591-595.

69. Son, H. J.; Lu, L.; Chen, W.; Xu, T.; Zheng, T.; Carsten, B.; Strzalka, J.; Darling, S. B.; Chen, L. X.; Yu, L., Synthesis and Photovoltaic Effect in Dithieno[2,3-d:2′,3′-d′]Benzo[1,2-b:4,5-b′]dithiophene-Based Conjugated Polymers. *Adv. Mater.* **2013,** *25* (6), 838-843.

70. Wang, D. H.; Park, K. H.; Seo, J. H.; Seifter, J.; Jeon, J. H.; Kim, J. K.; Park, J. H.; Park, O. O.; Heeger, A. J., Enhanced Power Conversion Efficiency in PCDTBT/PC70BM Bulk Heterojunction Photovoltaic Devices with Embedded Silver Nanoparticle Clusters. *Adv. Energy Mater.* **2011,** *1* (5), 766-770.

71. Peet, J.; Kim, J. Y.; Coates, N. E.; Ma, W. L.; Moses, D.; Heeger, A. J.; Bazan, G. C., Efficiency enhancement in low-bandgap polymer solar cells by processing with alkane dithiols. *Nat. Mater.* **2007,** *6* (7), 497-500.

72. Lee, K.; Kim, J. Y.; Park, S. H.; Kim, S. H.; Cho, S.; Heeger, A. J., Air-Stable Polymer Electronic Devices. *Adv. Mater.* **2007,** *19* (18), 2445-2449.

73. Chen, C.-P.; Chen, Y.-D.; Chuang, S.-C., High-Performance and Highly Durable Inverted Organic Photovoltaics Embedding Solution-Processable Vanadium Oxides as an Interfacial Hole-Transporting Layer. *Adv. Mater.* **2011,** *23* (33), 3859-3863.

74. You, J.; Chen, C.-C.; Dou, L.; Murase, S.; Duan, H.-S.; Hawks, S. A.; Xu, T.; Son, H. J.; Yu, L.; Li, G.; Yang, Y., Metal Oxide Nanoparticles as an Electron-Transport Layer in High-Performance and Stable Inverted Polymer Solar Cells. *Adv. Mater.* **2012,** *24* (38), 5267-5272.

75. Sun, Y.; Seo, J. H.; Takacs, C. J.; Seifter, J.; Heeger, A. J., Inverted Polymer Solar Cells

Integrated with a Low-Temperature-Annealed Sol-Gel-Derived ZnO Film as an Electron Transport Layer. *Adv. Mater.* **2011,** *23* (14), 1679-1683.

76. Hsieh, C.-H.; Cheng, Y.-J.; Li, P.-J.; Chen, C.-H.; Dubosc, M.; Liang, R.-M.; Hsu, C.-S., Highly Efficient and Stable Inverted Polymer Solar Cells Integrated with a Cross-Linked Fullerene Material as an Interlayer. *J. Am. Chem. Soc* **2010,** *132* (13), 4887-4893.

77. Jeong, B. S.; Norton, D. P.; Budai, J. D., Conductivity in transparent anatase TiO2 films epitaxially grown by reactive sputtering deposition. *Solid-State Electronics* **2003,** *47* (12), 2275-2278.

78. Hofhuis, J.; Schoonman, J.; Goossens, A., Time-of-flight studies on TiO[sub 2]/CuInS[sub 2] heterojunctions. *J. Appl. Phys.* **2008,** *103* (1), 014503.

79. Yang, H.; Zhu, S.; Pan, N., Studying the mechanisms of titanium dioxide as ultraviolet-blocking additive for films and fabrics by an improved scheme. *J. Appl. Polym. Sci.* **2004,** *92* (5), 3201-3210.

80. Zhou, Y.; Fuentes-Hernandez, C.; Shim, J.; Meyer, J.; Giordano, A. J.; Li, H.; Winget, P.; Papadopoulos, T.; Cheun, H.; Kim, J.; Fenoll, M.; Dindar, A.; Haske, W.; Najafabadi, E.; Khan, T. M.; Sojoudi, H.; Barlow, S.; Graham, S.; Brédas, J.-L.; Marder, S. R.; Kahn, A.; Kippelen, B., A Universal Method to Produce Low–Work Function Electrodes for Organic Electronics. *Science* **2012,** *336* (6079), 327-332.

81. Na, S.-I.; Kim, T.-S.; Oh, S.-H.; Kim, J.; Kim, S.-S.; Kim, D.-Y., Enhanced performance of inverted polymer solar cells with cathode interfacial tuning via water-soluble polyfluorenes. *Appl. Phys. Let.* **2010,** *97* (22), 223305.

82. Lee, T. H.; Choi, H.; Walker, B.; Kim, T.; Kim, H.-B.; Kim, J. Y., Replacing the metal oxide layer with a polymer surface modifier for high-performance inverted polymer solar cells. *RSC Adv.* **2014,** *4* (9), 4791-4795.

83. Yang, T.; Wang, M.; Duan, C.; Hu, X.; Huang, L.; Peng, J.; Huang, F.; Gong, X., Inverted polymer solar cells with 8.4% efficiency by conjugated polyelectrolyte. *Energy Environ. Sci.* **2012,** *5* (8), 8208-8214.

84. Lee, B. R.; Jung, E. D.; Nam, Y. S.; Jung, M.; Park, J. S.; Lee, S.; Choi, H.; Ko, S.-J.; Shin, N. R.; Kim, Y.-K.; Kim, S. O.; Kim, J. Y.; Shin, H.-J.; Cho, S.; Song, M. H., Amine-Based Polar Solvent Treatment for Highly Efficient Inverted Polymer Solar Cells. *Adv. Mater.* **2013,** *26* (3), 494-500.

85. He, Z.; Zhong, C.; Su, S.; Xu, M.; Wu, H.; Cao, Y., Enhanced power-conversion efficiency in polymer solar cells using an inverted device structure. *Nat. Photon.* **2012,** *6*, 591.

86. Beek, W. J. E.; Slooff, L. H.; Wienk, M. M.; Kroon, J. M.; Janssen, R. A. J., Hybrid Solar Cells Using a Zinc Oxide Precursor and a Conjugated Polymer. *Adv. Funct. Mater.* **2005,** *15* (10), 1703-1707.

87. Choi, H.; Lee, J.-P.; Ko, S.-J.; Jung, J.-W.; Park, H.; Yoo, S.; Park, O.; Jeong, J.-R.; Park, S.; Kim, J. Y., Multipositional Silica-Coated Silver Nanoparticles for High-Performance Polymer Solar Cells. *Nano Lett.* **2013,** *13* (5), 2204-2208.

88. Gupta, V.; Kyaw, A. K. K.; Wang, D. H.; Chand, S.; Bazan, G. C.; Heeger, A. J., Barium: An Efficient Cathode Layer for Bulk-heterojunction Solar Cells. *Sci. Rep.* **2013,** *3,* 1965.

89. Wetzelaer, G. A. H.; Kuik, M.; Lenes, M.; Blom, P. W. M., Origin of the dark-current ideality factor in polymer:fullerene bulk heterojunction solar cells. *Appl. Phys. Let.* **2011,** *99* (15), 153506.

90. Xing, G.; Mathews, N.; Sun, S.; Lim, S. S.; Lam, Y. M.; Grätzel, M.; Mhaisalkar, S.; Sum, T. C., Long-Range Balanced Electron- and Hole-Transport Lengths in Organic-Inorganic CH3NH3PbI3. *Science* **2013,** *342* (6156), 344-347.

91. Stranks, S. D.; Eperon, G. E.; Grancini, G.; Menelaou, C.; Alcocer, M. J. P.; Leijtens, T.; Herz, L. M.; Petrozza, A.; Snaith, H. J., Electron-Hole Diffusion Lengths Exceeding 1 Micrometer in an Organometal Trihalide Perovskite Absorber. *Science* **2013,** *342* (6156), 341-344.

92. Choi, H.; Jeong, J.; Kim, H.-B.; Kim, S.; Walker, B.; Kim, G.-H.; Kim, J. Y., Cesium-doped methylammonium lead iodide perovskite light absorber for hybrid solar cells.

Nano Energy **2014,** *7* (0), 80-85.

93. Liu, M.; Johnston, M. B.; Snaith, H. J., Efficient planar heterojunction perovskite solar cells by vapour deposition. *Nature* **2013,** *501* (7467), 395-398.

94. Jeon, N. J.; Noh, J. H.; Kim, Y. C.; Yang, W. S.; Ryu, S.; Seok, S. I., Solvent engineering for high-performance inorganic–organic hybrid perovskite solar cells. *Nat. Mater.* **2014,** *13* (9), 897-903.

95. Zhou, H.; Chen, Q.; Li, G.; Luo, S.; Song, T.-b.; Duan, H.-S.; Hong, Z.; You, J.; Liu, Y.; Yang, Y., Interface engineering of highly efficient perovskite solar cells. *Science* **2014,** *345* (6196), 542-546.

96. Kim, H.-B.; Choi, H.; Jeong, J.; Kim, S.; Walker, B.; Song, S.; Kim, J. Y., Mixed solvents for the optimization of morphology in solution-processed, inverted-type perovskite/fullerene hybrid solar cells. *Nanoscale* **2014,** *6* (12), 6679-6683.

97. Jeng, J.-Y.; Chiang, Y.-F.; Lee, M.-H.; Peng, S.-R.; Guo, T.-F.; Chen, P.; Wen, T.-C., CH3NH3PbI3 Perovskite/Fullerene Planar-Heterojunction Hybrid Solar Cells. *Adv. Mater.* **2013,** *25* (27), 3727-3732.

98. Malinkiewicz, O.; Yella, A.; Lee, Y. H.; Espallargas, G. M.; Graetzel, M.; Nazeeruddin, M. K.; Bolink, H. J., Perovskite solar cells employing organic charge-transport layers. *Nat. Photon.* **2014,** *8* (2), 128-132.

99. Conings, B.; Baeten, L.; De Dobbelaere, C.; D'Haen, J.; Manca, J.; Boyen, H.-G., Perovskite-Based Hybrid Solar Cells Exceeding 10% Efficiency with High Reproducibility Using a Thin Film Sandwich Approach. *Adv. Mater.* **2014,** *26* (13), 2041-2046.

100. Docampo, P.; Ball, J. M.; Darwich, M.; Eperon, G. E.; Snaith, H. J., Efficient organometal trihalide perovskite planar-heterojunction solar cells on flexible polymer substrates. *Nat. Commun.* **2013,** *4*, 2761.

101. Wang, K.-C.; Jeng, J.-Y.; Shen, P.-S.; Chang, Y.-C.; Diau, E. W.-G.; Tsai, C.-H.; Chao, T.-Y.; Hsu, H.-C.; Lin, P.-Y.; Chen, P.; Guo, T.-F.; Wen, T.-C., p-type Mesoscopic Nickel Oxide/Organometallic Perovskite Heterojunction Solar Cells. *Sci. Rep.*

2014, *4*, 4756.

102. Polander, L. E.; Pahner, P.; Schwarze, M.; Saalfrank, M.; Koerner, C.; Leo, K., Hole-transport material variation in fully vacuum deposited perovskite solar cells. *APL Mater.* **2014,** *2* (8), 081503.

103. Malinkiewicz, O.; Roldán-Carmona, C.; Soriano, A.; Bandiello, E.; Camacho, L.; Nazeeruddin, M. K.; Bolink, H. J., Metal-Oxide-Free Methylammonium Lead Iodide Perovskite-Based Solar Cells: the Influence of Organic Charge Transport Layers. *Adv. Energy Mater.* **2014,** *4* (15), 1400345.

104. Mai, C.-K.; Zhou, H.; Zhang, Y.; Henson, Z. B.; Nguyen, T.-Q.; Heeger, A. J.; Bazan, G. C., Facile Doping of Anionic Narrow-Band-Gap Conjugated Polyelectrolytes During Dialysis. *Angew. Chem. Int. Ed.* **2013,** *52* (49), 12874-12878.

105. Mai, C.-K.; Schlitz, R. A.; Su, G. M.; Spitzer, D.; Wang, X.; Fronk, S. L.; Cahill, D. G.; Chabinyc, M. L.; Bazan, G. C., Side-Chain Effects on the Conductivity, Morphology, and Thermoelectric Properties of Self-Doped Narrow-Band-Gap Conjugated Polyelectrolytes. *J. Am. Chem. Soc.* **2014,** *136* (39), 13478-13481.

106. Liang, P.-W.; Liao, C.-Y.; Chueh, C.-C.; Zuo, F.; Williams, S. T.; Xin, X.-K.; Lin, J.; Jen, A. K. Y., Additive Enhanced Crystallization of Solution-Processed Perovskite for Highly Efficient Planar-Heterojunction Solar Cells. *Adv. Mater.* **2014,** *26* (22), 3748-3754.

107. Kim, J. H.; Liang, P.-W.; Williams, S. T.; Cho, N.; Chueh, C.-C.; Glaz, M. S.; Ginger, D. S.; Jen, A. K. Y., High-Performance and Environmentally Stable Planar Heterojunction Perovskite Solar Cells Based on a Solution-Processed Copper-Doped Nickel Oxide Hole-Transporting Layer. *Adv. Mater.* **2015,** *27* (4), 695-701.

108. Kutes, Y.; Ye, L.; Zhou, Y.; Pang, S.; Huey, B. D.; Padture, N. P., Direct Observation of Ferroelectric Domains in Solution-Processed CH3NH3PbI3 Perovskite Thin Films. *J. Phys. Chem. Lett.* **2014,** *5* (19), 3335-3339.

109. Sun, S.; Salim, T.; Mathews, N.; Duchamp, M.; Boothroyd, C.; Xing, G.; Sum, T. C.; Lam, Y. M., The origin of high efficiency in low-temperature solution-processable bilayer

organometal halide hybrid solar cells. *Energy Environ. Sci.* **2014,** *7* (1), 399-407.

110. You, J.; Hong, Z.; Yang, Y.; Chen, Q.; Cai, M.; Song, T.-B.; Chen, C.-C.; Lu, S.; Liu, Y.; Zhou, H., Low-Temperature Solution-Processed Perovskite Solar Cells with High Efficiency and Flexibility. *ACS Nano* **2014,** *8* (2), 1674-1680.

111. Wang, Q.; Shao, Y.; Dong, Q.; Xiao, Z.; Yuan, Y.; Huang, J., Large fill-factor bilayer iodine perovskite solar cells fabricated by a low-temperature solution-process. *Energy Environ. Sci.* **2014,** *7* (7), 2359-2365.

112. Seo, J.; Park, S.; Chan Kim, Y.; Jeon, N. J.; Noh, J. H.; Yoon, S. C.; Seok, S. I., Benefits of very thin PCBM and LiF layers for solution-processed p-i-n perovskite solar cells. *Energy Environ. Sci.* **2014,** *7* (8), 2642-2646.

113. Yu, H.; Wang, F.; Xie, F.; Li, W.; Chen, J.; Zhao, N., The Role of Chlorine in the Formation Process of "CH3NH3PbI3-xClx" Perovskite. *Adv. Funct. Mater.* **2014**, *24* (45), 7102-7108.

114. Frost, J. M.; Butler, K. T.; Brivio, F.; Hendon, C. H.; van Schilfgaarde, M.; Walsh, A., Atomistic Origins of High-Performance in Hybrid Halide Perovskite Solar Cells. *Nano Lett.* **2014,** *14* (5), 2584-2590.

115. Yang, W. S.; Noh, J. H.; Jeon, N. J.; Kim, Y. C.; Ryu, S.; Seo, J.; Seok, S. I., High-performance photovoltaic perovskite layers fabricated through intramolecular exchange. *Science* **2015,** *348* (6240), 1234-1237.

116. Green, M. A.; Ho-Baillie, A.; Snaith, H. J., The emergence of perovskite solar cells. *Nat. Photon.* **2014,** *8* (7), 506-514.

117. Saparov, B.; Mitzi, D. B., Organic–Inorganic Perovskites: Structural Versatility for Functional Materials Design. *Chem. Rev.* **2016,** *116* (7), 4558-4596.

118. Kojima, A.; Teshima, K.; Shirai, Y.; Miyasaka, T., Organometal Halide Perovskites as Visible-Light Sensitizers for Photovoltaic Cells. *J. Am. Chem. Soc.* **2009,** *131* (17), 6050-6051.

119. Green, M. A.; Hishikawa, Y.; Warta, W.; Dunlop, E. D.; Levi, D. H.; Hohl-Ebinger, J.; Ho-Baillie, A. W. H., Solar cell efficiency tables (version 50). *Prog. Photovol: Res. Appl.* **2017,**

25 (7), 668-676.

120. Sutherland, B. R.; Sargent, E. H., Perovskite photonic sources. *Nat. Photon.* **2016,** *10* (5), 295-302.

121. Veldhuis, S. A.; Boix, P. P.; Yantara, N.; Li, M.; Sum, T. C.; Mathews, N.; Mhaisalkar, S. G., Perovskite Materials for Light-Emitting Diodes and Lasers. *Adv. Mater.* **2016,** *28* (32), 6804-6834.

122. Tan, Z.-K.; Moghaddam, R. S.; Lai, M. L.; Docampo, P.; Higler, R.; Deschler, F.; Price, M.; Sadhanala, A.; Pazos, L. M.; Credgington, D.; Hanusch, F.; Bein, T.; Snaith, H. J.; Friend, R. H., Bright light-emitting diodes based on organometal halide perovskite. *Nat. Nanotechnol.* **2014,** *9* (9), 687-692.

123. Kim, H.; Lim, K.-G.; Lee, T.-W., Planar heterojunction organometal halide perovskite solar cells: roles of interfacial layers. *Energy Environ. Sci.* **2016,** *9* (1), 12-30.

124. Lim, K.-G.; Ahn, S.; Kim, Y.-H.; Qi, Y.; Lee, T.-W., Universal energy level tailoring of self-organized hole extraction layers in organic solar cells and organic-inorganic hybrid perovskite solar cells. *Energy Environ. Sci.* **2016,** *9* (3), 932-939.

125. Bi, D.; Tress, W.; Dar, M. I.; Gao, P.; Luo, J.; Renevier, C.; Schenk, K.; Abate, A.; Giordano, F.; Correa Baena, J.-P.; Decoppet, J.-D.; Zakeeruddin, S. M.; Nazeeruddin, M. K.; Grätzel, M.; Hagfeldt, A., Efficient luminescent solar cells based on tailored mixed-cation perovskites. *Sci. Adv.* **2016,** *2* (1), e1501170.

126. Swarnkar, A.; Marshall, A. R.; Sanehira, E. M.; Chernomordik, B. D.; Moore, D. T.; Christians, J. A.; Chakrabarti, T.; Luther, J. M., Quantum dot–induced phase stabilization of α-CsPbI3 perovskite for high-efficiency photovoltaics. *Science* **2016,** *354* (6308), 92-95.

127. Krebs, F. C.; Nielsen, T. D.; Fyenbo, J.; Wadstrom, M.; Pedersen, M. S., Manufacture, integration and demonstration of polymer solar cells in a lamp for the "Lighting Africa" initiative. *Energy Environ. Sci.* **2010,** *3* (5), 512-525.

128. Mims, F. M., Sun photometer with light-emitting diodes as spectrally selective detectors. *Appl. Opt.* **1992,** *31* (33), 6965-6967.

129. Morys, M.; Mims, F. M.; Hagerup, S.; Anderson, S. E.; Baker, A.; Kia, J.; Walkup, T., Design, calibration, and performance of MICROTOPS II handheld ozone monitor and Sun photometer. *J. Geophys. Res. Atmos.* **2001,** *106* (D13), 14573-14582.

130. Hamilton, B. H.; Kelly, K. A.; Malasi, W.; Ziegler, C. J., Tetrakis(imidazolyl)borate-Based Coordination Polymers: Group II Network Solids, M[B(Im)4]2(H2O)2 (M = Mg, Ca, Sr). *Inorg. Chem.* **2003,** *42* (9), 3067-3073.

131. Cheng, Y.; Yang, Q.-D.; Xiao, J.; Xue, Q.; Li, H.-W.; Guan, Z.; Yip, H.-L.; Tsang, S.-W., Decomposition of Organometal Halide Perovskite Films on Zinc Oxide Nanoparticles. *ACS Appl. Mater. Interfaces* **2015,** *7* (36), 19986-19993.

132. Edri, E.; Kirmayer, S.; Kulbak, M.; Hodes, G.; Cahen, D., Chloride Inclusion and Hole Transport Material Doping to Improve Methyl Ammonium Lead Bromide Perovskite-Based High Open-Circuit Voltage Solar Cells. *J. Phys. Chem. Lett.* **2014,** *5* (3), 429-433.

133. Heo, J. H.; Song, D. H.; Im, S. H., Planar CH3NH3PbBr3 Hybrid Solar Cells with 10.4% Power Conversion Efficiency, Fabricated by Controlled Crystallization in the Spin-Coating Process. *Adv. Mater.* **2014,** *26* (48), 8179-8183.

134. Cho, H.; Jeong, S.-H.; Park, M.-H.; Kim, Y.-H.; Wolf, C.; Lee, C.-L.; Heo, J. H.; Sadhanala, A.; Myoung, N.; Yoo, S.; Im, S. H.; Friend, R. H.; Lee, T.-W., Overcoming the electroluminescence efficiency limitations of perovskite light-emitting diodes. *Science* **2015,** *350* (6265), 1222-1225.

135. Xiao, Z.; Kerner, R. A.; Zhao, L.; Tran, N. L.; Lee, K. M.; Koh, T.-W.; Scholes, G. D.; Rand, B. P., Efficient perovskite light-emitting diodes featuring nanometre-sized crystallites. *Nat. Photon.* **2017,** *11* (2), 108-115.

136. Burschka, J.; Pellet, N.; Moon, S.-J.; Humphry-Baker, R.; Gao, P.; Nazeeruddin, M. K.; Gratzel, M., Sequential deposition as a route to high-performance perovskite-sensitized solar cells. *Nature* **2013,** *499* (7458), 316-319.

137. Poglitsch, A.; Weber, D., Dynamic disorder in methylammoniumtrihalogenoplumbates (II) observed by millimeter-wave spectroscopy. *J. Chem. Phys.* **1987,** *87* (11), 6373-6378.

138. Patterson, A. L., The Scherrer Formula for X-Ray Particle Size Determination. *Phys. Rev.* **1939,** *56* (10), 978-982.

139. Kim, Y.-H.; Cho, H.; Lee, T.-W., Metal halide perovskite light emitters. *Proc. Natl. Acad. Sci.* **2016,** *113* (42), 11694-11702.

140. Wright, A. D.; Verdi, C.; Milot, R. L.; Eperon, G. E.; Perez-Osorio, M. A.; Snaith, H. J.; Giustino, F.; Johnston, M. B.; Herz, L. M., Electron-phonon coupling in hybrid lead halide perovskites. *Nat. Commun.* **2016,** *7*, 11755.

141. Walker, B.; Ullah, M.; Chae, G. J.; Burn, P. L.; Cho, S.; Kim, J. Y.; Namdas, E. B.; Seo, J. H., High mobility solution-processed hybrid light emitting transistors. *Appl. Phys. Lett.* **2014,** *105* (18), 183302.

142. Kim, Y.-H.; Cho, H.; Heo, J. H.; Kim, T.-S.; Myoung, N.; Lee, C.-L.; Im, S. H.; Lee, T.-W., Multicolored Organic/Inorganic Hybrid Perovskite Light-Emitting Diodes. *Adv. Mater.* **2015,** *27* (7), 1248-1254.

143. Hoye, R. L. Z.; Chua, M. R.; Musselman, K. P.; Li, G.; Lai, M.-L.; Tan, Z.-K.; Greenham, N. C.; MacManus-Driscoll, J. L.; Friend, R. H.; Credgington, D., Enhanced Performance in Fluorene-Free Organometal Halide Perovskite Light-Emitting Diodes using Tunable, Low Electron Affinity Oxide Electron Injectors. *Adv. Mater.* **2015,** *27* (8), 1414-1419.

144. Yu, J. C.; Kim, D. B.; Baek, G.; Lee, B. R.; Jung, E. D.; Lee, S.; Chu, J. H.; Lee, D.-K.; Choi, K. J.; Cho, S.; Song, M. H., High-Performance Planar Perovskite Optoelectronic Devices: A Morphological and Interfacial Control by Polar Solvent Treatment. *Adv. Mater.* **2015,** *27* (23), 3492-3500.

145. Wang, J.; Wang, D. L.; Moses, D.; Heeger, A. J., Dynamic quenching of 5-(2 '-ethyl-hexyloxy)-p-phenylene vinylene (MEH-PPV) by charge transfer to a C-60 derivative in solution. *J. Appl. Polym. Sci.* **2001,** *82* (10), 2553-2557.

146. You, J.; Hong, Z.; Yang, Y.; Chen, Q.; Cai, M.; Song, T.-B.; Chen, C.-C.; Lu, S.; Liu, Y.; Zhou, H.; Yang, Y., Low-Temperature Solution-Processed Perovskite Solar Cells with High Efficiency and Flexibility. *ACS Nano* **2014,** *8* (2), 1674-1680.

147. Nguyen, W. H.; Bailie, C. D.; Unger, E. L.; McGehee, M. D., Enhancing the Hole-Conductivity of Spiro-OMeTAD without Oxygen or Lithium Salts by Using Spiro(TFSI)(2) in Perovskite and Dye-Sensitized Solar Cells. *J. Am. Chem. Soc.* **2014,** *136* (31), 10996-11001.

148. Seo, J. H.; Yang, R.; Brzezinski, J. Z.; Walker, B.; Bazan, G. C.; Nguyen, T.-Q., Electronic Properties at Gold/Conjugated-Polyelectrolyte Interfaces. *Adv. Mater.* **2009,** *21* (9), 1006-1011.

149. Walker, B.; Tamayo, A.; Yang, J.; Brzezinski, J. Z.; Nguyen, T.-Q., Solution-processed small molecule-based blue light-emitting diodes using conjugated polyelectrolytes as electron injection layers. *Appl. Phys. Lett.* **2008,** *93* (6), 063302.

150. Seo, J. H.; Gutacker, A.; Walker, B.; Cho, S.; Garcia, A.; Yang, R.; Nguyen, T.-Q.; Heeger, A. J.; Bazan, G. C., Improved Injection in n-Type Organic Transistors with Conjugated Polyelectrolytes. *J. Am. Chem. Soc.* **2009,** *131* (51), 18220-18221.

151. Miller, O. D.; Yablonovitch, E.; Kurtz, S. R., Strong Internal and External Luminescence as Solar Cells Approach the Shockley-Queisser Limit. *IEEE J. Photovolt.* **2012,** *2* (3), 303-311.

152. Lim, K.-G.; Ahn, S.; Kim, H.; Choi, M.-R.; Huh, D. H.; Lee, T.-W., Self-Doped Conducting Polymer as a Hole-Extraction Layer in Organic–Inorganic Hybrid Perovskite Solar Cells. *Adv. Mater. Interfaces* **2016,** *3* (9), 1500678.

153. Lim, K.-G.; Kim, H.-B.; Jeong, J.; Kim, H.; Kim, J. Y.; Lee, T.-W., Boosting the Power Conversion Efficiency of Perovskite Solar Cells Using Self-Organized Polymeric Hole Extraction Layers with High Work Function. *Adv. Mater.* **2014,** *26* (37), 6461-6466.

Acknowledgements

2010년 7월 하계연구장학생프로그램(U-SURF)을 통해 처음 UNIST에 오게 되었고 교수님을 알게 되었습니다. 그때 교수님께서 파이를 예시로 들면서 “각자 가지고 있는 파이 조각을 맞추면 더 큰 파이를 완성시킬 수 있는데 서로가 파이조각을 나누어 가지려고만 해서 파이 조각이 더 작아지고 있다.”는 말씀이 저에겐 큰 울림으로 다가왔습니다. 또한 열정적으로 연구하고 있는 실험실 선배들을 보면서 나 또한 이곳에서 같이 연구하면 좋겠다고 다짐했습니다. 운이 좋게도 1년 뒤 전 NGEL의 멤버가 되어있었습니다. 그리고 어느새 또 시간이 흘러 이제 감사의 글을 적고 있습니다. 계속될 것만 같았던 저의 대학원 생활의 마침표가 다가온 다는 것이 아직은 실감이 나지 않습니다. 마지막까지 완주할 수 있도록 이끌어 주신 김진영 교수님께 제일 먼저 감사의 인사를 올립니다. 과연 내가 이 길을 걷고 있는 것이 옳은 길일까? 고민하고 있을 때 “힘들어도 완주하는 것이 제일 중요하다 버텨라.” 라는 말씀을 듣고 포기하지 않고 완주할 수 있었습니다.

7년이라는 시간동안 참 많은 사람들이 저에게 도움을 주었습니다. 무엇보다도 우리 NGEL 멤버들에게 감사의 인사를 전합니다. 이제 교수님이 되어버린 저의 선배이자 동료이자 친구인 효성이, 힘들 때 위로와 함께 항상 조언을 해주는 한국화학연구원의 박사님이 된 서진이형, 아무것도 모를 때 같이 일해 준 NGEL의 터줏대감 기환이 형, 그리고 짧았지만 정말 따뜻하게 대해 주었던 강원대 교수님 성범이형, 무슨 일이던 거절 하는 법 없이 도와 주셨던 Bright Walker 교수님, 호주에서 맘고생하고 있는 반천패밀리 태효, 미국에서 잘 살고 있는 명희, 다시 돌아와서 연구를 시작한 혜림이, NGEL의 선배님들 모두 감사합니다. 그리고 동기로 들어와서 같이 고생한 세영이, 아무것도 모르는 상태에서 페로브스카이트 연구한다고 고군분투한 나의 또 다른 공동연구자 재기, 고작 6개월 늦게 들어왔지만 어린 나이로 인해 계속해서 선배대접 해준 똑똑한 정우, 같이 졸업하는

NGEL의 졸업동기들에게도 감사합니다. 곧 이어 졸업할 예정인 언제나 착한 송이와 독일에서 연구하고 있는 택호, 랩장임에도 불구하고 위로 선배들이 너무 많아서 계속 막내처럼 행동할 수밖에 없었던 영진이, 대학원 학생회장까지 역임한 강택이, 새로운 하드워커가 된 나경이, 곧 NGEL의 실세가 될 재원이, 호주에서 고생하고 있는 NGEL의 살림꾼 형수, 너무 많은 선배들 때문에 매일 실험실 뒷정리하는 윤섭이와 혜원이, 그리고 막내라인 지우와 종득이 모두들 감사합니다. 계속 해서 NGEL을 이끌어 주길 바랍니다. 그 외 UNIST에서 많은 도움 주신 모든 분들에게 감사합니다. 또 힘들 때마다 웃게 해주는 후려 친구들과 구리 친구들 모두 감사합니다.

마지막으로 하늘에 계신 어머니와 항상 저를 믿고 응원해주는 나의 가족들 아버지, 누나, 매형과 장인어른, 장모님, 처형, 처남 모두 감사합니다. 긴 학위 기간동안 묵묵히 기다려주고 그 누구보다도 저에게 가장 큰 힘이 되어준 제가 이 자리에 올 수 있게 해준 저의 사랑하는 아내 경령이에게 너무 고맙고 또 감사하다고 전하고 싶습니다.

저에게 도움을 주시고 응원해 주시는 모든 분들에게 감사의 말을 전하며 이 감사함에 조금이나마 보답할 수 있도록 더욱 노력하겠습니다.

김학범 올림